論文 / 著書情報
Article / Book Information

題目(和文)	炭素繊維強化複合材料の繊維うねりの検出および寸法推定のための渦電流探傷試験法
Title(English)	EDDY CURRENT TECHNIQUE FOR DETECTION AND SIZE ESTIMATION OF FIBER WAVINESS IN CARBON FIBER REINFORCED COMPOSITES
著者(和文)	水上孝一
Author(English)	Mizukami Koichi
出典(和文)	学位:博士（工学）, 学位授与機関:東京工業大学, 報告番号:甲第10313号, 授与年月日:2016年9月20日, 学位の種別:課程博士, 審査員:水谷 義弘,轟 章,井上 裕嗣,因幡 和晃,赤坂 大樹,横関 智弘
Citation(English)	Degree:, Conferring organization: Tokyo Institute of Technology, Report number:甲第10313号, Conferred date:2016/9/20, Degree Type:Course doctor, Examiner:,,,,,
学位種別(和文)	博士論文
Type(English)	Doctoral Thesis

TOKYO INSTITUTE OF TECHNOLOGY

EDDY CURRENT TECHNIQUE FOR DETECTION AND SIZE ESTIMATION OF FIBER WAVINESS IN CARBON FIBER REINFORCED COMPOSITES

by

Koichi Mizukami

A thesis submitted to Tokyo Institute of Technology for the degree of
Doctor of Engineering

Department of Mechanical Sciences and Engineering
Tokyo Institute of Technology
2-12-1 Ookayama, Meguro-ku, Tokyo 152-8552, Japan

June 2016

Abstract

This thesis presents an eddy current method for detection and size estimation of fiber waviness in carbon fiber reinforced plastics (CFRPs).

First, analytical solutions for eddy current distribution in CFRP were derived to investigate the effect of anisotropic electrical properties of CFRP on the eddy current distribution. It was assumed that infinitely long line drive current was placed above a CFRP plate. Maxwell's equations of vector potential were solved taking the orthotropic electrical conductivity into consideration. When the tested CFRP is a unidirectional laminate, the differential equations can be solved if the line drive current is directed in the fiber direction or transverse direction. The derived analytical solutions indicate that the eddy current distribution in the unidirectional CFRP is dependent only on the electrical conductivity in the drive current direction, and is independent of electrical conductivities in other directions. Moreover, the direction of the eddy current corresponds to the direction of the line drive current. The method to solve differential equations could be used to derive analytical solutions to the eddy current distribution in cross-ply laminates. It was found that in the case of cross-ply laminates, the eddy current can be concentrated only in carbon fiber layers which have a direction corresponding to the drive current direction. This finding implies that the inspected fiber direction can be selected by changing the azimuth of the line drive current.

Second, an eddy current probe specialized for waviness detection was newly proposed. The proposed probe is composed of rectangular driver and pickup coils perpendicular to each other. The probe has high sensitivity to the presence of in-plane waviness and can select layers to be inspected of cross-ply laminates. The selectability of inspected layers was validated thorough analytical solutions for the eddy current distribution and finite element method analyses. The probe was used to detect artificially induced in-plane waviness in cross-ply CFRP laminates and a laminate including ±45 deg. layers. It was observed that the output signal of the probe had an extreme value at the vertex of the waviness, which implies the possibility of precise identification of waviness location. Detectability of subsurface waviness was investigated using a 20-layer cross-ply laminate and 24-layer laminate including ±45 deg. layers that had in-plane waviness at different depths. Experimental results showed that the in-plane waviness 18 layers from the surface of the cross-ply laminate could be detected. It was shown in the experiments for the laminate including ±45 deg. layers that signal changes at waviness zones were observed only when the probe azimuth corresponded to the fiber direction with the waviness. This result indicates that fiber

direction with waviness can be identified even in the case of laminates including ±45 deg. layers. The minimum angle of the detected waviness was 6.9 deg. In-plane waviness was simulated in finite element method analyses, and the distribution of the electromagnetic field was calculated. The effectiveness of the probe and the physical background of the obtained signals were verified by investigating the magnetic field around the waviness zone. The detectability of the proposed probe was compared with that of a half-transmission probe which is conventionally used for textural analysis of woven CFRPs. Experimental results showed that no signal change of the half-transmission probe could be observed when the same specimens were tested. This result confirms that the proposed probe has more excellent detectability of waviness.

Third, an eddy current method to visualize fiber waviness in multidirectional CFRPs was proposed. Since eddy currents induced by a driver coil flow along carbon fibers, waviness can be visualized if the eddy current path is visualized. In this method, the eddy current path is identified by the measurement of the magnetic field distribution. A new complex plane analysis method to visualize eddy current path from the magnetic field was proposed. Because the measured magnetic field includes the magnetic field from the drive current and eddy current, the excitation field from the drive current is eliminated by the complex plane analysis. The validity of the method was verified by finite element method analyses. It was shown that the surface waviness could be more accurately estimated at a higher drive frequency, while a lower frequency was better for the subsurface waviness. Experiments of the proposed method were performed for multidirectional CFRP specimens. A rectangular driver coil was placed above a waviness zone and the eddy current path was estimated from the magnetic field measured by scanning the CFRP surface with a pickup coil. Eddy current path was visualized from the deformation of the magnetic field, and the shape of the deformation corresponded to the shape of the induced waviness. The sizes of the wavy eddy current path were compared with waviness sizes measured by X-ray computed tomography and from optical images. Experimental results indicate that the amplitude and angle of the surface waviness can be estimated with errors of approximately -10% and -1 deg., respectively. Subsurface waviness sizes are underestimated, and the error becomes larger as the depth of the waviness increases.

Table of contents

Chapter 1

Introduction

1.1 Carbon fiber reinforced plastics

Carbon fiber reinforced plastics (CFRPs) are composite materials that consist of carbon fibers and resin. Fig. 1.1 shows schematic illustrations of CFRP. By combining carbon fibers and resin, excellent mechanical properties that cannot be provided by each material alone can be obtained. Carbon fibers have high tensile strength and stiffness. However, carbon fiber itself is flexible and cannot be used as a structural material. When carbon fibers are embedded in resin, the composite material can be resistant to compression and bending. By combining carbon fibers and resin, CFRP can be a light material with high strength. Hence, the notable advantages of CFRP are its high specific strength and specific stiffness. Because CFRP is reinforced by carbon fibers, it has anisotropic material properties. Unidirectional CFRP shown in Fig. 1.1(a) has high tensile strength in the fiber direction and lower tensile strength in the transverse direction. To increase strength in multiple directions, unidirectional plies are stacked such that they are directed in different directions as shown in Fig. 1.1(b).

Owing to the excellent mechanical properties of CFRP, the application of CFRP has great potential in reducing the weight of a structure. CFRP has been increasingly used as a structural material in the aerospace and automobile industries. In the aviation industry,

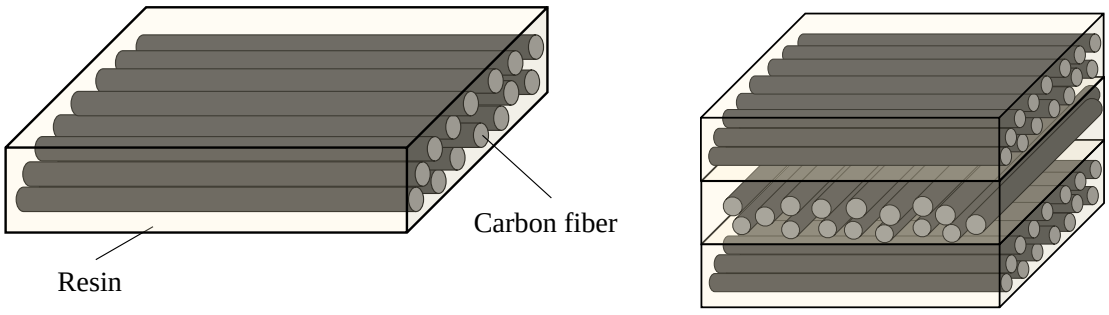

(a) (b)

Fig. 1.1 Schematic illustrations of CFRP: (a) unidirectional CFRP, (b) multidirectional CFRP.

the improvement of fuel efficiency and cruising distance is an important task. In the early stage of application to aircraft, CFRP was used only for secondary structures such as an outer panel of a tail wing. In recent years, CFRP has been used also for primary structures such as main wings and the fuselage. Currently, more than 50% of the weight of a Boeing 787 is accounted for by CFRP. The high specific strength and specific stiffness of CFRP are useful also for space application. In addition to these mechanical properties, CFRP can have a low coefficient of thermal expansion (CTE). A low CTE is important in guaranteeing dimensional stability under the large temperature variations that space equipment experience. Similar to the case of aerospace components, CFRP has been increasingly adopted for automotive frames and outer panels to reduce weight and environmental load. Initially, CFRP was used only for prestige cars such as the Mercedes-Benz SLR McLaren and Toyota Lexus LFA. Recently, the application of CFRP to passenger vehicles such as the BMWi3 has increased. Compared with the case for the aerospace industry, there is greater potential for growth in CFRP applications in the automobile industries. To realize more applications of CFRP, there is a need to develop fast and low-cost manufacturing methods.

There are several molding methods of molding CFRPs. Fig. 1.2 shows representative methods of molding continuous CFRP. Autoclave molding (Fig. 1.2(a)) is one representative method of molding CFRP in the aerospace industry. Carbon fibers that are pre-impregnated with resin are used as the base material. This form of material is called the prepreg. Generally, the prepreg is a sheet of carbon fibers impregnated with an uncured thermoset resin, such as epoxy or polyester. In recent years, thermoplastic prepregs in which carbon fibers are impregnated with thermoplastic resin have also become commercially available. In autoclave molding, prepregs are laminated on a

metal mold and wrapped in a vacuum bag. Laminated prepregs are then subject to pressure exerted by inert gas and heated in an autoclave. In the case of thermoset prepregs, thermoset resin is cured at a controlled temperature in the autoclave. Thermoplastic prepregs are consolidated at a temperature close to their melting points. Autoclave molding is a reliable molding method for producing high-quality CFRP parts with good reproducibility. Because autoclave molding can eliminate air bubbles, CFRP with excellent mechanical properties can be obtained. Resin transfer molding (RTM) (Fig. 1.2(b)) is a method of injecting resin to the preform of carbon fibers. Carbon fibers are placed between male and female dies, and liquid resin is pumped into the mold with curing agent. The resin is cured at room temperature and atmospheric pressure. The

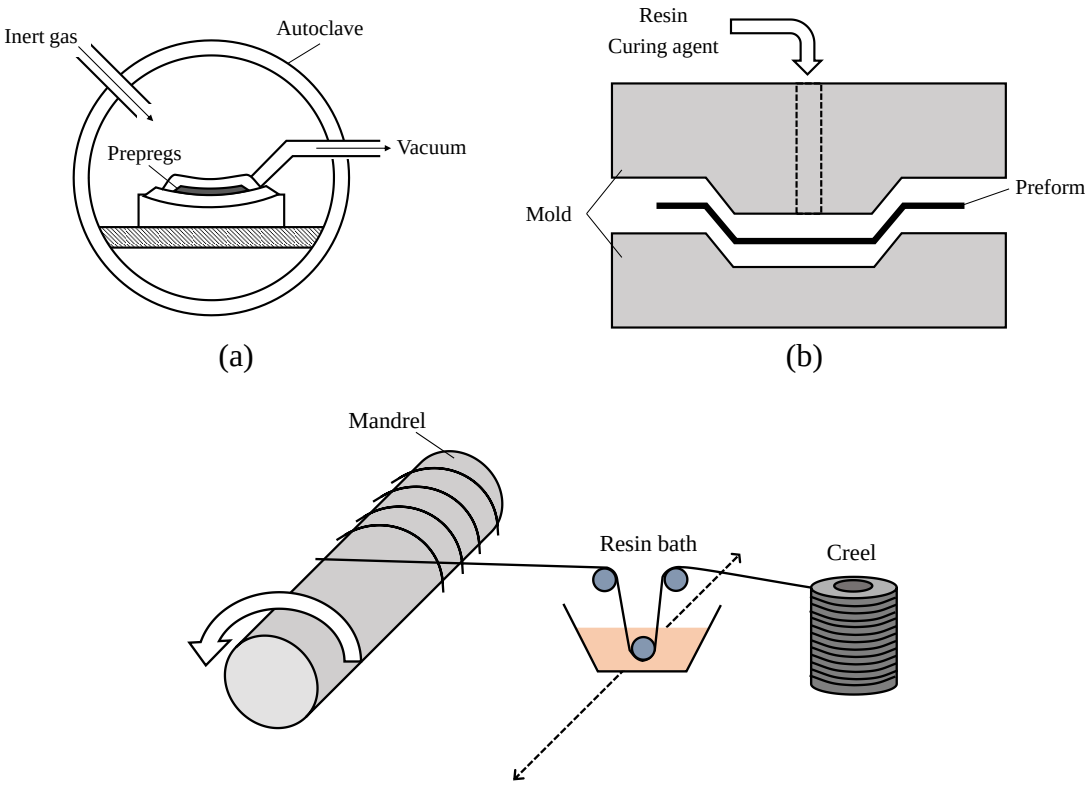

Fig. 1.2 Methods of molding CFRP: (a) autoclave molding, (b) resin transfer molding (RTM), (c) filament winding (FW).

method in which resin is injected by vacuum suction pressure is called vacuum-assisted RTM (VaRTM). RTM is a reliable and reproducible molding method. In addition, RTM is suitable for molding large CFRP parts with dimensional stability. Filament winding (FW) (Fig. 1.2(c)) is a method of molding cylindrical products, such as pressure vessels. In the FW process, a carbon fiber roving impregnated with resin is continuously wound on a mandrel with tension. After forming a cylindrical shape with the carbon fiber roving, resin is cured in a furnace. Because FW can produce CFRP with high volume fraction of carbon fibers, a product with high strength can be obtained.

1.2 Formation of fiber waviness

In the manufacturing process, defects can form in CFRP parts. Fiber waviness is one of the manufacturing defects of CFRP that affect structural integrity. Fiber waviness is a deformation of carbon fibers that are supposed to be straight in CFRP. Fig. 1.3 shows an example image of fiber waviness.

Formation mechanisms of waviness are divided into two groups: mechanisms of process-induced waviness and those of material-design-induced waviness.

The mechanisms of process-induced waviness relate to waviness produced by thermal residual stresses originating from process parameters [1.1]–[1.2]. Kuglar and Moon investigated process parameters that affect waviness development [1.3]. They counted the number of waviness and measured sizes of the waviness in T300 carbon fiber/Polysulfone unidirectional laminates processed in an autoclave. They investigated the effects of eight parameters: the hold temperature, hold time, pressure, part length, width, thickness, cooling rate and tool plate material. They found that only three parameters affect waviness development: the part length, cooling rate and tool plate material. Kuglar and Moon showed that the CTE of the tool plate is the most important among these process parameters. This is because mismatch in the CTE between the

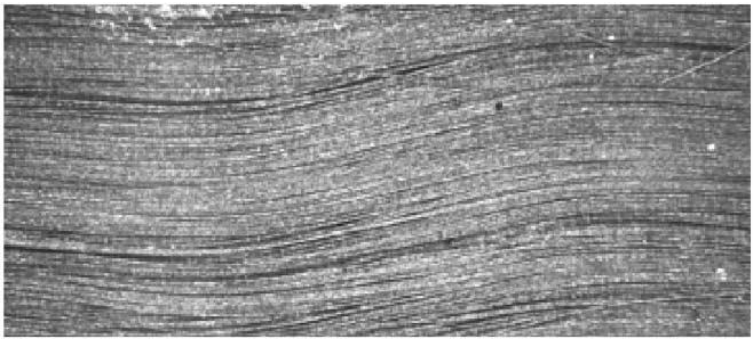

Fig. 1.3 Photograph of in-plane waviness induced in a thin laminated composite plate [1.3].

composite material and tool plate imposes a compressive load on the composite material. Generally, the CTE of a metal tool plate is much higher than that of a carbon fiber composite, resulting in compressive stress on the composite during cooling. Because an aluminum plate has a relatively high CTE, it has been reported that the use of an aluminum tool plate results in larger number of waviness compared with the use of copper and steel plates. A higher cooling rate also leads to compressive stress on the laminate surface because a higher cooling rate does not allow time for stress to be relaxed and produces a through-thickness temperature gradient. Waviness development in the FW process was also investigated by Kuglar and Moon [1.4], who found that mandrel material with a higher CTE produces a larger CTE mismatch-based driving force of out-of-plane waviness development. In addition, they showed that sufficient tow tension is required in the winding process to minimize waviness development. Kiuchi et al. developed a model of fiber waviness development in thermoset CFRP assuming perfect bonding between the composite material and tool plates [1.5]. According to their model, waviness formation is affected not only by CTE mismatch but also by an initial deflection of carbon fibers in the prepreg. Because it is difficult to exclude the initial fiber deflection in the prepreg, their modeling implies that waviness development is almost inevitable.

The mechanisms of material-design-induced waviness relate to waviness produced by the component shape or laminate stacking sequence that cannot be eliminated by improving process parameters. Potter et al. presented several layup examples that are inevitably accompanied by waviness [1.6]. When fiber tows are draped on a curved shape, such as a hemispheric structure, there is an inevitable path difference between tow edges as shown in Fig. 1.4. This must result in fiber waviness for the excess length

to collapse. Moreover, when an L-shaped part is fabricated on the corner of the L-shaped tool, significant waviness forms at the corner. This is because when the autoclave pressure is applied to the L-shaped part during molding, the material is forced into the tool carrying excess material into the radius as shown in Fig. 1.5. As described above, an excess length of fiber reinforcement can be a source of waviness development. Lightfoot et al. investigated mechanisms of the development of in-plane fiber misalignments produced in U-shaped graphite/epoxy parts shown in Fig. 1.6 [1.7]. They showed that large in-plane fiber misalignments are produced near the corner of the

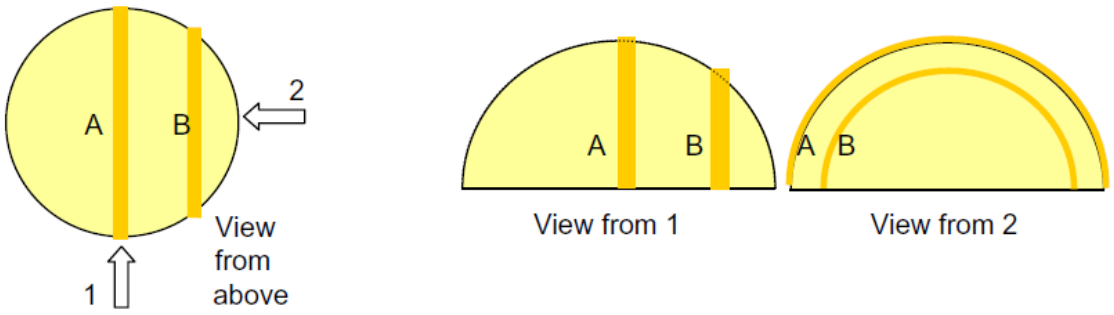

Fig. 1.4 Path differences between the edges of tows on the surface of a hemisphere [1.6].

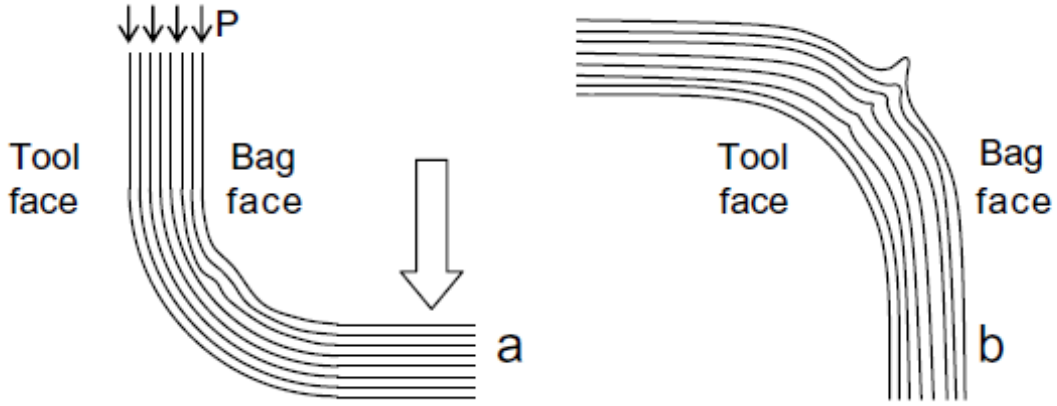

Fig. 1.5 Typical out-of-plane fiber waviness in corner regions of autoclave-molded thermoset prepreg parts [1.6].

U-shaped composite. This is explained by bridging that occurs in the production of curved composites. For example, when a 90° layer and 0° layer are stacked on the inside corner of the mold, the 0° layer cannot be formed into the corner of the tool material because of its high stiffness, which results in bridging of the laminate. When pressure is applied in the autoclave molding process, a shear force is applied to the 90° layer, resulting in the formation of huge out-of-plane waviness. Moreover, it was shown that huge in-plane waviness with a misalignment angle up to 50° is also induced because of the accommodation of excess length at the corner. Lightfoot et al. also identified combinations of fiber orientation that easily produce in-plane waviness [1.8].

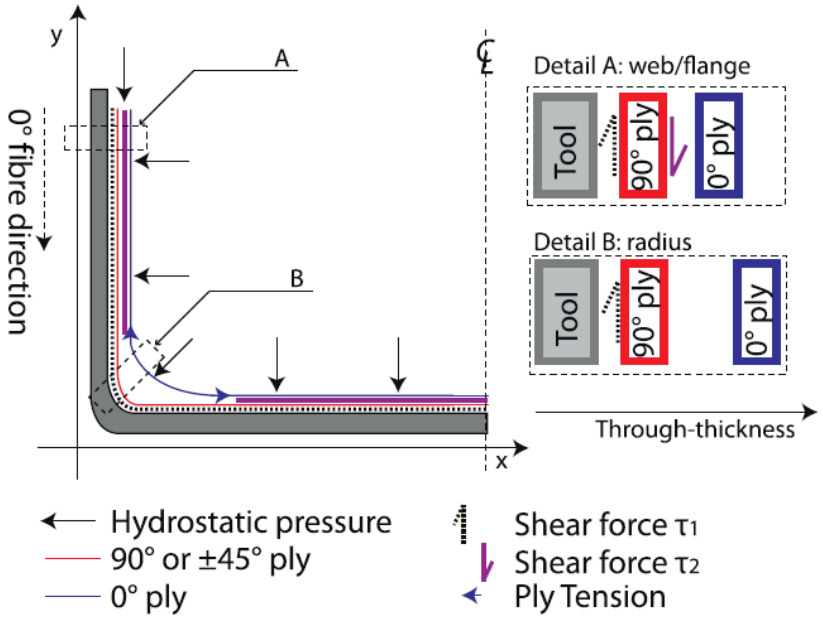

Fig. 1.6 Free-body diagram of half of a simple composite U-section cured on a metallic tool (with symmetry about the *x* axis) [1.7].

1.3 Effects of waviness on mechanical properties

It is well known that shear failure and fiber microbuckling are representative compression failure mechanisms [1.9]–[1.13]. Fiber waviness greatly reduces the compressive strength of CFRP. Unidirectional CFRP has the highest compressive strength when the compressive load is applied in the 0° fiber direction. However, the compressive strength is reduced when fibers are misaligned from the compressive load axis. Lo and Chim [1.14] and Yokozeki et al. [1.15] performed off-axis compression tests and measured the compressive strength of unidirectional CFRPs. According to their results, an in-plane misalignment of 15° can lead to more than 50% loss of compressive strength, as shown in Fig. 1.7. In addition, Yokozeki et al. showed that stiffness is greatly reduced by in-plane fiber misalignment. Thus, fiber misalignment caused by waviness leads to significant reduction in compressive strength. Mrse and Piggott measured the compressive strength of composites with artificially induced

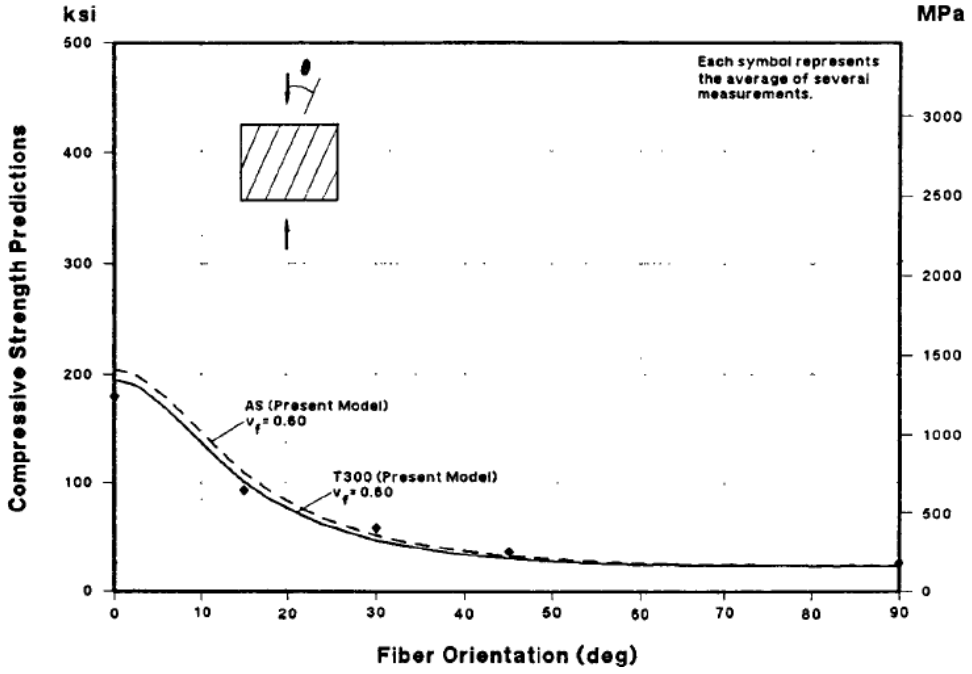

Fig. 1.7 Effect of fiber orientation on the compressive strength of carbon fiber composite [1.14].

in-plane fiber waviness [1.16]–[1.17]. They tested unidirectional samples with a fiber misalignment angle deviation ranging from 1° to 6° and obtained a corresponding compressive strength from 1.9 to 1.5 GPa. In the experiments of Adams and Bell, the most severe waviness in a multi-directional laminate reduced the compressive strength by as much as 35% [1.18]. Moreover, the percentage reduction in compressive strength in the 0° direction was equal to the percentage of 0° layers containing waviness. Chan and Wang [1.19] numerically calculated the stiffness reduction of multidirectional laminates caused by waviness. Chan and Wang calculated the stiffness in the 0° fiber direction of $[0/\pm45/90]_s$ CFRP laminates while varying the ratio of the in-plane waviness amplitude and half wavelength. They found that the stiffness in the 0° fiber direction is strongly affected by the amplitude-to-half wavelength ratio of waviness in the 0° layer, while the size of waviness in other layers has a small effect on the 0° directional stiffness loss. Altmann et al. [1.20] calculated the compressive strength of a unidirectional laminate while varying the amplitude-to-wavelength ratio of out-of-plane waviness. Their calculation confirmed that even a slight change in the amplitude-to-wavelength ratio affects compressive strength. Jumahat et al. [1.12] investigated fracture mechanisms of unidirectional CFRP subject to a compressive load. They established a combined model of fiber micro-buckling and plastic kinking to predict the compressive strength. In this model, the shape of initial fiber waviness is assumed to be a sine function. They showed that when the initial misalignment angle of waviness is changed from 1 to 5°, the compressive strength changes from 1191 to 461 MPa. They also found that when waviness has the same misalignment angle, waviness with a longer wavelength provides a greater reduction in compressive strength. According to researches described above, fiber waviness causes significant reduction in

the compressive strength and stiffness of CFRPs. Waviness affects compressive properties in the fiber direction with the waviness. Moreover, size of waviness strongly affects the loss of compressive strength and stiffness.

The effect on tensile behavior has been investigated in several studies. Chun et al. numerically obtained the tensile strength of a unidirectional graphite/epoxy plate with localized out-of-plane waviness [1.21]. When the amplitude-to-wavelength ratio of the waviness was varied from 0.011 to 0.034, the calculated tensile strength reduced by approximately 5%. El-Hajjar and Petersen performed tensile tests on multidirectional carbon/epoxy laminates with large out-of-plane waviness [1.22]. They used out-of-plane waviness with heights ranging from 0.9 to 1.55 mm, which was accompanied by thickness reduction. They showed that delamination growth occurs in the vicinity of the waviness and that reduction in tensile strength increases as waviness height increases. Khattab et al. developed a method of manufacturing CFRP with out-of-plane waviness that does not reduce the thickness [1.23]. They performed tensile tests for unidirectional CFRP specimens fabricated by their method and found that failure starts with delamination around the waviness area.

Waviness also degrades fatigue behavior. Adams and Hyer carried out compression fatigue tests on CFRP specimens with out-of-plane waviness [1.24]. Waviness with an amplitude-to-wavelength ratio from 0.05 to 0.06 exhibited loss of fatigue life, and the stress level corresponding to a 10^6 cycle run-out for the specimen was reduced to approximately 45 % of the static compression strength of the defect-free laminate.

1.4 Conventional nondestructive testing techniques for waviness

Because fiber waviness causes significant reduction in compressive strength and stiffness of CFRPs, a method to detect waviness is of particular importance. In earlier studies, the detection and measurement of waviness relied on optical measurements of the sample cross-section [1.25]–[1.27]. In recent years, several nondestructive testing (NDT) methods for waviness have been studied. Fiber waviness is divided into two types: in-plane waviness and out-of-plane waviness. Depending on the type of waviness, different types of NDT technique have been studied because of difference in physical background each NDT method uses.

One promising nondestructive technique for waviness is X-ray computed tomography (CT). Because X-ray CT can have excellent detectability of fiber orientation with high spatial resolution, attempts have been made to use X-ray CT in industry. Sutcliffe et al. developed a micro-CT X-ray imaging methodology for measurement of fiber orientation in CFRP, and successfully detected in-plane and out-of-plane fiber misalignments with standard deviations of 1.21° and 0.75° respectively [1.28]. However, it remains difficult to clearly distinguish the fiber and matrix in X-ray CT images because carbon fiber and resin have similar radiodensities [1.29]. Hence, image processing still plays an important role in X-ray CT imaging. Furthermore, X-ray CT can be limited by the geometry of tested components, and the inspection of large structures is, therefore, often difficult.

Ultrasonic testing is an NDT technique that is used in practice for damage detection of composite materials in the aerospace field. There have been attempts to conduct ultrasonic testing for detecting fiber waviness in CFRPs. Yang et al. developed a pitch-catch ultrasonic technique to assess the fiber orientation of CFRPs [1.30]. Smith et

al. succeeded in mapping the huge in-plane fiber misalignment by choosing a small group of waveforms and short time window [1.31]. In addition, Smith successfully quantified the out-of-plane ply angle using a focused probe. Zardan et al. studied deviations of an ultrasonic beam induced by an oblique interface of out-of-plane waviness, and experimentally detected the perturbed acoustic field [1.32]. Pain and Drinkwater applied the total focusing method (TFM) to an ultrasonic array technique [1.33]. They found experimentally that out-of-plane waviness could be visualized clearly in a TFM phase image. Although these methods can be used for detection of waviness, tested materials must be immersed in water so that ultrasonic waves propagate through the material under test. This makes it difficult to inspect a large structure. In addition, some components are not allowed to absorb water in the aerospace field.

Thermal nondestructive techniques have been developed in recent years to detect waviness. Elhajjar et al. investigated the application of thermoelastic stress analysis to the detection of out-of-plane waviness in carbon fiber composites [1.34]. They measured the surface temperature of a specimen with out-of-plane waviness under cyclic loading, and showed that the location of waviness was visible in the obtained thermal image. Although this approach can be used to identify the location of fiber waviness, it is difficult to inspect the inside of the tested material. Moreover, this approach is limited by component geometries because of the use of cyclic loading.

The above mentioned NDT techniques for waviness have restrictions even though the detectability of waviness has been experimentally verified. More importantly, an NDT technique for small in-plane waviness has not yet been established although out-of-plane waviness can be detected and visualized by ultrasonic testing using the

difference in the time of flight caused by an oblique ply interface. Only X-ray CT has the potential to detect small in-plane waviness. However, it is difficult for X-ray CT to inspect large structures used in practice in the aerospace industry. During the manufacturing process, the out-of-plane motion of fibers is restricted in the case of a thin laminate. Because CFRP is often used as thin plates, NDT for in-plane waviness is more important. Since it is difficult to detect in-plane waviness, manufacturers of CFRP parts often rely on strength tests. However, huge cost is required for a strength test. Therefore, there is great demand for an NDT technique for in-plane waviness that is free from the difficulty encountered by the conventional technique.

1.5 Eddy current testing for CFRPs

Eddy current testing (ET) is a nondestructive method used for electrically conductive materials. ET has been conventionally used to detect cracks in metal structures [1.35]–[1.38]. Fig. 1.8 shows the physical principle of ET. Eddy currents are induced in the material under test by a driver coil according to the law of electromagnetic induction. The magnetic field generated by the eddy currents is measured by a pickup coil. A change in the eddy current path caused by a local defect can be detected by a change in the pickup coil voltage and the defect location can be identified. The pickup coil can be replaced by any magnetic sensor, such as the giant magnetoresistive sensor and superconducting quantum interference device magnetometer [1.39]–[1.43]. Generally, the amplitude of eddy current exponentially attenuates in the thickness direction of the material [1.44]. This is referred to as the skin effect, and the penetration depth of the eddy current has been defined as the depth at which the amplitude of the eddy current becomes 1/*e* of the surface eddy current. Because of the skin effect, ET has been used mainly for detection of defects on a material surface. ET has the advantages that materials can be tested without contact and that it allows fast single-sided scanning. ET thus has the potential to overcome the difficulty encountered in X-ray CT imaging.

ET can be used for carbon fiber composites because carbon fibers are electrically

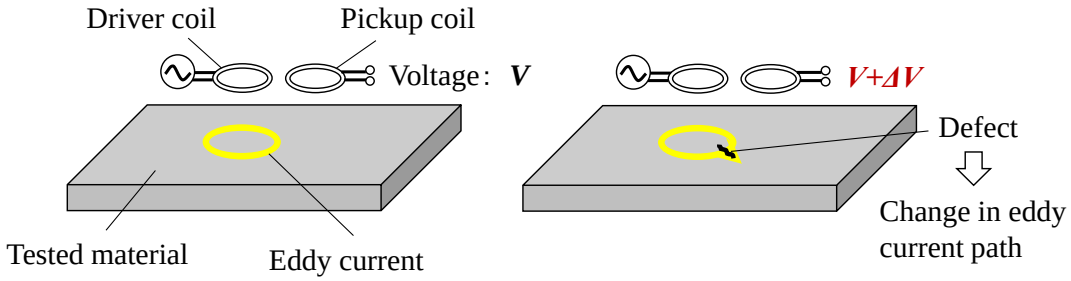

Fig. 1.8 Basic principle of defect detection in eddy current testing.

conductive. Since the unidirectional ply of a carbon fiber layer has strong anisotropy in electrical conductivity [1.44]–[1.45], eddy current distributions in CFRP become more complicated than those in metal. Some studies successfully applied ET to the detection of damage in CFRP, such as fiber breakages and delamination [1.46]–[1.50].

The in-plane carbon fiber orientation can be identified by using the strong anisotropy of conductivity. The rotation of a pair of driver and pickup coils, which are sometimes called a half-transmission probe, is often used to characterize in-plane fiber orientations. Lange and Mook [1.51], Mook et al. [1.52] and Yin et al. [1.53]–[1.54] measured the output voltage of the pickup coil during the rotation of a pair of driver and pickup coils on CFRP plates. Fig. 1.9 shows the rotating eddy current probe and examples of the obtained polar diagrams. They found that the output signal has a local maximum in the polar diagram when the probe azimuth corresponds to fiber directions. Moreover, Mook et al. showed that the angular resolution of this method can be improved by increasing the distance between driver and pickup coils and by using coils with smaller diameters [1.52]. Cheng et al. verified the improvement of angular resolution by carrying out

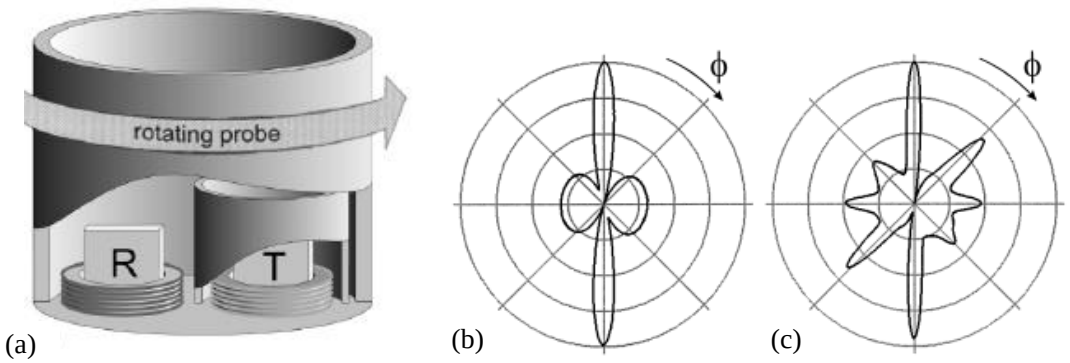

(a) (b) (c)

Fig. 1.9 Eddy current method used to identify the fiber orientation of CFRP [1.52]: (a) rotating eddy current probe, where T and R denote the transmitter (driver coil) and receiver (pickup coil), (b) polar diagram obtained for a unidirectional CFRP, (c) polar diagram obtained for a multidirectional CFRP ($[90_2/+45_2/0_2/-45_2]$).

finite element analyses of the eddy current distribution [1.55]. They attributed the resolution improvement to the stretch of the eddy current distribution caused by strong anisotropy of the unidirectional ply of the CFRP. Because the method using probe rotation requires a larger distance between the driver coil and pickup coil for higher angular resolution, it is difficult to make the spatial resolution and angular resolution compatible. Thus, probe rotation is not a suitable technique for detecting small in-plane waviness. Heuer et al. [1.56]–[1.59] and Schmidt et al. [1.60] scanned with a half-transmission probe at high frequency up to 100 MHz to enhance the sensitivity and spatial resolution of the probe. Their works showed the excellent spatial resolution of the half-transmission probe and that the fiber orientation is visible in the obtained eddy current image. Heuer et al. investigated the effectiveness of high-frequency eddy current imaging for textural analysis of a CFRP fabric and successfully visualized in-plane waviness. Because carbon fiber fabric has a periodic structure of the fiber roving, the obtained distribution of the probe signal has a stripe pattern as shown in Fig. 1.10. Bardl et al. applied the two-dimensional Fourier transform to a high-frequency eddy current image and successfully mapped local yarn orientations of a draped one-layer biaxial carbon fiber fabric [1.61]. However, the use of a higher drive frequency leads to a smaller penetration depth of eddy currents because of the skin effect, and the inspection of a deeper region of the tested material becomes more difficult. An eddy current technique that can be used at a lower drive frequency is required to detect waviness in a deeper region. Moreover, textural analysis based on the two-dimensional Fourier transform can be applied only to woven CFRP because it uses periodic pattern of the carbon fiber roving. There thus remains a demand for an eddy current method to detect in-plane waviness in CFRP composed of non-woven unidirectional plies.

Detection of out-of-plane waviness is easier than detection of in-plane waviness for ET. Out-of-plane waviness is accompanied by a variation of the fiber volume fraction in the thickness direction of the CFRP. ET can be sensitive to a local change in electrical conductivity caused by variation in the fiber volume content. The detection of out-of-plane waviness in thin laminate was reported by Heuer et al. (Fig. 1.10) [1.59]. Mizukami et al. showed that out-of-plane waviness in a thick unidirectional laminate can be detected using an orthogonal eddy current probe [1.62]. They successfully detected out-of-plane waviness with the maximum amplitude of 3.5 mm approximately 25 mm away from the surface. There is thus demand for an eddy current technique for detection of in-plane waviness.

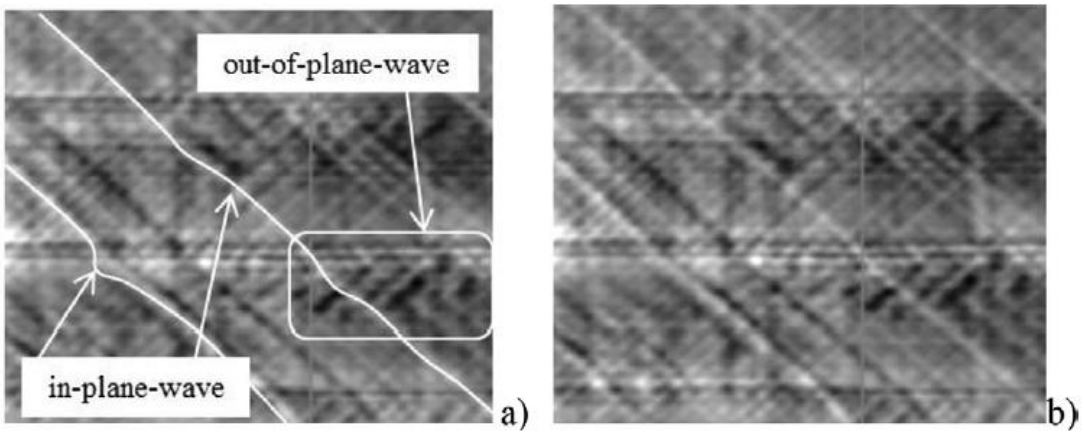

Fig. 1.10 High-frequency eddy current images of CFRP plates with in-plane and out-of-plane waves. (Size 150 mm ×150 mm × 5 mm): a) indication of the wave position, b) raw data image [1.59].

1.6 Objectives of the present study

The objective of the present study is to develop an eddy current-based NDT method for in-plane waviness. The requirements for ET of in-plane waviness are as follows.

1) Investigation of the effect of the anisotropy of CFRP on eddy current distribution

The effectiveness of ET for CFRPs has been experimentally verified by several studies. However, the effect of anisotropic electrical conductivity on eddy current distribution has not been analytically investigated. A derivation of analytical solutions for eddy current in CFRP is needed to clarify the effect of anisotropy and to develop an ET method specialized for waviness detection.

2) Eddy current sensor sensitive to in-plane waviness at low frequency

Because fiber waviness is a small deformation of fibers, it is difficult for conventional ET to detect in-plane waviness. Although the sensitivity and spatial resolution of the eddy current sensor improve at higher frequency, the penetration depth of the eddy current decreases. The detectability of in-plane waviness should be enhanced by the sensor configuration and not by increasing the frequency to achieve a greater penetration depth. An eddy current sensor configuration specific to in-plane waviness detection is required to inspect a thicker laminate.

3) Identification of the fiber direction with in-plane waviness

In-plane waviness causes degradation of the compressive strength and stiffness in the fiber direction with the waviness. Hence, the identification of the fiber direction with waviness is important in the inspection of multidirectional CFRPs. Layups of 0° and 90°

layers, and layups of 0°, 90°, +45° and −45° layers are often used for CFRP laminates. It is necessary to develop an ET method that can inspect these multidirectional laminates.

4) Visualization of in-plane waviness for size estimation

Reduction of the compressive strength and stiffness resulting from waviness depends on the size of the waviness. Visualization of waviness for size estimation is important in evaluating degradation of mechanical properties. Conventionally, estimation of the defect size in ET has relied on inverse analyses. In the case of metals, the perturbation of the electromagnetic field caused by a crack can be analytically derived using the dyadic Green function [1.63]–[1.67]. Finite element method (FEM) analyses are also conducted to solve the forward problem by modeling a crack [1.68]. However, in the case of CFRP, it is difficult to analytically obtain the perturbation of the electromagnetic field caused by in-plane waviness. Moreover, it is more difficult to have agreement between experimental data and numerical calculation result for CFRPs than it is for metals. This is because of variations in electrical conductivity in CFRP as a result of material inhomogeneity. It is thus difficult to estimate the size of in-plane waviness by comparing experimental data and calculations. There is a need for a development of an eddy current technique that can visualize in-plane waviness without inverse analysis.

1.7 Thesis outline

This thesis presents an eddy current method for the detection and size estimation of in-plane waviness in CFRP. Fig. 1.11 is a flow chart for the thesis.

Chapter 1 Introduction

The background of this study is presented. Formation mechanisms of waviness and the effects of waviness on mechanical properties of CFRP are reviewed. Studies on conventional NDT methods for waviness and the restrictions of these methods are described. It is shown that ET has the potential to overcome the difficulty encountered by conventional methods. The purpose of the present study is the development of an ET method to detect and visualize waviness.

Chapter 2 Derivation of analytical solutions to the eddy current problem of CFRP

The eddy current distribution in CFRP induced by a line current is derived. The effect of anisotropic conductivity on the eddy current distribution is investigated. The physical background of the derived analytical solution is discussed.

Chapter 3 Layer-selectable eddy current technique for detection of in-plane waviness

An eddy current method sensitive to in-plane waviness is newly proposed. Using the analytical solutions for the eddy current distribution, a method to select the inspected fiber layer is developed. The validity of the proposed method is investigated in FEM analyses. Experiments are performed for multidirectional CFRP specimens with artificially induced in-plane waviness.

Chapter 4 Eddy current imaging technique for visualization of in-plane fiber waviness

A method to visualize the eddy current path is newly proposed to visualize in-plane waviness. The accuracy of estimation of the waviness shape and size is investigated in FEM analyses. Magnetic field measurements to visualize eddy current path are performed for CFRP specimens with waviness. The shape and size of the visualized eddy current path are compared with those measured from X-ray CT and optical images.

Chapter 5 Conclusions and future works

Findings obtained in this thesis are summarized. An inspection scenario for in-plane waviness in CFRP is proposed according to the results obtained in the present study. Future works required for further improvement of waviness inspection are mentioned.

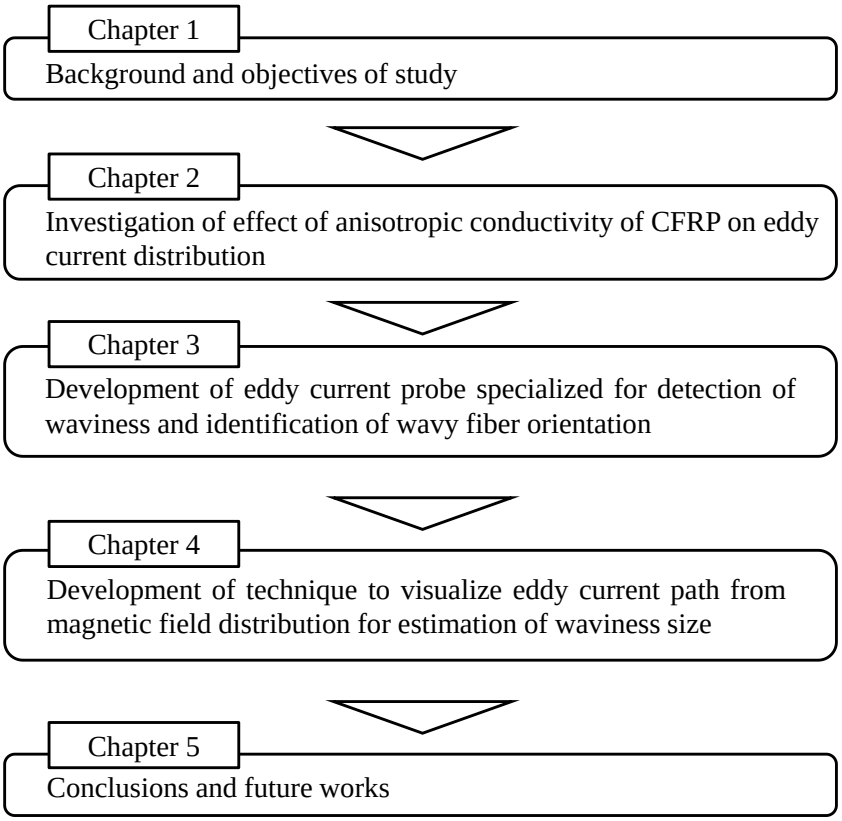

Fig. 1.11 Flow chart of the thesis

1.8 References

[1.1] Patricia P. Parlevliet, Harald E. N. Bersee, Adriaan Beukers, “Residual stresses in thermoplastic composites − A study of the literature − Part I Formation of residual stresses”, Composites: Part A, Vol. 37, (2006), pp. 1847-1857.

[1.2] Patricia P. Parlevliet, Harald E. N. Bersee, Adriaan Beukers, “Residual stresses in thermoplastic composites – a study of the literature. Part III Effects of thermal residual stresses”, Composites: Part A, Vol. 38, (2007), pp. 1581-1596.

[1.3] Danielle Kugler and Tess J. Moon, “Identification of the Most Significant Processing Parameters on the Development of Fiber Waviness in Thin Laminates”, Journal of Composite Materials, Vol. 36, No. 12, (2002), pp. 1451-1479.

[1.4] Danielle Kugler and Tess J. Moon, “The effect of Mandrel material and tow tension on defects and compressive strength of hoop-wound, on-line consolidated, composite rings”, Composites: Part A, Vol. 33, (2002), pp. 861-876.

[1.5] Takehiro Kiuchi, Akira Todoroki, Ryosuke Matsuzaki and Yoshihiro Mizutani, “Fiber-waviness Model in Filament Winding Process”, Journal of Solid Mechanics and Materials Engineering, Vol. 4, No. 1, (2010), pp. 63-74.

[1.6] K. Potter, B. Khan, M. Wisnom, T. Bell, J. Stevens, “Variability, fibre waviness and misalignment in the determination of the properties of composite materials and structures”, Composites: Part A, Vol. 39, (2008), pp. 1343-1354.

[1.7] James S. Lightfoot, Michael R. Wisnom, Kevin Potter, “A new mechanism for the formation of ply wrinkles due to shear between plies”, Composites: Part A, Vol. 49, (2013), pp. 139-147.

[1.8] James S. Lightfoot, Michael R. Wisnom, Kevin Potter, “Defects in woven preforms Formation mechanisms and the effects of laminate design and layup protocol”, Composites: Part A, Vol. 51, (2013), pp. 99-107.

[1.9] R. J. Lee, “Compression strength of aligned carbon fibre-reinforced thermoplastic laminates”, Composites, Vol. 18, No. 1, (1987), pp. 35-39.

[1.10] P. M. Jelf and N. A. Fleck, “Compression Failure Mechanisms in Unidirectional Composites”, Journal of Composite Materials, Vol. 26, No. 18, (1992), pp. 2706-2726.

[1.11] P. Berbinau, C. Soutis, I. A. Guz, “Compressive failure of 0° unidirectional carbon-fibre-reinforced plastic (CFRP) laminates by fibre microbuckling”, Composite Science and Technology, Vol. 59, (1999), pp. 1451-1455.

[1.12] A. Jumahat, C. Soutis, F.R. Jones, A. Hodzic, “Fracture mechanisms and failure analysis of carbon fibre toughened epoxy composites subjected to compressive loading”, Composite Structures, Vol. 92, (2010), pp. 295-305.

[1.13] B. Vieille, W. Albouy, L. Chevalier, L. Taleb, “About the influence of stamping on thermoplastic-based composites for aeronautical applications”, Composites: Part B, Vol. 45, (2013), pp. 821-834.

[1.14] K. H. Lo and E. S.-M. Chim, “Compressive strength of unidirectional composites”, Journal of reinforced Plastics and Composites, Vol. 11, (1992), pp. 838-896.

[1.15] Tomohiro Yokozeki, Toshio Ogasawara, Takashi Ishikawa, “Nonlinear behavior and compressive strength of unidirectional and multidirectional carbon fiber composite laminates”, Composites: Part A, Vol. 37, (2006), pp. 2069-2079.

[1.16] A. M. Mrse and M. R. Piggott, “Compressive properties of unidirectional carbon fibre laminates The effects of unintentional and intentional fibre misalignment”, Composites Science and Technology, Vol. 49, (1993), pp. 219-227.

[1.17] M.R. Piggott, “The effect of fibre waviness on the mechanical properties of unidirectional fibre composites: A review”, Composites Science and Technology, Vol. 53, (1995), pp. 201-205.

[1.18] Daniel O’Hare Adams and Steven J. Bell, “Compression strength reductions in composite laminates due to multiple-layer waviness”, Composites Science and Technology, Vol. 53, (1995), pp. 207-212.

[1.19] W. S. Chang and J. S. Wang, “Influence of fiber waviness on the structural response of composite laminates”, Journal of Thermoplastic Composite Materials, Vol. 7, (1994), pp. 243-260.

[1.20] Andreas Altmann, Philipp Gesell, Klaus Drechsler, “Strength prediction of ply waviness in composite materials considering matrix dominated effects”, Composite Structures, Vol. 127, (2015), pp. 51-59.

[1.21] Heoung-Jae Chun, Jai-Yoon Shin, Isaac M. Daniel, “Effects of material and geometric nonlinearities on the tensile and compressive behavior of composite materials with fiber waviness”, Composites Science and Technology, Vol. 61, (2001), pp. 125-134.

[1.22] Rani F. El-Hajjar, Derek R. Petersen, “Gaussian function characterization of unnotched tension behavior in a carbon/epoxy composite containing localized fiber waviness”, Composite Structures, Vol. 93, (2011), pp. 2400-2408.

[1.23] I. Al-din Khattab, J. Kreikemeier and N. S. Abdelhadi, “Manufacturing of CFRP specimens with controlled out-of-plane waviness”, CEAS Aeronautical Journal, Vol. 5, (2014), pp. 85-93.

[1.24] Daniel O’ Hare Adams and M. W. Hyer, “Effects of layer waviness on the compression fatigue performance of thermoplastic composite laminates”, Fatigue,

Vol. 16, (1994), pp. 385-391.

[1.25] Peter J. Joyce, Danielle Kuglar and Tess J. Moon, “A Technique for Characterizing Process-Induced Fiber Waviness in Unidirectional Composite Laminates-Using Optical Microscopy”, Journal of Composite Materials, Vol. 31, No. 17, (1997), pp. 1694-1727

[1.26] C. J. Creighton, M. P. F. Sutcliffe, T. W. Clyne, “A multiple field image analysis procedure for characterisation of fibre alignment in composites”, Composites: Part A, Vol. 32, (2001), pp. 221-229.

[1.27] K. K. Kratmann, M. P. F. Sutcliffe, L. T. Lilleheden, R. Pyrz, O.T. Thomsen, “A novel image analysis procedure for measuring fibre misalignment in unidirectional fibre composites”, Composites Science and Technology, Vol. 69, (2009), pp. 228-238.

[1.28] M. P. F. Sutcliffe, S. L. Lemanski, A. E. Scott, “Measurement of fibre waviness in industrial composite components”, Composites Science and Technology, Vol. 72, (2012), pp. 2016-2023.

[1.29] Akinori Yoshimura, Ryohei Hosoya, Jun Koyanagi and Toshio Ogasawara, “X-ray computed tomography used to measure fiber orientation in CFRP laminates”, Advanced Composite Materials, (2014).

[1.30] In-Young Yang, Kwang-Hee Im, David K. Hsu, Vinay Dayal, Dan Barnard, Ji-Hoon Kim, Cheon-Seok Cha, Young-Tae Cho, Do-Jung Kim, “Feasibility on fiber orientation detection of unidirectional CFRP composite laminates using one-sided pitch–catch ultrasonic technique”, Composites Science and Technology, Vol. 69, (2009), pp. 2042-2047.

[1.31] Robert A. Smith, Supratik Mukhopadhyay, Andrew Lawrie and Stephen R. Hallett, “Applications of ultrasonic NDT to aerospace composites”, Proceedings of 5th International Symposium on NDT in Aerospace, (2013).

[1.32] J. P. Zardan, C. Gueudre, G. Corneloup, “Study of induced ultrasonic deviation for the detection and identification of ply waviness in carbon fibre reinforced polymer”, NDT & E International, Vol. 56, (2013), pp. 1-9.

[1.33] Damien Pain, Bruce W. Drinkwater, “Detection of Fibre Waviness Using Ultrasonic Array Scattering Data”, Journal of Nondestructive Evaluation, Vol. 32, (2013), pp. 215-227.

[1.34] Rani Elhajjar, Rami Haj-Ali, and Bo-Siou Wei, “An Infrared Thermoelastic Stress Analysis Investigation for Detecting Fiber Waviness in Composite Structures”, Polymer-Plastics Technology and Engineering, Vol. 53, (2014), pp. 1251-1258.

[1.35] Ladislav Janousek, Zhenmao Chen, Noritaka Yusa, Kenzo Miya, “Excitation with phase shifted fields-enhancing evaluation of deep cracks in eddy-current testing”, NDT & E International, Vol. 38, (2005), pp. 508-515.

[1.36] Gerhard Mook, Olaf Hesse, Valentin Uchanin, “Deep Penetrating Eddy Currents and Probes”, Proceedings of European Conference on Nondestructive Testing, (2006).

[1.37] Gerhard Mook, Fritz Michel, Jouri Simonin, “Electromagnetic imaging using probe arrays”, Proceedings of 17th World Conference on Nondestructive Testing, (2008).

[1.38] R. Hughes, Y. Fan, S. Dixon, “Near electrical resonance signal enhancement (NERSE) in eddy-current crack detection”, NDT & E International, Vol. 66, (2014), pp. 82-89.

[1.39] Teodor Dogaru and Stuart T. Smith, “Giant Magnetoresistance-Based Eddy-Current Sensor”, IEEE Transaction on Magnetics, Vol. 37, No. 5, (2001), pp. 3831-3838.

[1.40] Jen-Tzong Jeng, Guan-Shiun Lee, Wen-Chu Liao, Chia-Lun Shu, “Depth-resolved eddy-current detection with GMR magnetometer”, Journal of Magnetism and Magnetic Materials, Vol. 34, (2006), pp. 470-473.

[1.41] Rimond Hamia, Christophe Cordier, Sébastien Saez, and Christophe Dolabdjian, “Eddy-Current Nondestructive Testing Using an Improved GMR Magnetometer and a SingleWire as Inducer: A FEM Performance Analysis”, IEEE Transaction on Magnetics, Vol. 46, No. 10, (2010), pp. 3731-3737.

[1.42] Mehdi Fardmanesh, Farrokh Sarreshtedari, Arash Pourhashemi, Elnaz Ansari, Mohammad A. Vesaghi, Juergen Schubert, Marko Banzet, and Hans-Joachim Krause, “Optimization of NDE Characterization Parameters for a RF-SQUID Based System Using FEM Analysis”, IEEE Transaction on Applied Superconductivity, Vol. 19, No. 3, (2009), pp. 791-795.

[1.43] R. Nagendran, N. Thirumurugan, N. Chinnasamy, M. P. Janawadkar, R. Baskaran, L. S. Vaidhyanathan, C. S. Sundar, “Optimum eddy current excitation frequency for subsurface defect detection in SQUID based non-destructive evaluation”, NDT & E International, Vol. 43, (2010), pp. 713-717.

[1.44] Akira Todoroki, “Skin Effect of Alternating Electric Current in Laminated CFRP”, Advanced Composite Materials, Vol. 21, Nos. 5-6, (2012), pp. 477-489.

[1.45] J.C. Abry, S. Bochard, A. Chateauminois, M. Salvia, G. Giraud, “In situ detection of damage in CFRP laminates by electrical resistance measurements”, Composites Science and Technology, Vol. 59, (1999), pp. 925-935.

[1.46] Jun Cheng, Hongli Ji, Jinhao Qiu, Toshiyuki Takagi, Tetsuya, Uchimoto and Ning Hu, “Novel electromagnetic modeling approach of carbon fiber-reinforced polymer laminate for calculation of eddy currents and eddy current testing signals”, Journal of Composite Materials, Vol. 49, No. 5, (2015), pp. 617-631.

[1.47] X. E. Gros, K. Ogi and K. Takahashi, “Eddy Current, Ultrasonic C-Scan and Scanning Acoustic Microscopy Testing of Delaminated Quasi-Isotropic CFRP Materials: A Case Study”, Journal of Reinforced Plastics and Composites, Vol. 17, No. 5, (1995), pp. 389-405.

[1.48] Kiyoshi Koyama, Hiroshi Hoshikawa and Gouki Koijima, “Eddy Current Nondestructive Testing for Carbon Fiber-Reinforced Composites”, Journal of Pressure Vessel Technology, Vol. 135, (2013), pp. 041501-1-5.

[1.49] Henning Heuer, Martin H. Schulze, Norbert Meyendorf, “High Resolution Inspection of Carbon Fiber Materials by Eddy Current Techniques”, Proceedings of 2nd International Symposium on NDT in Aerospace, (2010).

[1.50] Lu Ma and Manuchehr Soleimani, “Hidden defect identification in carbon fibre reinforced polymer plates using magnetic induction tomography”, Measurement Science and Technology, Vol. 25, (2014), p. 055404.

[1.51] R. Lange and G. Mook, “Structural analysis of CFRP using eddy current methods”, NDT&E International, Vol. 27, No. 5, (1994), pp. 241-248.

[1.52] Gerhard Mook, Rolf Lange and Ole Koeser, “Nondestructive characterisation of carbon fibre reinforced plastics by means of eddy currents”, Composites Science and Technology, Vol. 61, (2001), pp. 865-873.

[1.53] Wuliang Yin, Philip J. Withers, Umesh Sharma and Anthony J. Peyton, “Noncontact Characterization of Carbon-Fiber-Reinforced Plastics Using Multifrequency Eddy Current Sensors”, IEEE Transaction on Instrumentation and Measurement, Vol. 58, No. 3, (2009), pp. 738-743.

[1.54] W Yin, X Li, P J Withers and A J Peyton, “Non-contact characterization of hybrid aluminium/carbon-fibre-reinforced plastic sheets using multi-frequency eddy-current sensors”, Measurement Science and Technology, Vol. 21, (2010), p. 105708.

[1.55] Jun Cheng, Hongli Ji, Jinhao Qiu, Toshiyuki Takagi, Tetsuya Uchimoto, Ning Hu, “Role of interlaminar interface on bulk conductivity and electrical anisotropy of CFRP laminates measured by eddy current method”, NDT & E International, Vol. 68, (2014), pp.1-12.

[1.56] Martin H. Schulze, Henning Heuer, Martin Küttner, Norbert Meyendorf, “High-resolution eddy current sensor system for quality assessment of carbon fiber

materials", Microsystem Technology, Vol. 16, (2010), pp. 791-797.

[1.57] Henning Heuer andMartin H. Schulze, "Eddy Current Testing of Carbon Fiber Materials by High Resolution Directional Sensors", Proceedings of International Workshop SMART MATERIALS, STRUCTURES & NDT in AEROSPACE Conference NDT in Canada 2011, (2011).

[1.58] H. Heuer, M. H. Schulze and N. Meyendorf, "Non-destructive evaluation (NDE) of composites: eddy current techniques", Non-Destructive Evaluation (NDE) of Polymer Matrix Composites, Woodhead publishing, (2013), pp. 34-55.

[1.59] H. Heuer, M. Schulze, M. Pooch, S. Gabler, A. Nocke, G. Bardl, Ch. Cherif, M. Klein, R. Kupke, R. Vetter, F. Lenz, M. Kliem, C. Bülow, J. Goyvaerts, T. Mayer, S. Petrenz, "Review on quality assurance along the CFRP value chain e Nondestructive testing of fabrics, preforms and CFRP by HF radio wave techniques", Composites: part B, Vol. 77, (2015), pp. 494-501.

[1.60] Carsten Schmidt, Cedric Schultz, Patric Weber, Berend Denkena, "Evaluation of eddy current testing for quality assurance and process monitoring of automated fiber placement", Composites: Part B, Vol. 56, (2014), pp. 109-116.

[1.61] Georg Bardl, Andreas Nocke, Chokri Cherif, Matthias Pooch, Martin Schulze, Henning Heuer, Marko Schiller, Richard Kupke, Marcus Klein, "Automated detection of yarn orientation in 3D-draped carbon fiber fabrics and preforms from eddy current data", Composites: Part B, Vol. 96, (2016), pp. 312-324.

[1.62] Koichi Mizukami, Yoshihiro Mizutani, Akira Todoroki, Yoshiro Suzuki, "Detection of in-plane and out-of-plane fiber waviness in unidirectional carbon fiber reinforced composites using eddy current testing", Composites: Part B, Vol. 86, (2016), pp. 84-94.

[1.63] J. R. Bowler, "Eddy current calculations using half-space Green's functions", Journal of Applied Physics, Vol. 61, No. 3, (1987), pp. 833-839.

[1.64] J. R. Bowler and S. A. Jenkins, "Eddy-current probe impedance due to a volumetric flaw", Journal of Applied Physics, Vol. 70, No. 3, (1991), pp. 1107-1114.

[1.65] Stephan J. Norton and John R. Bowler, "Theory of eddy current inversion", Journal of Applied Physics, Vol. 73, No. 2, (1993), pp. 501-512.

[1.66] J. R. Bowler, "Eddy-current interaction with an ideal crack. I. The forward problem", Journal of Applied Physics, Vol. 75, No. 12, (1994), pp. 8128-8137.

[1.67] Jozsef Pavo and Kenzo Miya, "Reconstruction of Crack Shape by Optimization Using Eddy Current Field Measurement", IEEE Transaction on Magnetics, Vol. 30, No. 5, (1994), pp. 3407-3410.

[1.68] Haoyu Huang, Nozomu Sakurai, Toshiyuki Takagi, Tetsuya Uchimoto, “Design of an eddy-current array probe for crack sizing in steam generator tubes”, NDT & E International, Vol. 36, (2003), pp. 515-522.

Chapter 2

Derivation of analytical solutions to the eddy current problem of CFRP

2.1 Background

Because carbon fiber is electrically conductive, eddy currents are induced in CFRP when the CFRP is exposed to an alternating magnetic field generated by a drive current. Because CFRP has anisotropic electrical conductivity, the distribution of the eddy current in CFRP is more complicated than that in metal. Although distributions of eddy current in CFRP have been investigated in FEM analyses, the contribution of anisotropic conductivity to the eddy current distribution has not been expressed in the form of analytical solutions.

Analytical solutions to drive current-eddy current problem were first derived by Dodd and Deeds [2.1]. Dodd and Deeds derived analytical solutions for the electromagnetic field when a circular drive current is placed above an isotropic conductive slab. Luquire et al. derived analytical solutions for eddy current in multilayered plates [2.2]. These studies can be used only for isotropic conductive plate or layered isotropic plates. Analytical solutions for eddy current in CFRP have not been derived because difficulties arise when treating the anisotropy of electrical conductivity.

Because the unidirectional ply in CFRP has strong anisotropy of electrical conductivity in longitudinal, transverse and thickness directions [2.3], a line drive current has the potential to effectively induce eddy currents with higher intensity than those induced by a circular drive current [2.4]. Todoroki obtained general expressions of the skin depth of eddy current in CFRP assuming that both the electric field and magnetic field have only one directional component [2.5]. This approximate calculation can be used to estimate the skin depth of the eddy current induced by a line current. Although the approximation of Todoroki can be used to easily calculate the skin depth of eddy current in CFRP even in cases of cross-ply laminates, it cannot be used to

calculate the amplitude and phase of the eddy current.

In this chapter, analytical solutions for the electromagnetic field are derived assuming that a line drive current is placed above a CFRP plate. The physical background of the derived analytical solutions is discussed to clarify the contribution of anisotropic electrical conductivity to the eddy current distribution. The penetration depth of eddy current calculated from the derived analytical solution is compared with the general expression for the skin depth, and the difference between them is discussed.

2.2 Derivation of analytical solutions for the electromagnetic field

2.2.1 Governing equations for the electromagnetic field

Analytical solutions for the electromagnetic field in the drive current-eddy current problem are derived by solving Maxwell's equations. Maxwell's equations are written as follows.

$$\nabla \cdot \boldsymbol{B} = 0 \tag{2.1}$$

$$\nabla \times \boldsymbol{E} = -\frac{\partial \boldsymbol{B}}{\partial t} \tag{2.2}$$

$$\nabla \times \boldsymbol{H} = \boldsymbol{J} + \frac{\partial \boldsymbol{D}}{\partial t} \tag{2.3}$$

$$\nabla \cdot \boldsymbol{D} = \rho \tag{2.4}$$

Here, $\boldsymbol{B}$, $\boldsymbol{H}$, $\boldsymbol{D}$ and $\boldsymbol{E}$ are the magnetic flux density, magnetic field, electric flux density and electric field. ρ and $\boldsymbol{J}$ are the electric charge and current density. We now assume that the magnetic flux density is expressed as a rotation of vector $\boldsymbol{A}$ as in Eq. (2.5).

$$\boldsymbol{B} = \nabla \times \boldsymbol{A} \tag{2.5}$$

Vector $\boldsymbol{A}$ is referred to as the magnetic vector potential. Because div(rot$\boldsymbol{X}$) is zero for any vector $\boldsymbol{X}$, magnetic flux density $\boldsymbol{B}$ in Eq. (2.5) automatically satisfies Eq. (2.1). By substituting Eq. (2.5) into Eq. (2.2), we obtain Eq. (2.6).

$$\nabla \times \left(\boldsymbol{E} + \frac{\partial \boldsymbol{A}}{\partial t} \right) = 0 \tag{2.6}$$

Because rot(grad$X$) becomes zero for arbitrary scalar X, the term in the brackets in Eq. (2.6) can be expressed as Eq. (2.7).

$$\boldsymbol{E} + \frac{\partial \boldsymbol{A}}{\partial t} = -\nabla \phi \tag{2.7}$$

ϕ is referred to as the electric scalar potential. Using Eqs. (2.5) and (2.7), Eqs. (2.3) and (2.4) can be rewritten as follows.

$$\left(\Delta-\mu_0\varepsilon_0\frac{\partial^2}{\partial t^2}\right)\boldsymbol{A}-\nabla\left(\nabla\cdot\boldsymbol{A}+\mu_0\varepsilon_0\frac{\partial\phi}{\partial t}\right)=-\mu_0\boldsymbol{J} \tag{2.8}$$

$$\Delta\phi+\nabla\cdot\frac{\partial\boldsymbol{A}}{\partial t}=-\frac{\rho}{\varepsilon_0} \tag{2.9}$$

Here, μ_0 and ε_0 are the magnetic permeability in a vacuum and permittivity in a vacuum. The following relationships are used in the derivation of Eqs. (2.8) and (2.9).

$$\boldsymbol{B}=\mu_0\boldsymbol{H} \tag{2.10}$$

$$\boldsymbol{D}=\varepsilon_0\boldsymbol{E} \tag{2.11}$$

The magnetic permeability of CFRP is isotropic and equal to μ_0. When the drive frequency is less than 10 MHz, permittivity is also isotropic and its value is equal to that in a vacuum [2.6].

We now apply Coulomb gauge transformations to rewrite the governing equations in a simpler form. Coulomb gauge transformations are written as follows.

$$\boldsymbol{A}'=\boldsymbol{A}+\nabla\chi \tag{2.12}$$

$$\phi'=\phi-\frac{\partial\chi}{\partial t} \tag{2.13}$$

When $\boldsymbol{A}$ and ϕ are solutions to Eqs. (2.8) and (2.9), $\boldsymbol{A}'$ and ϕ' are also solutions. Because this is true for arbitrary χ, a convenient χ can be selected to simplify Eqs. (2.8) and (2.9). The Coulomb gauge assumes the following relationship to eliminate $\nabla\cdot\boldsymbol{A}$ in Eqs. (2.8) and (2.9).

$$\Delta\chi=-\nabla\cdot\boldsymbol{A} \tag{2.14}$$

Using the Coulomb gauge, the governing equations are rewritten as follows.

$$\left(\Delta-\mu_0\varepsilon_0\frac{\partial^2}{\partial t^2}\right)\boldsymbol{A}-\mu_0\varepsilon_0\nabla\frac{\partial\phi}{\partial t}=-\mu_0\boldsymbol{J} \tag{2.15}$$

$$\Delta\phi = -\frac{\rho}{\varepsilon_0} \tag{2.16}$$

The purpose of the present study is to solve Eqs. (2.15) and (2.16) considering anisotropy in electrical conductivity.

2.2.2 Analytical solutions for eddy current in isotropic materials

First, we derive analytical solutions for the spatial distribution of vector potential ***A*** assuming that a line drive current with infinite length is placed above an isotropic conductive material. In this case, the electromagnetic field can be calculated when the spatial distribution of vector potential ***A*** is given, and the eddy current distribution can be obtained. This is because there is no electric charge and thus no electric field originating from electric charge. Analytical solution to the eddy current distribution in an isotropic material is later extended to the case of CFRP.

Fig. 2.1 shows the analytical model used for derivation of the analytical solutions for the vector potential. In Fig. 2.1, a delta-function line drive current is placed above an isotropic conductive plate with lift-off l at $y = y_0$. The thickness of the conductive plate is c and the conductivity of the plate is σ. The line drive current is directed in the x

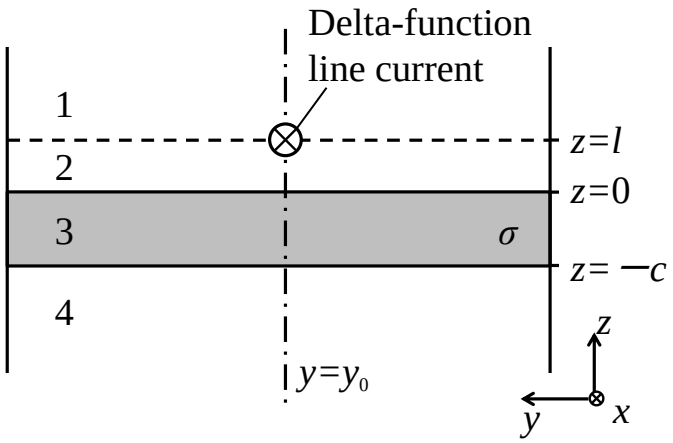

Fig. 2.1 Analytical model of a delta-function line current above a conductive plate.

direction in Fig. 2.1, and is a sinusoidal electric current with amplitude *I* and frequency *f*. We divide the analytical model in Fig. 2.1 into four regions 1–4. Region 3 is the isotropic conductive material in which eddy current is induced. It is assumed that all regions are infinite in the *x*-*y* plane.

Region 1: Semi-infinite space above the line drive current (air)

Region 2: Space between the drive current and conductive material (air)

Region3: Isotropic conductive material with thickness *c* and conductivity σ

Region4: Semi-infinite space below the conductive material (air)

According to Eq. (2.15), the differential equation of vector potential $\boldsymbol{A}$ is given by Eq. (2.17).

$$\nabla^2 \boldsymbol{A} + \mu_0 \varepsilon_0 \frac{\partial}{\partial t}\left(-\frac{\partial \boldsymbol{A}}{\partial t} - \nabla \phi \right) = -\mu_0 \sigma \left(-\frac{\partial \boldsymbol{A}}{\partial t} - \nabla \phi \right) - \mu_0 \boldsymbol{i}_0 \tag{2.17}$$

Here, $\boldsymbol{i}_0$ is the drive current density vector and ω is the angular drive frequency ($\omega = 2\pi f$). The first term on the right side of Eq. (2.17) is derived from the following relationship between the electrical conductivity and electric field.

$$\boldsymbol{J} = \sigma \boldsymbol{E} = \sigma \left(-\frac{\partial \boldsymbol{A}}{\partial t} - \nabla \phi \right) \tag{2.18}$$

When the drive frequency is below approximately 10MHz, the displacement current becomes negligible [2.1] and we get Eq. (2.19).

$$\nabla^2 \boldsymbol{A} = -\mu_0 \sigma \left(-\frac{\partial \boldsymbol{A}}{\partial t} - \nabla \phi \right) - \mu_0 \boldsymbol{i}_0 \tag{2.19}$$

Because a sinusoidal excitation field is assumed in this case, Eq. (2.19) can be written in the complex form shown in Eq. (2.20).

$$\nabla^2 \boldsymbol{A} = -\mu_0 \sigma \left(-j\omega A - \nabla \phi \right) - \mu_0 \boldsymbol{i}_0 \tag{2.20}$$

Here, *j* is an imaginary unit. The drive current density vector $\boldsymbol{i}_0$ is written as Eq. (2.21).

$$\boldsymbol{i}_0 = \left(I\delta(y - y_0)\delta(z - l), \quad 0, \quad 0 \right)^T \tag{2.21}$$

Because the drive current has only an x directional component, the vector potential also has only an x component, A_x. y and z components of the vector potential are zero. Hence, we get Eq. (2.22).

$$\frac{\partial^2 A_x}{\partial x^2} + \frac{\partial^2 A_x}{\partial y^2} + \frac{\partial^2 A_x}{\partial z^2} - j\omega\mu_0\sigma A_x - \mu_0\sigma\frac{\partial \phi}{\partial x} + \mu_0 I\delta(y - y_0)\delta(z - l) = 0 \tag{2.22}$$

Differentiation with respect to x can be eliminated because of the model's infinite length in the x direction.

$$\frac{\partial^2 A_x}{\partial y^2} + \frac{\partial^2 A_x}{\partial z^2} - j\omega\mu_0\sigma A_x + \mu_0 I\delta(y - y_0)\delta(z - l) = 0 \tag{2.23}$$

Eq. (2.23) is the well-known Helmholtz equation with two variables, and it can be solved by the separation of variables. We define a general solution for A_x in region k (k = 1, 2, 3, 4) as $A^{(k)}(y,z)$. $A^{(k)}(y,z)$ is expressed as follows.

$$A^{(k)}(y, z) = \int_0^\infty \left(A_k e^{\alpha_k z} + B_k e^{-\alpha_k z}\right)\cos\alpha(y - y_0)d\alpha \tag{2.24}$$

where

$$\alpha_k = \begin{cases} \alpha & (k = 1,2,4) \\ \left(\alpha^2 + j\omega\mu_0\sigma\right)^{1/2} & (k = 3) \end{cases} \tag{2.25}$$

In Eq. (2.24), we have eight unknowns: A_1, A_2, A_3, A_4, B_1, B_2, B_3 and B_4. However, when we consider finite $A^{(k)}(y,z)$ at $z \rightarrow \pm\infty$, we get $A_1 = B_4 = 0$. In determining the six remaining unknowns, we use boundary conditions of continuity and Ampere's law to obtain the six following equations.

$$A^{(1)}(y,l) = A^{(2)}(y,l) \tag{2.26}$$

$$\left.\frac{\partial A^{(1)}}{\partial z}\right|_{z=l} = \left.\frac{\partial A^{(2)}}{\partial z}\right|_{z=l} - \mu_0 I\delta(y - y_0) \tag{2.27}$$

$$A^{(2)}(y,0) = A^{(3)}(y,0) \tag{2.28}$$

$$\left.\frac{\partial A^{(2)}}{\partial z}\right|_{z=0} = \left.\frac{\partial A^{(3)}}{\partial z}\right|_{z=0} \tag{2.29}$$

$$A^{(3)}(y,-c) = A^{(4)}(y,-c) \tag{2.30}$$

$$\left.\frac{\partial A^{(3)}}{\partial z}\right|_{z=-c} = \left.\frac{\partial A^{(4)}}{\partial z}\right|_{z=-c} \tag{2.31}$$

By substituting Eq. (2.24) into Eq. (2.26), we obtain Eq. (2.32).

$$\int_0^\infty B_1 e^{-\alpha l}\cos\alpha(y-y_0)d\alpha = \int_0^\infty \left(A_2 e^{\alpha l} + B_2 e^{-\alpha l}\right)\cos\alpha(y-y_0)d\alpha \tag{2.32}$$

Because both sides of Eq. (2.32) are expressed in integral form, it is difficult to solve the unknowns. We multiply both sides of Eq. (2.32) by $\cos\alpha'(y-y_0)d(y-y_0)$ and integrate them from zero to ∞. Subsequently, we introduce the Fourier integral theorem in Eq. (2.33) to simplify the integral equation.

$$f(\alpha') = \frac{2}{\pi}\int_0^\infty f(\alpha)\left(\int_0^\infty \cos\alpha(y-y_0)\cos\alpha'(y-y_0)d(y-y_0)\right)d\alpha \tag{2.33}$$

By applying Eq. (2.33) to Eq. (2.32), we get Eq. (2.34).

$$B_1 e^{-\alpha l} = A_2 e^{\alpha l} + B_2 e^{-\alpha l} \tag{2.34}$$

Similarly, integral equations of boundary conditions Eqs. (2.27)–(2.31) can be simplified as follows.

$$-B_1\alpha e^{-\alpha l} = A_2\alpha e^{\alpha l} - B_2\alpha e^{-\alpha l} - \frac{\mu_0 I}{\pi} \tag{2.35}$$

$$A_2 + B_2 = A_3 + B_3 \tag{2.36}$$

$$A_2\alpha - B_2\alpha = A_3\alpha_3 - B_3\alpha_3 \tag{2.37}$$

$$A_3 e^{-\alpha_3 c} + B_3 e^{\alpha_3 c} = A_4 e^{-\alpha c} \tag{2.38}$$

$$A_3\alpha_3 e^{-\alpha_3 c} - B_3\alpha_3 e^{\alpha_3 c} = A_4\alpha e^{-\alpha c} \tag{2.39}$$

We now have the six unknowns A_2, A_3, A_4, B_1, B_2 and B_3 and the six equations Eqs. (2.34)–(2.39). The six unknowns can be obtained by solving the six equations.

$$A_2 = \frac{\mu_0 I e^{-\alpha l}}{2\pi\alpha} \tag{2.40}$$

$$A_3 = \frac{\mu_0 I}{\pi}\cdot\frac{(\alpha_3+\alpha)e^{-\alpha l}}{(\alpha_3+\alpha)^2 - (\alpha_3-\alpha)^2 e^{-2\alpha_3 c}} \tag{2.41}$$

$$A_4 = \frac{\mu_0 I}{\pi}\cdot\frac{2\alpha_3 e^{-\alpha l}e^{(\alpha-\alpha_3)c}}{(\alpha_3+\alpha)^2 - (\alpha_3-\alpha)^2 e^{-2\alpha_3 c}} \tag{2.42}$$

$$B_1 = \frac{\mu_0 I}{2\pi\alpha}\left\{e^{\alpha l} + \frac{\left(\alpha^2 - {\alpha_3}^2\right)\left(1-e^{-2\alpha_3 c}\right)e^{-\alpha l}}{\left(\alpha_3+\alpha\right)^2 - \left(\alpha_3-\alpha\right)^2 e^{-2\alpha_3 c}}\right\} \tag{2.43}$$

$$B_2 = \frac{\mu_0 I}{2\pi\alpha}\cdot\frac{\left(\alpha^2 - {\alpha_3}^2\right)\left(1-e^{-2\alpha_3 c}\right)e^{-\alpha l}}{\left(\alpha_3+\alpha\right)^2 - \left(\alpha_3-\alpha\right)^2 e^{-2\alpha_3 c}} \tag{2.44}$$

$$B_3 = \frac{\mu_0 I}{\pi}\cdot\frac{\left(\alpha_3-\alpha\right)e^{-2\alpha_3 c}e^{-\alpha l}}{\left(\alpha_3+\alpha\right)^2 - \left(\alpha_3-\alpha\right)^2 e^{-2\alpha_3 c}} \tag{2.45}$$

By substituting Eqs. (2.40)–(2.45) into Eq. (2.24), solutions to the vector potential in region 1, 2, 3 and 4 are given as follows.

$$A^{(1)}(y,z) = \frac{\mu_0 I}{2\pi}\int_0^\infty \frac{1}{\alpha}\left\{e^{\alpha l} + \frac{\left(\alpha^2 - {\alpha_3}^2\right)\left(1-e^{-2\alpha_3 c}\right)e^{-\alpha l}}{\left(\alpha_3+\alpha\right)^2 - \left(\alpha_3-\alpha\right)^2 e^{-2\alpha_3 c}}\right\}e^{-\alpha z}\cos\alpha(y-y_0)d\alpha \tag{2.46}$$

$$A^{(2)}(y,z) = \frac{\mu_0 I}{2\pi}\int_0^\infty \frac{1}{\alpha}\left\{e^{\alpha z} + \frac{\left(\alpha^2 - {\alpha_3}^2\right)\left(1-e^{-2\alpha_3 c}\right)}{\left(\alpha_3+\alpha\right)^2 - \left(\alpha_3-\alpha\right)^2 e^{-2\alpha_3 c}}e^{-\alpha z}\right\}e^{-\alpha l}\cos\alpha(y-y_0)d\alpha \tag{2.47}$$

$$A^{(3)}(y,z) = \frac{\mu_0 I}{\pi}\int_0^\infty \left\{\frac{\left(\alpha_3+\alpha\right)e^{\alpha_3 z} + \left(\alpha_3-\alpha\right)e^{-2\alpha_3 c}e^{-\alpha_3 z}}{\left(\alpha_3+\alpha\right)^2 - \left(\alpha_3-\alpha\right)^2 e^{-2\alpha_3 c}}\right\}e^{-\alpha l}\cos\alpha(y-y_0)d\alpha \tag{2.48}$$

$$A^{(4)}(y,z) = \frac{\mu_0 I}{\pi}\int_0^\infty \frac{2\alpha_3 e^{-\alpha l}e^{(\alpha-\alpha_3)c}}{\left(\alpha_3+\alpha\right)^2 - \left(\alpha_3-\alpha\right)^2 e^{-2\alpha_3 c}}e^{\alpha z}\cos\alpha(y-y_0)d\alpha \tag{2.49}$$

Now we assume that the drive current has a rectangular cross-section. Fig. 2.2 shows the analytical model of a line current with a rectangular cross-section above a conductive plate. The rectangular cross-section is a rectangular domain in the *y*-*z* plane

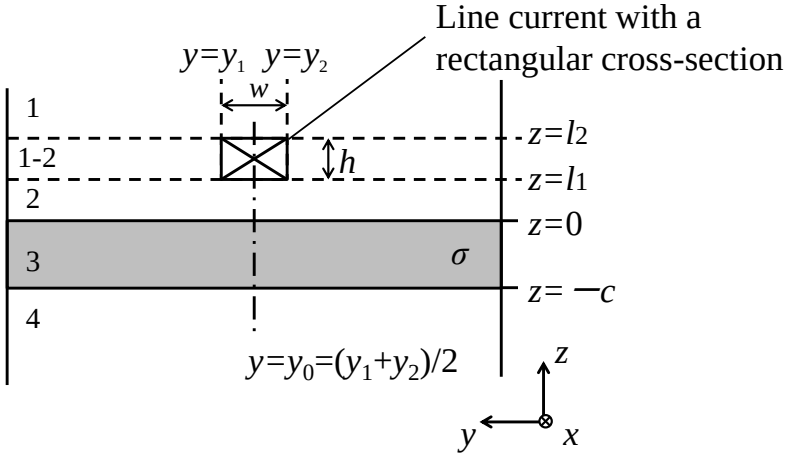

Fig. 2.2 Analytical model of a rectangular cross-section line current above a conductive plate.

bordered by $y = y_1$, $y = y_2$, $z = l_1$ and $z = l_2$ ($y_1 < y_2$, $l_1 < l_2$) as shown in Fig. 2.2. We denote the vector potential induced by the drive current with the rectangular cross-section in each region as $A_{\mathrm{rec}}^{(k)}(y,z)$ (k = 1, 2, 3 ,4). $A_{\mathrm{rec}}^{(k)}(y,z)$ can be calculated using the following equation.

$$A_{\mathrm{rec}}^{(k)}(y,z) = \int_{y_1}^{y_2}\int_{l_1}^{l_2} A^{(k)} dl dy_0 \tag{2.50}$$

In Eq. (2.50), the current density of drive current i_0 is substituted into I in Eqs. (2.46)–(2.49) assuming that the applied current density in the rectangular cross-section is constant over the rectangular domain. The vector potentials in regions 1, 2, 3 and 4 in Fig. 2.2 are calculated as follows using Eq. (2.50).

$$A_{\mathrm{rec}}^{(1)}(y,z) = \frac{\mu_0 i_0}{2\pi}\int_0^\infty \frac{-1}{\alpha^3}\left\{(e^{\alpha l_2}-e^{\alpha l_1}) - \frac{\left(\alpha^2-{\alpha_3}^2\right)\left(1-e^{-2\alpha_3 c}\right)(e^{-\alpha l_2}-e^{-\alpha l_1})}{(\alpha_3+\alpha)^2-(\alpha_3-\alpha)^2 e^{-2\alpha_3 c}}\right\}e^{-\alpha z} \times\{\sin\alpha(y-y_2)-\sin\alpha(y-y_1)\}d\alpha \tag{2.51}$$

$$A_{\mathrm{rec}}^{(2)}(y,z) = \frac{\mu_0 i_0}{2\pi}\int_0^\infty \frac{1}{\alpha^3}\left\{e^{\alpha z} + \frac{\left(\alpha^2-{\alpha_3}^2\right)\left(1-e^{-2\alpha_3 c}\right)}{(\alpha_3+\alpha)^2-(\alpha_3-\alpha)^2 e^{-2\alpha_3 c}}e^{-\alpha z}\right\}(e^{-\alpha l_2}-e^{-\alpha l_1}) \times\{\sin\alpha(y-y_2)-\sin\alpha(y-y_1)\}d\alpha \tag{2.52}$$

$$A_{\mathrm{rec}}^{(3)}(y,z) = \frac{\mu_0 i_0}{\pi}\int_0^\infty \frac{1}{\alpha^2}\left\{\frac{(\alpha_3+\alpha)e^{\alpha_3 z}+(\alpha_3-\alpha)e^{-2\alpha_3 c}e^{-\alpha_3 z}}{(\alpha_3+\alpha)^2-(\alpha_3-\alpha)^2 e^{-2\alpha_3 c}}\right\}(e^{-\alpha l_2}-e^{-\alpha l_1}) \times\{\sin\alpha(y-y_2)-\sin\alpha(y-y_1)\}d\alpha \tag{2.53}$$

$$A_{\mathrm{rec}}^{(4)}(y,z) = \frac{\mu_0 i_0}{\pi}\int_0^\infty \frac{1}{\alpha^2}\frac{2\alpha_3 e^{(\alpha-\alpha_3)c}(e^{-\alpha l_2}-e^{-\alpha l_1})}{(\alpha_3+\alpha)^2-(\alpha_3-\alpha)^2 e^{-2\alpha_3 c}}e^{\alpha z} \times\{\sin\alpha(y-y_2)-\sin\alpha(y-y_1)\}d\alpha \tag{2.54}$$

To calculate the vector potential between the top and bottom of the line current (region 1–2 in Fig. 2.2), we need a special treatment. The vector potential in region 1–2 $A_{\mathrm{rec}}^{(1-2)}(y,z)$ is calculated from the sum of $A_{\mathrm{rec}}^{(1)}\big|_{l_2=z}$ and $A_{\mathrm{rec}}^{(2)}\big|_{l_1=z}$. By substituting l_2 = z in Eq. (2.51) and $l_1 = z$ in Eq. (2.52), we obtain Eq. (2.55).

$$A_{\mathrm{rec}}^{(1-2)}(y,z) = A_{\mathrm{rec}}^{(1)}\Big|_{l_2=z} + A_{\mathrm{rec}}^{(2)}\Big|_{l_1=z}$$

$$= \frac{\mu_0 i_0}{2\pi}\int_0^\infty \frac{-1}{\alpha^3}\left\{(2-e^{-\alpha(l_2-z)}-e^{-\alpha(z-l_1)}) - \frac{\left(\alpha^2-{\alpha_3}^2\right)\left(1-e^{-2\alpha_3 c}\right)\left(e^{-\alpha(z+l_2)}-e^{-\alpha(z+l_1)}\right)}{(\alpha_3+\alpha)^2-(\alpha_3-\alpha)^2 e^{-2\alpha_3 c}}\right\} \times\left\{\sin\alpha(y-y_2)-\sin\alpha(y-y_1)\right\}d\alpha \tag{2.55}$$

Eddy current density vector $\boldsymbol{J}$ in the conductive plate of region 3 can be calculated using Eq. (2.56).

$$\boldsymbol{J} = \sigma\boldsymbol{E} = -j\omega\sigma\boldsymbol{A} = -j\omega\sigma\begin{pmatrix} A_{\mathrm{rec}}^{(3)}(y,z) \\ 0 \\ 0 \end{pmatrix} \tag{2.56}$$

Since there is no electric charge, the electric field generated by the potential gradient is not included in Eq. (2.56).

2.2.3 Analytical solutions for eddy current in unidirectional CFRPs

The analytical solution for eddy current in an isotropic material is extended to the case of CFRP. We assume that region 3 in the analytical model of Fig. 2.1 is unidirectional CFRP. We define the x direction in the model as the 0° direction. When we assume that the fiber orientation of CFRP is θ around the z axis, electrical conductivity is expressed as the matrix in Eq. (2.57) [2.7].

$$\overline{\overline{\sigma}} = \begin{pmatrix} \sigma_0\cos^2\theta+\sigma_{90}\sin^2\theta & \dfrac{\sigma_0-\sigma_{90}}{2}\sin 2\theta & 0 \\ \dfrac{\sigma_0-\sigma_{90}}{2}\sin 2\theta & \sigma_0\sin^2\theta+\sigma_{90}\cos^2\theta & 0 \\ 0 & 0 & \sigma_t \end{pmatrix} \tag{2.57}$$

Here, $\overline{\overline{\sigma}}$ is the electrical conductivity matrix and σ_0, σ_{90} and σ_t are the CFRP conductivities in the fiber direction, transverse direction and thickness direction, respectively. The differential equation of the vector potential that takes the anisotropy of conductivity into consideration can be written as follows.

$$\nabla^2 \boldsymbol{A} = -\mu_0 \overline{\overline{\sigma}}\left(-j\omega \boldsymbol{A} - \nabla\phi\right) - \mu_0 \boldsymbol{i}_0 \tag{2.58}$$

Because Eq. (2.58) is generally a simultaneous differential equation, it is difficult to derive the analytical solutions for the vector potential. We now assume that the drive current is directed in the x direction and the angle θ = 0° or 90°. Drive current flows in the fiber direction or the transverse direction as displayed in Fig. 2.3 when θ = 0° or 90°. By substituting θ = 0° or 90° into Eq. (2.57), (1,2) and (2,1) components in conductivity matrix $\overline{\overline{\sigma}}$ become zero. Thus, the linkage between the x directional component and y directional component of the vector potential can be eliminated. In this case, the y directional component and z directional component of the vector potential become zero like the vector potential for an isotropic material. When the drive current is directed in the fiber direction (θ = 0°), the differential equation of the x directional component of the vector potential A_x is written as Eq. (2.59).

$$\frac{\partial^2 A_x}{\partial y^2} + \frac{\partial^2 A_x}{\partial z^2} - j\omega\mu_0\sigma_0 A_x + \mu_0 I\delta(y - y_0)\delta(z - l) = 0 \tag{2.59}$$

Similarly, when the drive current is directed in the transverse direction (θ = 90°), the differential equation is expressed as Eq. (2.60).

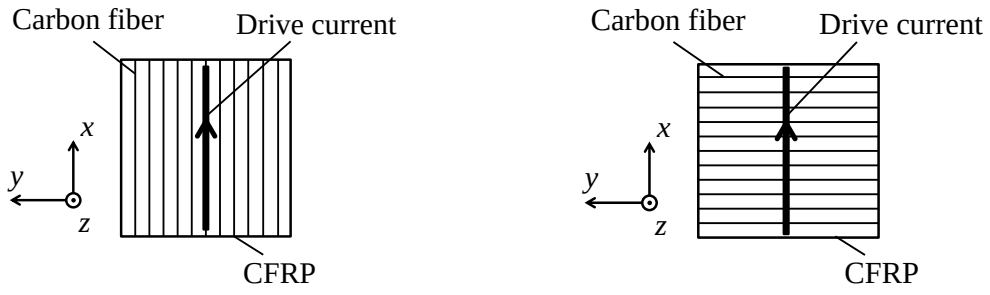

(a) (b)

Fig. 2.3 Schematic illustrations of the relationship between the direction of the drive current and that of carbon fibers: (a) drive current in the fiber direction (θ = 0°), (b) drive current in the transverse direction (θ = 90°).

$$\frac{\partial^2 A_x}{\partial y^2}+\frac{\partial^2 A_x}{\partial z^2}-j\omega\mu_0\sigma_{90}A_x+\mu_0 I\delta(y-y_0)\delta(z-l)=0 \tag{2.60}$$

Here, y_0 is the y location of the delta-function drive current. Eqs. (2.59) and (2.60) are differential equations obtained by substituting $\sigma = \sigma_0$ or $\sigma = \sigma_{90}$ into Eq. (2.23). Therefore, when the drive current is directed in the fiber direction or transverse direction, the eddy current distribution in unidirectional CFRP can be calculated by substituting the conductivity in the drive current direction into Eq. (2.56). More importantly, this indicates that the eddy current distribution in CFRP depends only on conductivity in the drive current direction and is independent of conductivity in other directions. In the case of woven CFRP that has macroscopically in-plane isotropy of conductivity, the (1,2) and (2,1) components in the conductivity matrix of Eq. (2.57) can be eliminated by substituting in-plane conductivity σ_{xy} into σ_0 and σ_{90}. Thus, the eddy current distribution in woven CFRP can also be calculated by substituting σ_{xy} into σ in Eq. (2.56).

2.2.4 Analytical solutions for eddy current in cross-ply CFRPs

Analytical solutions for the eddy current distribution in a cross-ply laminate that is composed of 0° and 90° layers can be derived employing the method described above. Fig. 2.4 shows an analytical model of a delta-function line current placed above a three-layer cross-ply laminate. It is assumed that the fiber orientations of the three layers θ_3, θ_4 and θ_5 (regions 3, 4 and 5 in Fig. 2.4) are 0° or 90°. The differential equation of vector potential in region k (k = 3, 4, 5) is written as Eq. (2.61).

$$\nabla^2\boldsymbol{A}=-\mu_0\begin{pmatrix}\sigma_0\cos^2\theta_k+\sigma_{90}\sin^2\theta_k & \frac{\sigma_0-\sigma_{90}}{2}\sin 2\theta_k & 0\\ \frac{\sigma_0-\sigma_{90}}{2}\sin 2\theta_k & \sigma_0\sin^2\theta_k+\sigma_{90}\cos^2\theta_k & 0\\ 0 & 0 & \sigma_t\end{pmatrix}\left(-j\omega\boldsymbol{A}-\nabla\phi\right)-\mu_0\boldsymbol{i}_0 \tag{2.61}$$

When θ_k = 0° or 90°, y and z directional components of the vector potential are zero and the vector potential has only the x directional component. x directional component of vector potential A_x depends only on conductivity in the drive current direction. Considering the infinite length of the model in the x direction, the differential equation of A_x can be obtained.

$$\frac{\partial^2 A_x}{\partial y^2} + \frac{\partial^2 A_x}{\partial z^2} - j\omega\mu_0\sigma_k A_x + \mu_0 I\delta(y - y_0)\delta(z - l) = 0 \tag{2.62}$$

Here, σ_k is region k's electrical conductivity in the drive current direction (k = 3, 4, 5). The general solution for A_x in region k ($A^{(k)}(y,z)$) is expressed as Eq. (2.63).

$$A^{(k)}(y,z) = \int_0^\infty \left(A_k e^{\alpha_k z} + B_k e^{-\alpha_k z}\right)\cos\alpha(y - y_0)d\alpha \tag{2.63}$$

where,

$$\alpha_k = \begin{cases} \alpha & (k = 1,2,6) \\ \left(\alpha^2 + j\omega\mu_0\sigma_k\right)^{1/2} & (k = 3,4,5) \end{cases} \tag{2.64}$$

Unknown variables A_k and B_k can be obtained by considering the boundary conditions

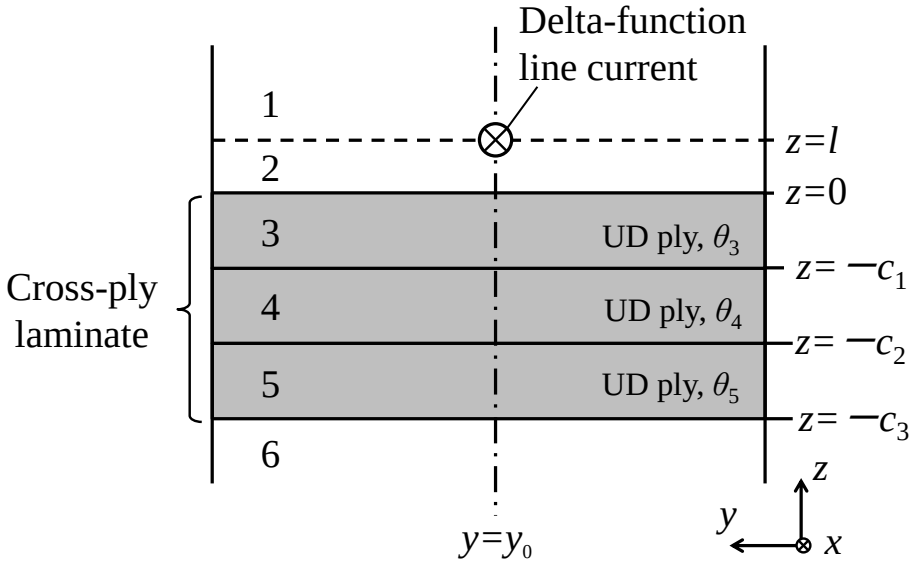

Fig. 2.4 Analytical model of a delta-function drive current placed above a cross-ply CFRP laminate.

of continuity and Ampere's law in the same way as for unidirectional CFRP. The solution can be extended to the case of line drive current with a rectangular cross-section shown in Fig. 2.5.

Eddy current distributions in three-layer cross-ply laminate were calculated employing the analytical model shown in Fig. 2.5. Table 2.1 gives the input parameters used to calculate the eddy current distribution. Fig. 2.6 shows the eddy current distribution in a cross-ply laminate with a stacking sequence of [0/90/0]. Fig. 2.6 presents the distribution of the amplitude of the *x* directional eddy current distribution. It is seen that eddy currents are concentrated in 0° layers, while the amplitude of eddy current in the 90° layer is low. This is because electrical conductivity in transverse direction of unidirectional ply is much smaller than that in longitudinal direction. When plies in CFRP have a fiber orientation of 0° or 90°, the vector potential in each ply has only one directional component corresponding to the drive current direction. This indicates that the electric field is also directed in the drive current direction. Because

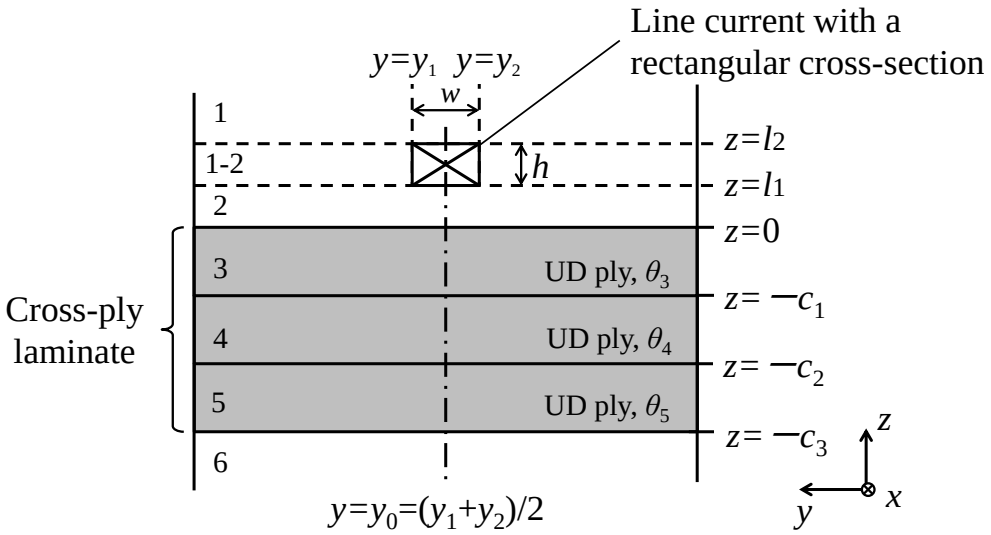

Fig. 2.5 Analytical model of a drive current with a rectangular cross-section placed above a cross-ply CFRP laminate.

eddy current vector is calculated as a product of the electrical conductivity and electric field, layers that have low conductivity in the drive current direction have a small amplitude of eddy current. This explains why eddy current in the 90° layer is small in Fig. 2.6. Fig. 2.7 shows the eddy current distribution in a cross-ply laminate with a stacking sequence of [90/0/90]. Because of the physical background described above, eddy currents are concentrated only in the 0° layer. This result shows that the amplitude of eddy current in multilayered CFRP does not always have the maximum value at the surface. The results in Figs. 2.6 and 2.7 reveal that layers in which eddy currents are induced can be selected by changing the in-plane azimuth of the line drive current.

Table 2.1 Input parameters used to calculate the eddy current distribution in three-layer cross-ply laminate

Variables	Value
Width of the drive current: w [mm]	5
Height of the drive current: h [mm]	2
Lift-off: l_1 [mm]	1
Depth of bottom surface of 1st layer: c_1 [mm]	1
Depth of bottom surface of 2nd layer: c_2 [mm]	3
Depth of bottom surface of 3rd layer: c_3 [mm]	4
Drive current amplitude: I [A]	1
Drive frequency: f [Hz]	1000000
Fiber direction conductivity: σ_0 [S/m]	34120 [2.3]
Transverse direction conductivity: σ_{90} [S/m]	24 [2.3]
Magnetic permeability: μ_0 [H/m]	1.26×10^{-6}

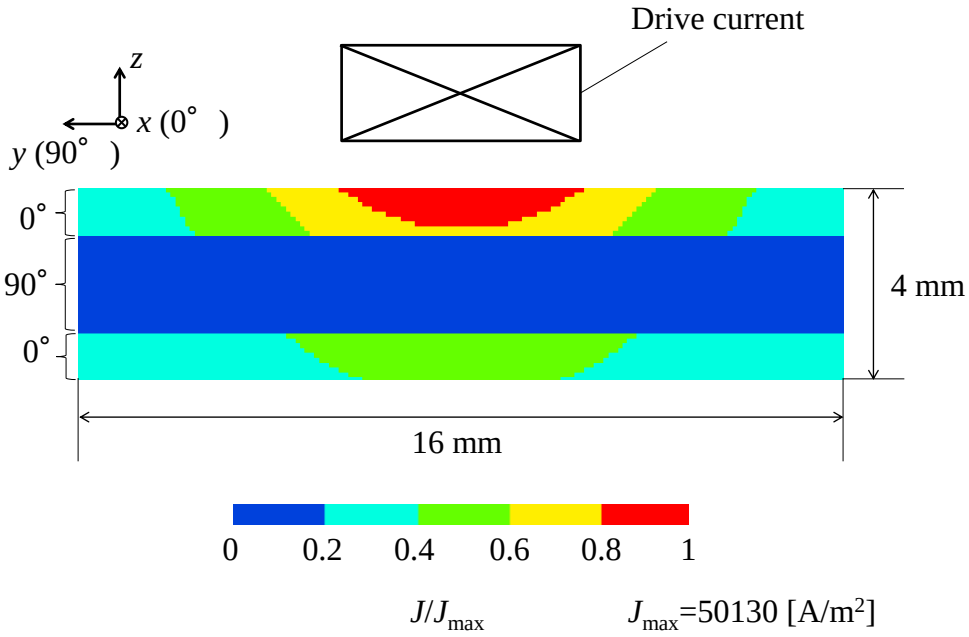

Fig. 2.6 Distribution of eddy current in the *x* direction when a line drive current is placed above cross-ply CFRP with the stacking sequence of [0/90/0].

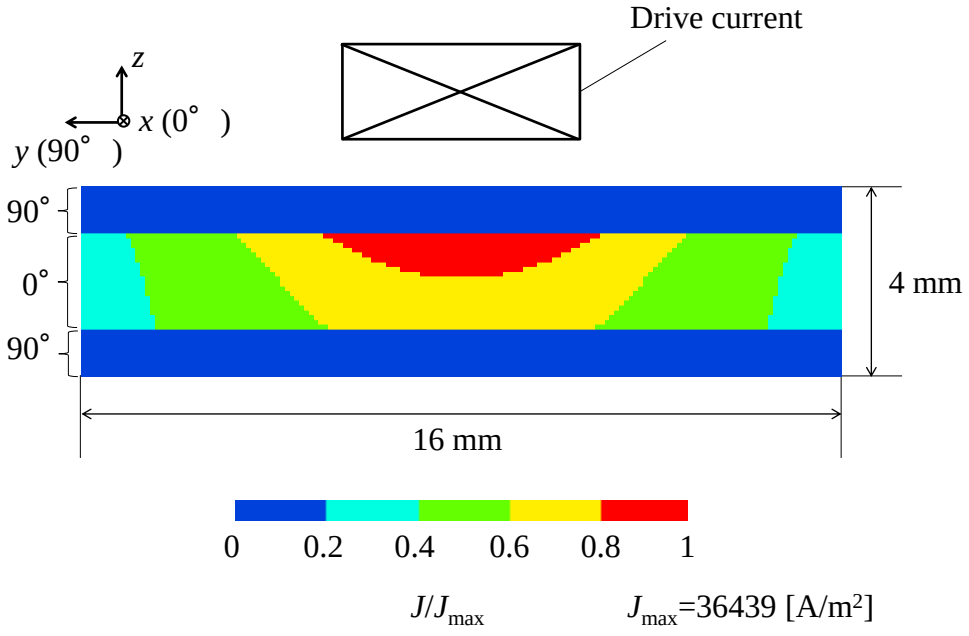

Fig. 2.7 Distribution of eddy current in the *x* direction when a line drive current is placed above cross-ply CFRP with the stacking sequence of [90/0/90].

2.3 Skin depth calculated from an analytical solution and general expression

2.3.1 General expression of skin depth

Eddy current in a conductive material has maximum amplitude at the surface and attenuates in the thickness direction because of the skin effect. The depth at which the amplitude of the eddy current attenuates to 1/*e* (~37%) of the maximum value is referred to as the skin depth of the eddy current. The skin depth is approximately calculated by solving Maxwell's equations assuming that the electric field and magnetic field have only one directional component in a semi-infinite plate. The skin depth δ calculated on the basis of this assumption is expressed as Eq. (2.65).

$$\delta = 1/\sqrt{\pi f \mu \sigma} \tag{2.65}$$

Here, f is the drive frequency and μ and σ are the magnetic permeability and electrical conductivity of the material, respectively. In this approximation, the amplitude of eddy current density $|J|$ at depth z is expressed by Eq. (2.66).

$$|J|/|J_{\max}| = \exp(-z/\delta) \tag{2.66}$$

Here, $|J_{\max}|$ is the maximum eddy current density at the surface of the material. Eq. (2.65) is the well-known general expression of skin depth and widely used to estimate the skin depth of eddy current. It was proved by Todoroki that when the direction of the electric field is the fiber direction or the transverse direction of unidirectional CFRP, conductivity in the electric field direction can be substituted into σ in Eq. (2.65) [2.5]. However, when eddy currents are induced by a line current, the assumption that the electric field and magnetic field have only one directional component may not be realistic. There may thus be a large difference between the skin depth calculated from the general expression in Eq. (2.65) and that calculated from the analytical solution in

the previous chapter. We compare the skin depths calculated from both calculation methods and investigate the difference between them.

2.3.2 Effect of drive current width on skin depth

We investigate the change in skin depth of eddy current in a woven CFRP with the width w of the drive current (see Fig. 2.2). The skin depth calculated from the analytical solution is compared with that calculated from the general expression. Table 2.2 gives the input parameters for calculating the eddy current distribution from the analytical solution. The eddy current distribution is calculated for cases of w = 2, 10, 20 mm. Fig. 2.8 shows the eddy current density along the z direction at $y = y_0$ in Fig. 2.2 calculated from the analytical solution and that calculated from Eq. (2.66). In Fig. 2.8, the horizontal axis denotes the depth from the surface of CFRP and the vertical axis denotes the eddy current density divided by its maximum value. Table 2.3 gives the skin depth in cases of w = 2, 10, 20 mm and the skin depth calculated from the general expression. It is seen that the skin depth increases as the width w of the drive current increases and the eddy current distributes in a deeper region. In addition, the skin depth approaches that calculated from the general expression as w increases. That is because an increase

Table 2.2 Input parameters used in the analysis of the effect of width w

Variables	Value
Width of the drive current: w [mm]	2, 10, 20
Height of the drive current: h [mm]	2
Lift-off: l_1 [mm]	2
Thickness of the CFRP: c [mm]	20
Drive current amplitude: I [A]	1
Drive frequency: f [Hz]	1000000
In-plane conductivity of CFRP: σ_{xy} [S/m]	7700 [2.8]

in w makes magnetic field being directed in almost one direction around $y = y_0$ and this is similar to the assumption used in the derivation of the general expression.

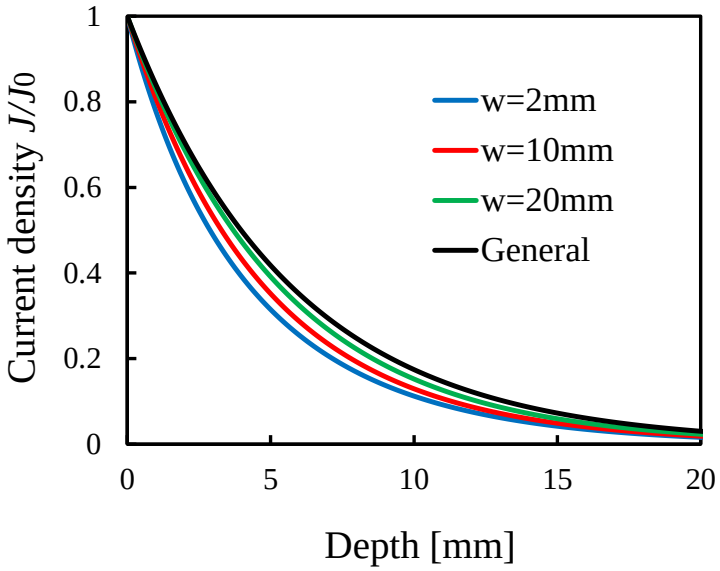

Fig. 2.8 Change in eddy current density at $y = y_0$ with width w of the drive current.

Table 2.3 Changes in skin depth with width w of the drive current and skin depth calculated from the general expression

Calculation condition	Skin depth [mm]
w = 2mm	4.2
w = 10mm	4.7
w = 20mm	5.3
General expression	5.7

2.3.3 Effect of drive current lift-off on skin depth

Changes in skin depth as a result of variation in the lift-off l_1 of the line current are investigated and compared with the skin depth calculated from the general expression. Table 2.4 shows input parameters for calculating the eddy current distribution from the analytical solution. The eddy current distribution is calculated for cases of l_1 = 0.2, 2,

3.8 mm. Fig. 2.9 shows the eddy current distribution in the z direction at $x = x_0$ calculated from the analytical solution and the general expression. In Fig. 2.9, the horizontal axis denotes the depth from the surface of the CFRP and the vertical axis denotes the eddy current density divided by its maximum value. Table 2.5 gives skin depth calculated from the analytical solution for l_1 = 0.2, 2, 3.8 mm and that calculated from the general expression. It is seen that the skin depth increases as lift-off increases. In particular, when l_1 = 0.2 mm, the skin depth calculated from the general expression is

Table 2.4 Input parameters used for the analysis of the effect of lift-off l_1

Variables	Value
Width of the drive current: w [mm]	2
Height of the drive current: h [mm]	2
Lift-off: l_1 [mm]	0.2, 2, 3.8
Thickness of the CFRP: c [mm]	20
Drive current amplitude: I [A]	1
Drive frequency: f [Hz]	1000000
In-plane conductivity of CFRP: σ_{xy} [S/m]	7700 [2.8]

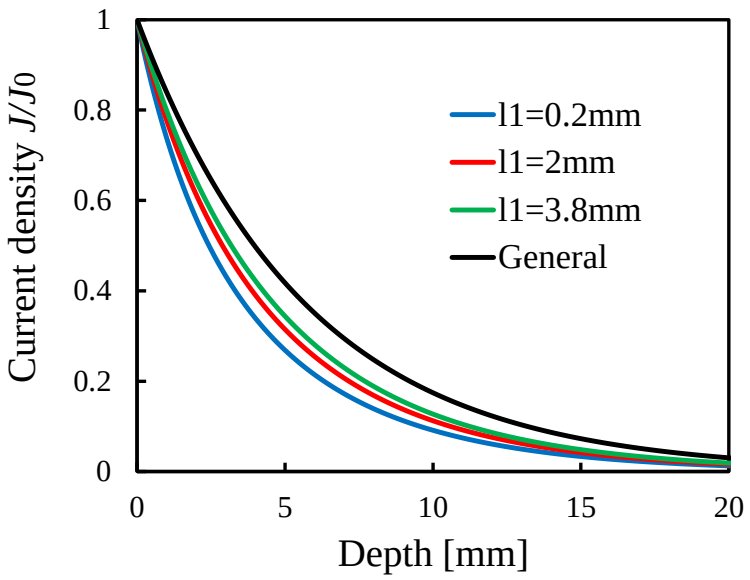

Fig. 2.9 Change in eddy current density at $y = y_0$ with lift-off l_1 of the drive current.

about 160% of the actual skin depth. This result indicates that the general expression overestimates the skin depth of the eddy current when the drive current is placed in the vicinity of the CFRP.

Table 2.5 Changes in skin depth with lift-off l_1 of the drive current and skin depth calculated from the general expression

Calculation condition	Skin depth [mm]
l_1 = 0.2mm	3.6
l_1 = 2mm	4.2
l_1 = 3.8mm	4.6
General expression	5.7

2.4 Conclusions of Chapter 2

In this chapter, we derived analytical solutions for the vector potential in the case that eddy current is induced in CFRP by a line drive current. It was shown that when the line drive current is directed in the fiber direction or transverse direction of unidirectional CFRP, the spatial distribution of the vector potential depends only on the CFRP's conductivity in the drive current direction. Thus, the eddy current distribution is also determined only by conductivity in the drive current direction and is independent of conductivity in other directions. This trend also applies to cross-ply CFRP laminates. Eddy currents are concentrated in layers with a fiber orientation corresponding to the drive current direction. This indicates that layers in which eddy currents are induced can be selected by changing the in-plane azimuth of the line drive current.

The skin depth of eddy current calculated from the derived analytical solution was compared with that calculated from the well-known general expression of the skin depth. Because the general expression is based on the assumption that both the electric field and magnetic field have only one directional component, large error may arise when the general expression is used to estimate the skin depth. We calculated the skin depth from the analytical solution varying the width and the lift-off of the line current and compared with the skin depth calculated from the general expression. It was found that the general expression overestimates the skin depth. The smaller the width and the lift-off of the line current are, the larger the error arising from the general expression becomes. Although the skin depth depends only on the drive frequency and material properties according to the general expression, analytical results indicate that the skin depth strongly depends also on the dimensions and location of the drive current. These findings are important especially to eddy current testing. To achieve higher spatial

resolution in eddy current testing, it is better to limit eddy currents to a narrow region, which indicates that drive current with smaller width is desirable. Moreover, to obtain a higher signal-to-noise ratio in eddy current testing, it is necessary to induce more eddy current in the tested material. Hence, it is better to use a drive current with smaller lift-off. Therefore, the skin depth calculated from the general expression can have large error in eddy current testing.

2.5 References

[2.1] C. V. Dodd and W. E. Deeds, “Analytical solutions to eddy-current probe-coil problems”, Journal of applied physics vol. 39, (1968), pp. 2829-2838.

[2.2] J. W. Luquire, W. E. Deeds and C. V. Dodd, “Alternating Current Distribution Between Planar Conductor”, Journal of Applied Physics, Vol. 41, (1970), pp. 3983-3991.

[2.3] J.C. Abry, S. Bochard, A. Chateauminois, M. Salvia, G. Giraud, “In situ detection of damage in CFRP laminates by electrical resistance measurements”, Composites Science and Technology, Vol. 59, (1999), pp. 925-935.

[2.4] R. Rudolf, P. Mitschang and M. Neitzel, “Induction heating of continuous carbon fibre reinforced thermoplastics”, Composites: Part A, Vol. 31, (2000), pp. 1191–1202.

[2.5] Akira Todoroki, “Skin effect of alternating electric current on laminated CFRP”, Advanced Composite Materials, Vol. 21, No. 5-6, (2012), pp.477-489.

[2.6] T. A. Ezquerra, M. T Connor, S Roy, M Kulescza, J Fernandes-Nascimento, F. J Baltá-Calleja, “Alternating-current electrical properties of graphite, carbon-black and carbon-fiber polymeric composites”, Composites Science and Technology, Vol. 61, (2001), pp. 903-909.

[2.7] S. B. Pratap and W. F. Weldon, “Eddy Currents in Anisotropic Composites Applied to Pulsed Machinery”, IEEE Transactions on Magnetics, Vol. 32, No. 2, (1996).

[2.8] Kiyoshi Koyama, Hiroshi Hoshikawa and Gouki Kojima, “Eddy Current Nondestructive Testing for Carbon Fiber-Reinforced Composites”, Journal of Pressure Vessel Technology, Vol. 135, (2013), pp. 041501-1-5.

Chapter 3

Layer-selectable eddy current technique for detection of in-plane waviness

3.1 Background

This chapter presents a new eddy current method to detect in-plane waviness. Since in-plane waviness is a small deformation of carbon fibers, it is conventionally difficult to obtain the distinct change in the output signal of an eddy current probe. There is thus the need to develop an eddy current method that has high sensitivity to in-plane waviness. In an effort to achieve high sensitivity to in-plane waviness, high-frequency eddy current methods have been studied [3.1]–[3.2] because a higher drive frequency offers better spatial resolution and a larger signal change at defective zone. Heuer et al. successfully detected large in-plane waviness of a fiber roving in woven CFRP using a half-transmission probe at high frequencies up to 100 MHz [3.1]. Although excellent sensitivity can be achieved using high-frequency eddy current methods, a problem arises when inspecting thicker CFRPs. Because of the skin effect, the penetration depth of eddy current becomes smaller at higher frequency [3.3]. This indicates that high-frequency eddy current methods have limitation in detection of waviness in a deeper region. An eddy current probe that is sensitive to in-plane waviness even at lower drive frequency is thus required. In addition to the probe sensitivity, the identification of the wavy fiber orientation is important in the detection of in-plane waviness. It has been reported that fiber waviness causes degradation of mechanical properties in the fiber direction with the waviness [3.4]. It is therefore necessary to develop an eddy current method that identifies the fiber orientation with waviness. Considering the requirements described above, we newly developed an eddy current method that can detect deep lying in-plane waviness and identify the wavy fiber orientation.

3.2 Eddy current method specialized for in-plane waviness detection

3.2.1 Identification of wavy fiber orientation

Fig. 3.1 shows the proposed probe used for in-plane waviness detection. The probe is composed of a vertical rectangular driver coil and rectangular pickup coil perpendicular to each other. The pickup coil is placed under the driver coil such that total excitation magnetic fluxes penetrating the pickup coil loop become zero. Hence, the excitation magnetic field from the driver coil ideally does not contribute to the output voltage of the pickup coil.

The eddy current distribution in cross-ply laminates can be controlled by changing the in-plane azimuth of the probe. When the long sides of the vertical rectangular driver coil parallel to the CFRP surface are directed in a certain fiber direction, eddy currents are concentrated in layers with that fiber direction. For example, when the driver coil is directed in the 0° fiber direction of a cross-ply laminate, eddy currents are concentrated in 0° layers, and thus only 0° layers can be inspected. This can be explained by

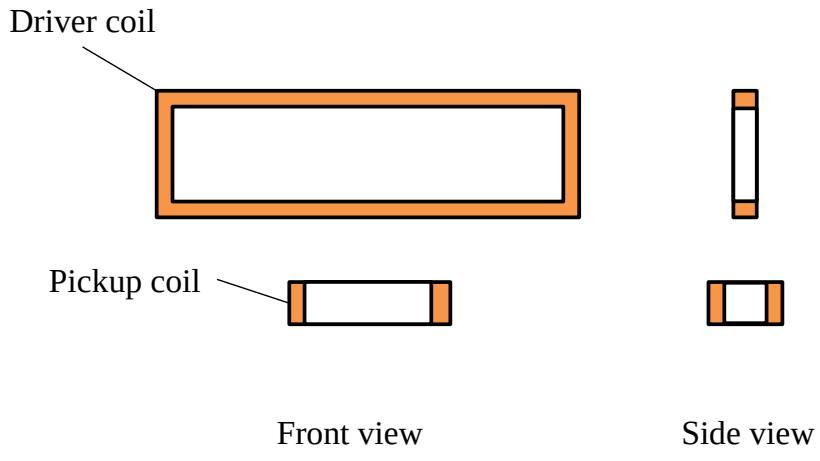

Fig. 3.1 Configurations of the proposed probe. Rectangular driver and pickup coils perpendicular to each other are placed such that the total magnetic flux from the driver coil thorough the pickup coil becomes zero.

analytical solutions to the drive current-eddy current problem. Fig. 3.2 shows the analytical model used for the derivation of the analytical solutions. Two opposing line currents are placed above *n*-layer CFRP laminate. It is assumed that the drive currents have infinite length in the *x* direction of Fig. 3.2. The CFRP plate is assumed to be infinitely long in the *x*-*y* plane. The two drive currents in the rectangular driver coil parallel to the CFRP surface can be approximately simulated by two infinite line currents if the sides of the rectangular driver coil parallel to the CFRP surface are sufficiently long. As described in Chapter 2, the differential equation of the magnetic vector potential in the laminate in Fig. 3.2 is written as follows.

$$\nabla^2 \boldsymbol{A} = -\mu_0 \boldsymbol{i_0} + j\omega\mu_0 \begin{pmatrix} \sigma_0 \cos^2\theta + \sigma_{90}\sin^2\theta & \dfrac{\sigma_0 - \sigma_{90}}{2}\sin 2\theta & 0 \\ \dfrac{\sigma_0 - \sigma_{90}}{2}\sin 2\theta & \sigma_0 \sin^2\theta + \sigma_{90}\cos^2\theta & 0 \\ 0 & 0 & \sigma_t \end{pmatrix} \boldsymbol{A} \tag{3.1}$$

Here, $\boldsymbol{A}$ is the vector potential, μ_0 is the magnetic permeability in a vacuum, $\boldsymbol{i_0}$ is the drive current density vector, ω is the angular drive frequency and j is the imaginary unit.

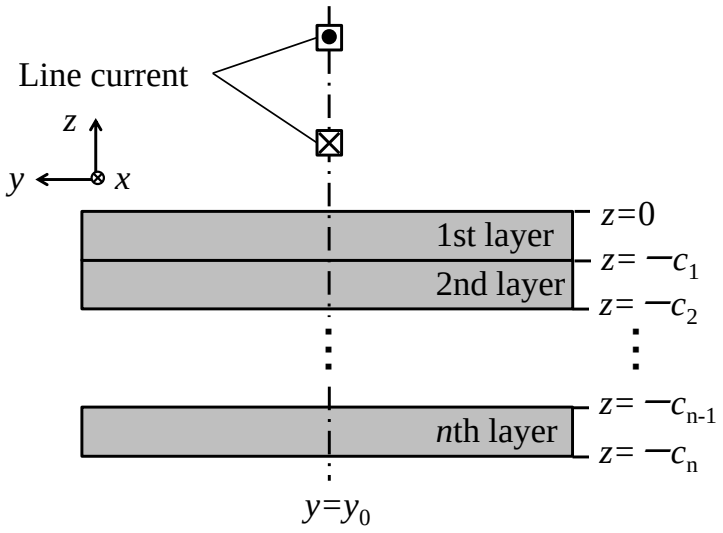

Fig. 3.2 Analytical model of line drive currents above a cross-ply CFRP laminate. Two line currents infinitely long in the *x* direction are placed above the *n*-layer CFRP laminate. The two line currents flow in opposite directions.

σ_0, σ_{90} and σ_t are the electrical conductivities of the unidirectional ply in longitudinal, transverse and thickness directions, respectively. θ denotes the fiber orientation angle of a layer in the CFRP (where the x axis in Fig. 3.2 is assumed to be the 0° direction). When θ = 0° or 90°, (1,2) and (2,1) components in the conductivity matrix of Eq. (3.1) become zero. Hence, Eq. (3.1) is not a simultaneous differential equation and can be solved by the separation of variables as mentioned in Chapter 2. Analytical solutions for x, y and z directional components of the vector potential in the k^{th} layer of the CFRP are expressed as follows.

$$A_x = \int_0^\infty (A_k e^{(\alpha^2 + j\omega\mu\sigma_k)^{1/2} z} + B_k e^{-(\alpha^2 + j\omega\mu\sigma_k)^{1/2} z}) \cos\alpha(y - y_0) d\alpha \quad (k = 1, 2, \ldots, n) \tag{3.2}$$

$$A_y = 0 \tag{3.3}$$

$$A_z = 0 \tag{3.4}$$

In Eq. (3.2), A_k and B_k are constants determined by boundary conditions. σ_k is the conductivity in the drive current direction. Eqs. (3.2)–(3.4) show that the vector potential has only one directional component (i.e., the x directional component in the case of Fig. 3.2) and is directed in the drive current direction when the laminate is a cross-ply laminate. Moreover, the vector potential depends only on conductivity in the drive current direction. Electrical conductivities in directions perpendicular to the drive current does not affect the vector potential. The eddy current density vector can be calculated using the vector potential and is expressed as Eq. (3.5).

$$\boldsymbol{J} = -j\omega \begin{pmatrix} \sigma_0 \cos^2\theta + \sigma_{90} \sin^2\theta & \dfrac{\sigma_0 - \sigma_{90}}{2} \sin 2\theta & 0 \\ \dfrac{\sigma_0 - \sigma_{90}}{2} \sin 2\theta & \sigma_0 \sin^2\theta + \sigma_{90} \cos^2\theta & 0 \\ 0 & 0 & \sigma_t \end{pmatrix} \boldsymbol{A} \tag{3.5}$$

Eq. (3.5) indicates that eddy currents flow only in the drive current direction. Since

electrical conductivity in the fiber direction is approximately 1,000 times larger than that in transverse direction, it is implied that eddy currents are concentrated in layers with a fiber direction corresponding to the drive current direction.

To verify the nature of eddy current in the cross-ply laminate described above, the eddy current distribution is calculated in FEM analyses. The FEM analyses are performed using the general-purpose FEM software ANSYS. An analytical model of the FEM analysis is shown in Fig. 3.3. A rectangular driver coil is placed above a CFRP laminate with a lift-off of 4 mm. The dimensions of the CFRP plate are 100 mm × 100 mm × 4 mm, and it is assumed that the stacking sequence is $[0_2/90_2/0_2/90_2]_s$. *x* and *y* directions in the model represent 0° and 90° fiber directions, respectively. Electrical conductivities of the unidirectional ply used in this analysis are given in Table 3.1 [3.5]. The length of the long side of the driver coil parallel to the CFRP surface is denoted *d* and the length of the short side perpendicular to the CFRP surface is 5 mm. Long sides

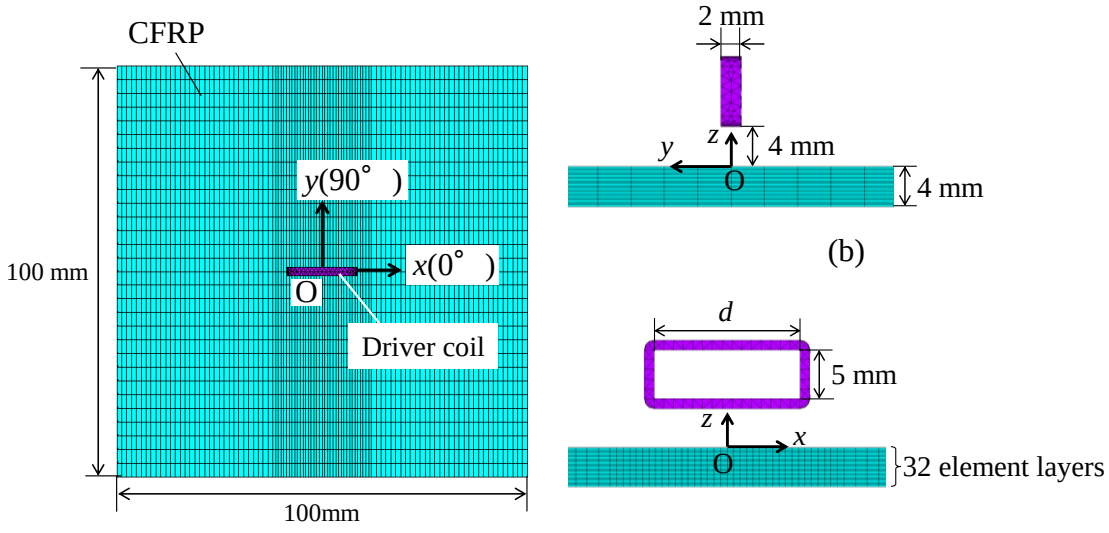

Fig. 3.3 Analytical model of the vertical rectangular driver coil placed above a CFRP cross-ply laminate: (a) top view, (b) side view, (c) front view.

of the rectangular driver coil parallel to the CFRP surface are directed in the 0° direction of the cross-ply laminate. The driver coil is located at the center of the CFRP plate. The frequency of the drive current is set to 1 MHz. The CFRP laminate has 32 element layers in the thickness direction. Fig. 3.4 shows the eddy current vector distribution under the driver coil calculated in FEM analysis. The location of the driver coil is $x = y = 0$. The length of the long side of the driver coil, d, is assumed to be 15 mm in Fig. 3.4. Distributions of the real part of the eddy current density vector in each element layer are displayed in Fig. 3.4. The displayed area is a 50 mm × 50 mm area under the driver coil. The real part denotes the component that is in-phase with the drive current. As shown in Fig. 3.4, eddy currents are concentrated only in 0° layers immediately under the driver coil, and are directed in the 0° direction as implied by Eq. (3.5). Eddy currents flowing in the 90° direction away from $x = y = 0$ are results of the finite length of line drive currents. The eddy current distribution in the thickness direction is investigated while varying the length of long side d. Fig. 3.5 shows the FEM results of the eddy current density distribution in the thickness direction at $x = y = 0$ for d = 15, 30, 45 mm and $d \rightarrow \infty$. In Fig. 3.5, the horizontal axis denotes the distance from the surface, while the vertical axis denotes the amplitude of the eddy current density in the 0° direction. The case of $d \rightarrow \infty$ is calculated using the two-dimensional model shown in Fig. 3.2. As seen in Fig. 3.5, eddy currents are concentrated in 0° layers, while the amplitudes of eddy

Table 3.1 Material properties of unidirectional ply used for FEM analysis [3.5]

Material property	Value
Conductivity in fiber direction [S/m]	34120
Conductivity in transverse direction [S/m]	24
Conductivity in thickness direction [S/m]	20
Magnetic permeability [H/m]	1.26×10^{-6}

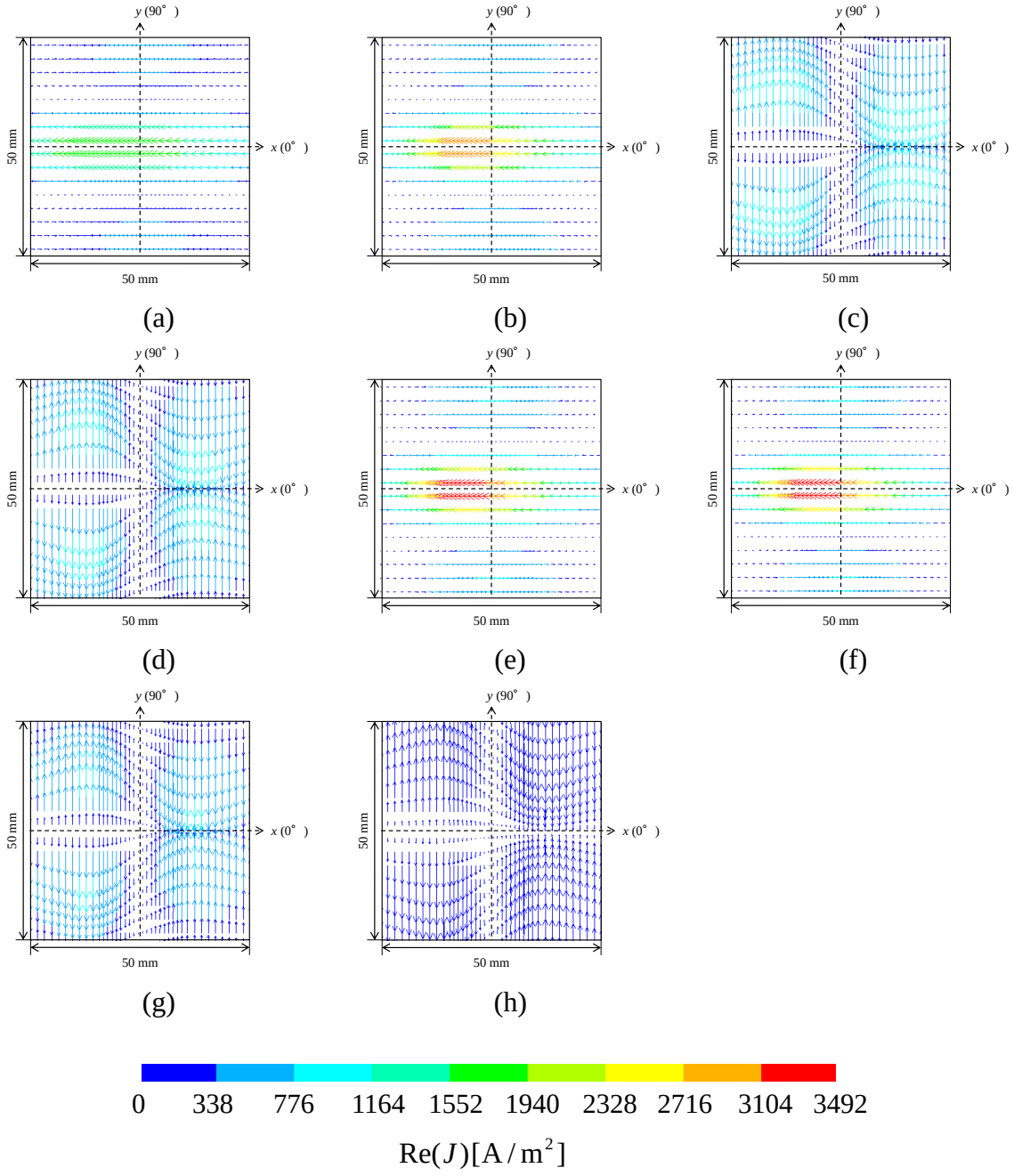

Fig. 3.4 Eddy current vector distribution in $[0_2/90_2/0_2/90_2]_s$ laminate calculated using FEM, where the real part of the eddy current density vector in the 50 mm × 50 mm area under the driver coil is displayed: (a) first element layer from the surface (0° layer), (b) fourth element layer (0° layer), (c) fifth element layer (90° layer), (d) eighth element layer (90° layer), (e) ninth element layer (0° layer), (f) 12th element layer (0° layer), (g) 13th element layer (90° layer), (h) 16th element layer (90° layer).

currents in the 90° layers are small. As the length of the long sides of the driver coil increases, the eddy current distribution approaches that of two-dimensional analysis. Fig. 3.5 shows that the eddy current density is not a maximum at the surface in the cases of *d* = 15, 30, 45 mm. This is because of the strong anisotropy in electric conductivity of the CFRP. A case in which the eddy current density was not a maximum at the surface in the ET of a cross-ply CFRP has been reported [3.6].

If infinitely long line drive currents in Fig. 3.2 are directed in one of the fiber directions of the cross-ply CFRP, the term of electric potential can be eliminated from the governing equation of the electromagnetic field, as shown in Eq. (3.1). However, since the rectangular driver coil has finite length, there is an electric potential gradient. Fig. 3.6 shows the numerically calculated distributions of the electric potential in the cross-ply CFRP at different depths. The electric potential distribution was calculated using the analytical model in Fig. 3.3, which was used to obtain the eddy current distributions shown in Fig. 3.4. Fig. 3.6 shows that there is an electric potential gradient in the laminate. This gradient is caused by the accumulation of electric charge

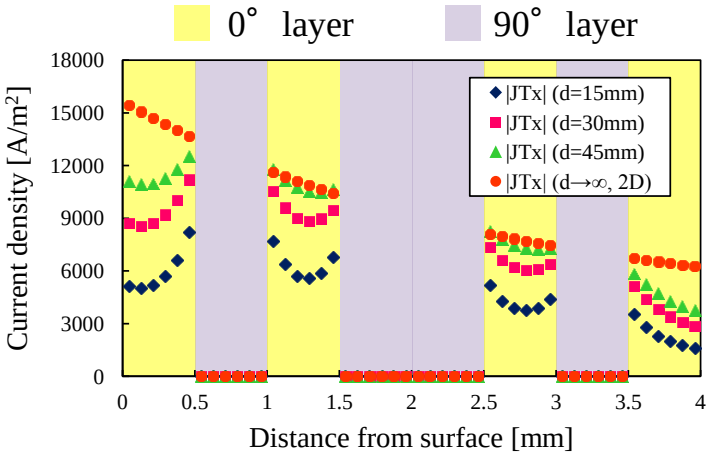

Fig. 3.5 Numerical results of the eddy current density distribution in the thickness direction under a driver coil.

originating from the finite length of the drive current. Hoshikawa and Koyama reported that when a vertical rectangular coil is excited above a conductive plate, electric charge

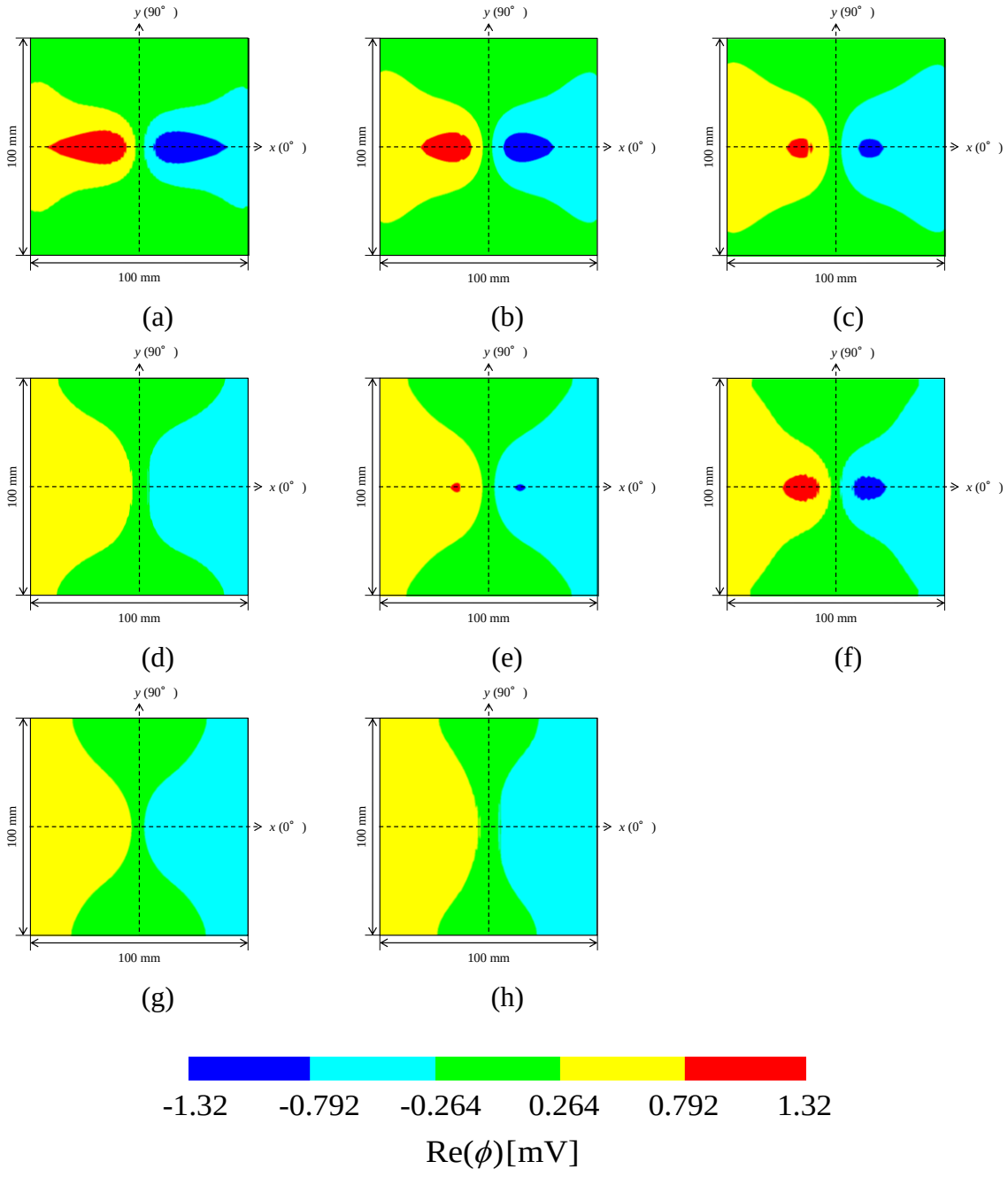

Fig. 3.6 Distribution of the real part of the electric potential in a 100 mm × 100 mm area under the driver coil calculated using FEM: (a) z = 0 mm, (b) z = −0.25 mm, (c) z = −0.5 mm, (d) z = −0.75 mm, (e) z = −1 mm, (f) z = −1.25 mm, (g) z = −1.5 mm, (h) z = −1.75 mm.

is carried in the direction of the sides of the rectangular driver coil parallel to the plate surface [3.7]. This produces an area with increased electric charge and an area with decreased electric charge under the driver coil. This explains the electric potential gradient in Fig. 3.6. The potential gradient is not produced in the case of excitation with an infinitely long line drive current. This is because the infinite length of the line drive current does not cause localization of electric charge. Because of the generation of the electric potential gradient, the eddy current distribution depends on electrical conductivity in the transverse and thickness directions. Fig. 3.7 shows the numerically calculated relationship between the maximum eddy current density (J_{max}) in the cross-ply laminate and electrical conductivities in transverse and thickness directions. It is seen that J_{max} strongly depends on electrical conductivity in the thickness direction, while the effect of the variation of electrical conductivity in transverse direction is much weaker. According to the analytical solution shown in Eq. (3.2), electrical conductivities in transverse and thickness directions do not affect the eddy current distribution. This is

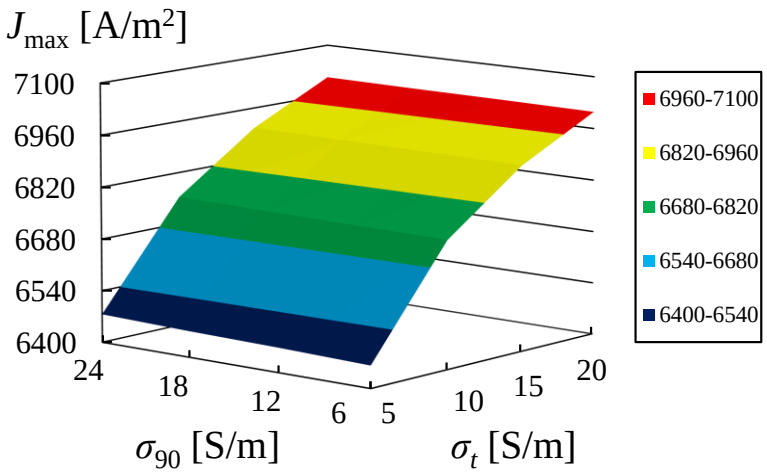

Fig. 3.7 Numerically calculated relationships between the maximum eddy current density in the cross-ply laminate $[0_2/90_2/0_2/90_2]_s$ and electrical conductivities in transverse and thickness directions of unidirectional ply.

because there is no electric potential gradient in the case of the infinitely long line drive current. Meanwhile, variation of electrical conductivity in the thickness direction strongly affects the magnitude of eddy current if the eddy current is induced by a vertical rectangular driver coil, as shown in Fig. 3.7. Since electrical conductivity in the thickness direction depends on the contacts of carbon fibers, there is a large variation of this property in the CFRP laminate [3.8]. It is noted that the variation of electrical conductivity in the thickness direction may cause the variation of output signal of the probe during scanning.

As shown by the results of FEM analyses described above, eddy currents in cross-ply CFRP are directed in the direction of the long sides of the driver coil parallel to the CFRP surface. Furthermore, the eddy currents are concentrated in the layers with a fiber direction corresponding to the long sides. Therefore, the inspected fiber direction can be selected by changing the in-plane azimuth of the probe, and the fiber direction with waviness can be identified.

3.2.2 Sensitivity to in-plane waviness

In addition to the selectability of the inspected fiber direction, the probe has high sensitivity to in-plane fiber waviness. The magnetic field from the driver coil does not contribute to the output voltage of the pickup coil because total excitation magnetic fluxes penetrating the pickup coil loop upwardly and downwardly are equal to each other. Fig. 3.8 shows schematic illustrations of the eddy current path in the non-defective zone and in-plane waviness zone. Eddy currents under the driver coil are parallel to the long sides of the driver coil in non-defective zones, as shown by the FEM results in Fig. 3.4. Total magnetic fluxes from eddy currents through the pickup coil

loop become zero at non-defective zones. Hence, the output voltage of the probe is ideally zero at non-defective zones. On the other hand, when the probe is close to the waviness, the output voltage of the pickup coil is generated by changes in the eddy current path along the waviness. As shown in Fig. 3.8, the eddy current path is deformed in the waviness zone because eddy current flows along carbon fibers. In this case, the magnetic field from the eddy current penetrating the pickup coil loop upwardly and that from the eddy current penetrating the pickup coil loop downwardly are not equal. An output voltage of the pickup coil is thus produced. This indicates that a large change ratio in the pickup coil voltage is caused by waviness. The probe shown in Fig. 3.1 thus has high sensitivity to in-plane waviness. Furthermore, since the output voltage of the pickup coil is zero at non-defective zones, the probe is insensitive to lift-off variations.

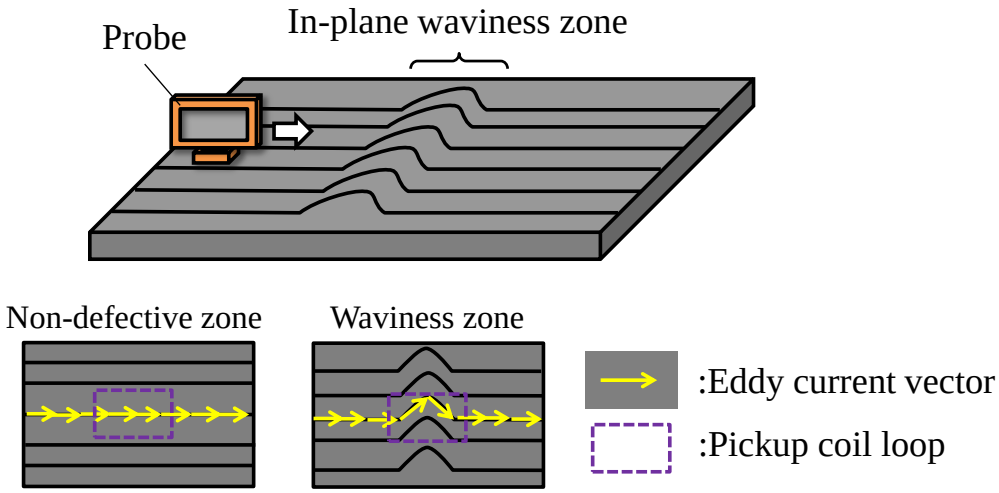

Fig. 3.8 Schematic illustrations of the eddy current path under the proposed probe.

3.3 Experiments on waviness detection for cross-ply laminates

3.3.1 Materials

Fig. 3.9 shows cross-ply CFRP specimens with artificial in-plane waviness.

Specimen #1 shown in Fig. 3.9(a) was a three-layer cross-ply laminate with a

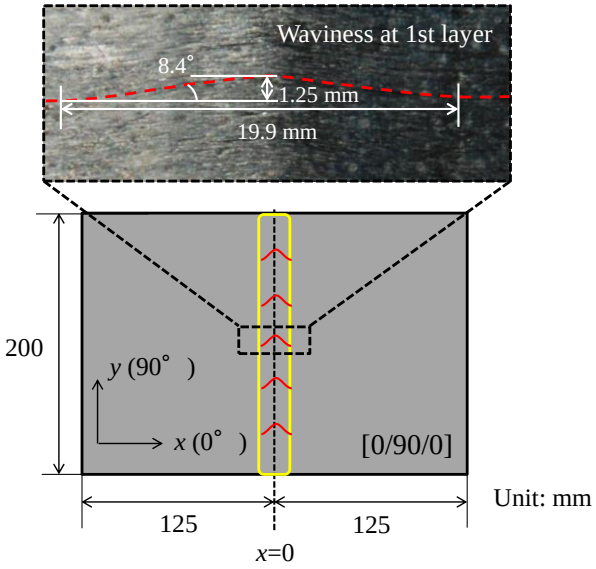

(a)

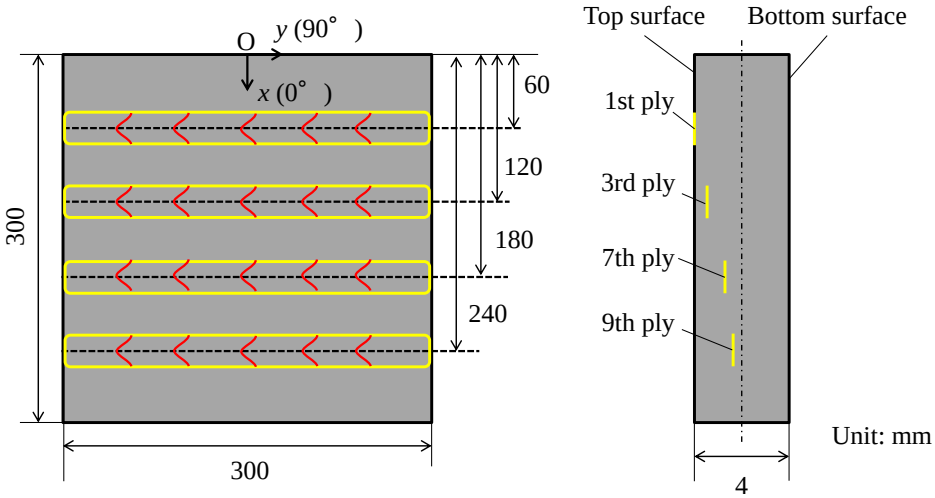

(b)

Fig. 3.9 Cross-ply CFRP specimens with artificially induced in-plane waviness: (a) three-layer cross-ply laminate [0/90/0] (specimen #1), (b) 20-layer cross-ply laminate $[(0/90)_5]_s$ (specimen #2).

stacking sequence of [0/90/0]. The length and width of the laminate were 250 and 200 mm, respectively. Specimen #1 was fabricated by stacking unidirectional prepregs (Mitsubishi Rayon Co., Ltd., PYROFIL TR380G250S) and curing them in an electric furnace. In-plane fiber waviness was artificially induced in the first layer along the center line (x = 0) of the specimen. Although actual waviness is not always induced along the part width, the use of a specimen with waviness along the part width is valid because the eddy current is spatially localized under the driver coil as Fig. 3.4 shows. The waviness was induced by deforming fibers in the prepreg before stacking. Epoxy resin on the center line of the first layer prepreg was removed by wiping it with a paper towel soaked with acetone until carbon fibers could deform. Subsequently, compression was applied to the resin-removed area to produce in-plane waviness. The prepreg with in-plane waviness was stacked and cured following the manufacturer's recommended cycle. As shown in Fig. 3.9(a), in-plane waviness in which fibers were deformed in the $+y$ direction was induced. At the center of the first layer of specimen #1, the amplitude and length of the induced waviness were 1.25 and 19.9 mm, respectively. The misalignment angle of the waviness was 8.4° as shown in Fig. 3.9(a).

Specimen #2 was a 20-layer cross-ply laminate with a stacking sequence of $[(0/90)_5]_s$. The dimensions of specimen #2 were 300 mm × 300 mm × 4 mm. Specimen #2 was fabricated by stacking thermoplastic unidirectional prepregs (Toho Tenax Co., Ltd., Q111E 2000). Multiple in-plane waviness were artificially induced in 0° layers, which were the first, third, seventh and ninth layers from the top surface, as shown in Fig. 3.9(b). The waviness were induced by deforming fibers in each prepreg prior to molding. A heat gun was used to heat part of the prepreg until the thermoplastic resin had softened. Carbon fibers in that area were then moved in the transverse direction ($-y$

direction in Fig. 3.9(b)) to induce in-plane waviness. Prepregs with in-plane waviness were stacked and a CFRP specimen with in-plane waviness at desired positions was fabricated. The sizes of the artificial waviness were measured by X-ray CT and from optical images. Fig. 3.10 shows the method to measure the size of waviness from the obtained images. The size of waviness was measured using auxiliary lines. Since in-plane waviness in the first layer was visible, its size was measured from the optical image shown in Fig. 3.10(a). Sizes of subsurface waviness were measured from an X-ray CT image, as shown in Fig. 3.10(b). Table 3.2 gives the sizes of waviness in specimen #2 measured from X-ray CT and an optical image.

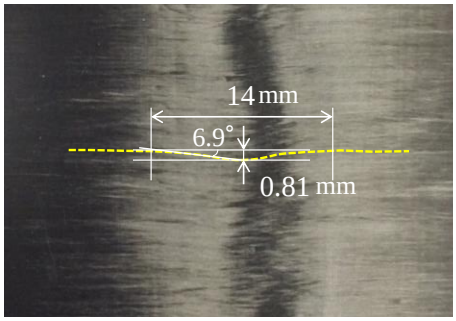

(a)

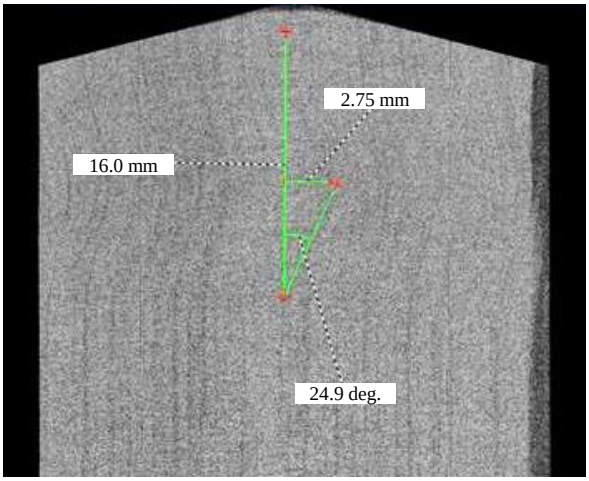

(b)

Fig. 3.10 Examples of the auxiliary-line-based measurement of in-plane waviness: (a) optical image of the first layer waviness in specimen #2, (b) X-ray CT image of the third layer waviness in specimen #2

Table 3.2 Sizes of in-plane waviness in specimen #2 measured from X-ray CT and an optical image (where the size of waviness in the first layer was measured from an optical image)

Layer (from top surface)	Amplitude [mm]	Length [mm]	Angle [°]
first layer	0.81	14.0	6.9
third layer	2.75	16.0	24.9
seventh layer	1.48	10.6	21.8
ninth layer	1.66	10.8	20.6

3.3.2 Experimental setup

Fig. 3.11 shows the experimental setup of the ET of the cross-ply specimens with in-plane waviness. The probe shown in Fig. 3.1 was placed above the CFRP specimen.

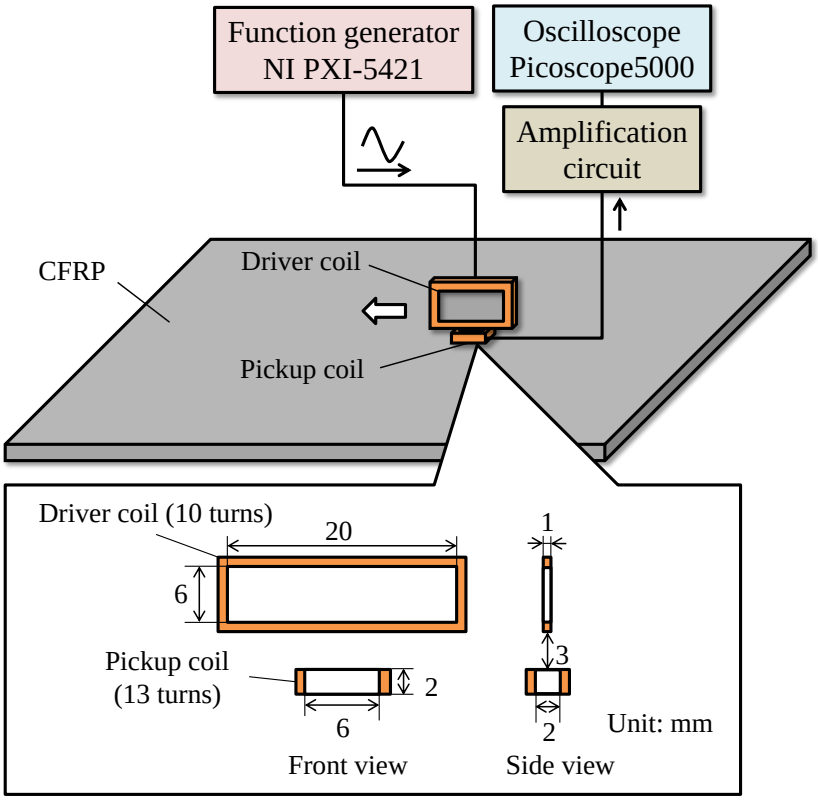

Fig. 3.11 Experimental setup of ET of cross-ply CFRP specimens with in-plane waviness.

The driver coil was a 10-turn rectangular coil, and the long sides and short sides were 20 and 6 mm, respectively. The pickup coil was a rectangular coil with 13 turns and dimensions of 6 mm × 2 mm. The diameters of enameled copper wire used to turn the driver and pickup coils were 0.3 mm and 0.16 mm, respectively. The pickup coil was located 3 mm under the driver coil. The drive voltage was supplied by an arbitrary waveform generator (National Instruments Corporation, NI PXI-5421, 16-bit, 100 MS/s). The output voltage of the pickup coil was amplified by a factor of 100 using an amplification circuit and then measured using an oscilloscope (Pico Technology Ltd., Picoscope 5442 A, 14-bit, 125 MS/s).

For the detection of in-plane waviness in specimen #1, the probe was placed above specimen #1 such that the long side of the driver coil was directed in the 0° fiber direction. The lift-off of the probe (i.e., the distance between the specimen surface and the bottom of the pickup coil) was 3 mm. A sinusoidal voltage with frequency of 3 MHz was applied to the driver coil. The probe scanned along the 0° fiber direction (x direction in Fig. 3.9(a)), and the output voltage of the pickup coil was measured at 2.5 mm intervals. This experiment was performed for the two cases shown in Fig. 3.12. In cases 1 and 2 shown in Figs. 3.12(a) and (b), the relationships between the positive direction of the drive current and the direction of fiber displacement in waviness are different. Experiments were carried out for case 1 and 2 to investigate whether the output voltage of the pickup coil depends on the direction of fiber displacement in waviness.

Three experiments were performed for specimen #2. First, long sides of the driver coil were directed in the 0° fiber direction, and the probe scanned the top surface of specimen #2 along the x axis in Fig. 3.9(b). In this case, in-plane waviness were located

in the first, third, seventh and ninth layers from the inspected surface. Lift-off of the probe was nominally 0.5 mm and the probe scanned along the *x* axis in Fig. 3.9(b) at 2.5 mm intervals. Drive frequencies applied to the driver coil were 1, 3, and 5 MHz. Second, long sides of the driver coil were directed in the 0° fiber direction, and the probe scanned the bottom surface of specimen #2. In this case, in-plane waviness were located in 20^{th}, 18^{th}, 14^{th} and 12^{th} layers from the inspected surface. Drive frequencies used in this case were 0.25, 0.5 and 1 MHz. Other measurement conditions such as the lift-off and measurement interval were the same as those in the top-surface measurement. Third, long sides of the driver coil were directed in the 90° fiber direction (*y* direction in Fig. 3.9(b)), and the probe scanned the top surface along the *x* axis. This case was studied to investigate whether the proposed probe can select layers to be inspected. If the proposed probe can successfully select layers to be inspected, in-plane waviness in 0° layers are not detected when the probe is directed in the 90° direction. Frequencies of sinusoidal

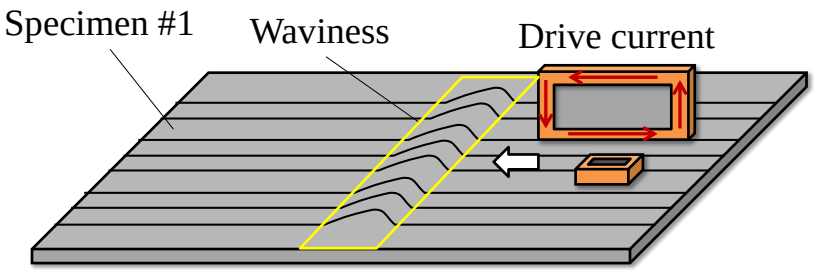

(a)

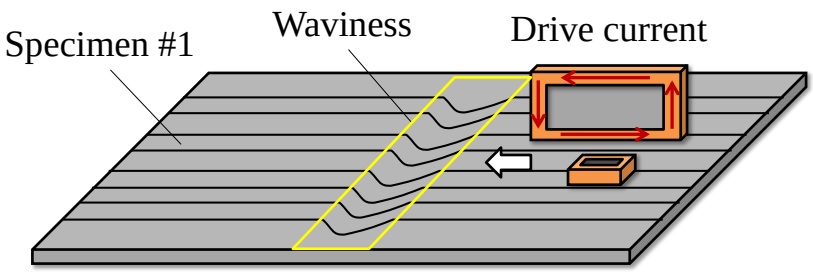

(b)

Fig. 3.12 Relationship between the positive direction of drive current and the direction of fiber deformation in waviness: (a) case 1, (b) case 2.

voltage applied to the driver coil were 0.25, 0.5 and 1 MHz. Other measurement conditions were the same as those in the first and second measurements.

3.3.3 Results and discussion

Fig. 3.13 shows measurement results for specimen #1. The horizontal axis denotes the *x* location of the center of the pickup coil and the vertical axis denotes the amplitude of the pickup coil voltage divided by the amplitude of the drive voltage. Since it is often necessary to evaluate the probe output for arbitrary excitation amplitude, the output signal is normalized by the input signal. The region $-10 < x < 10$ mm in Figs. 3.13(a) and (b) represents the in-plane waviness zone. $x = 0$ is the location of the vertex of the

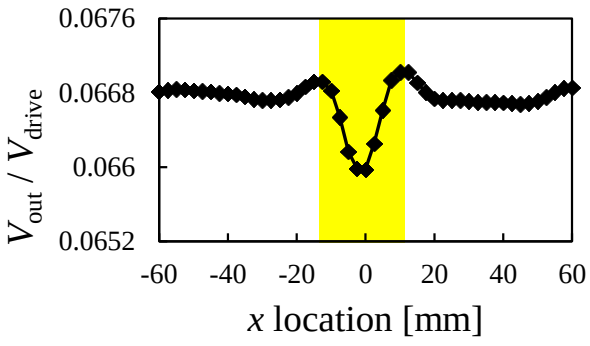

(a)

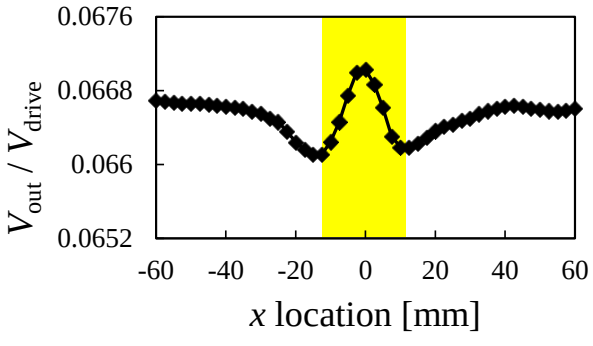

(b)

Fig. 3.13 Results of ET obtained by the probe scanning specimen #1: (a) results for case 1, (b) results for case 2.

waviness. Fig. 3.13(a) shows that in case 1 of Fig. 3.12(a), the amplitude of the pickup coil output has a local maximum at the edges of the waviness zone and has a local minimum value at the vertex of the waviness. This result implies that the length of the in-plane waviness zone can be roughly estimated from the distance between two measurement points where a local maximum output is obtained. Although the output of the pickup coil becomes zero theoretically at the non-defective zone, it is not the case in Fig. 3.13. This is because of dimensional misalignment in coil fabrication. In contrast, Fig. 3.13(b) shows that in case 2 of Fig. 3.12(b), the amplitude of the pickup coil output becomes a local minimum at the edges of the waviness zone and a local maximum at the vertex of the waviness. In this measurement, the distance between two measurement points with a local minimum output represents the length of waviness. The difference between Figs. 3.13(a) and (b) is caused by the direction of fiber displacement in waviness, which implies that the direction of fiber displacement can be identified using the obtained output signals.

Fig. 3.14 shows results of the top-surface measurement of specimen #2 in which long sides of the driver coil were directed in the 0° fiber direction. The horizontal and vertical axes denote the x location of the probe and the amplitude of the pickup coil output divided by the drive voltage amplitude. x = 60, 120, 180 and 240 mm are nominal locations of the vertex of waviness in the first, third, seventh and ninth layers, respectively. Figs. 3.14(a), (b) and (c) show the results for frequencies of 1, 3 and 5 MHz, respectively. As shown in Fig. 3.14(a), the output voltage of the pickup coil becomes a local minimum at all waviness vertexes. Moreover, it is observed that the output voltage becomes a local maximum at the edges of waviness zones like the results shown in Fig. 3.13(a). These results confirm that the waviness length can be

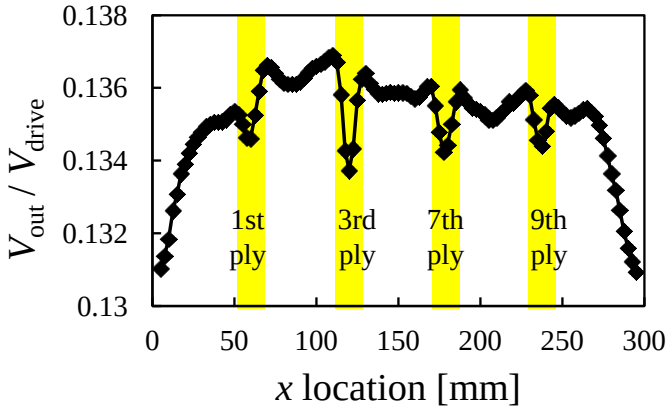

(a)

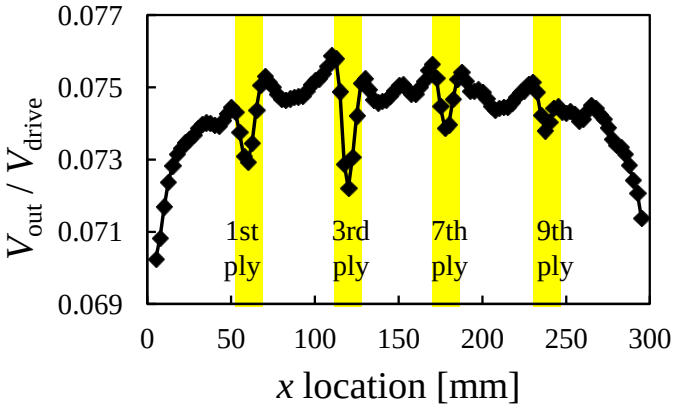

(b)

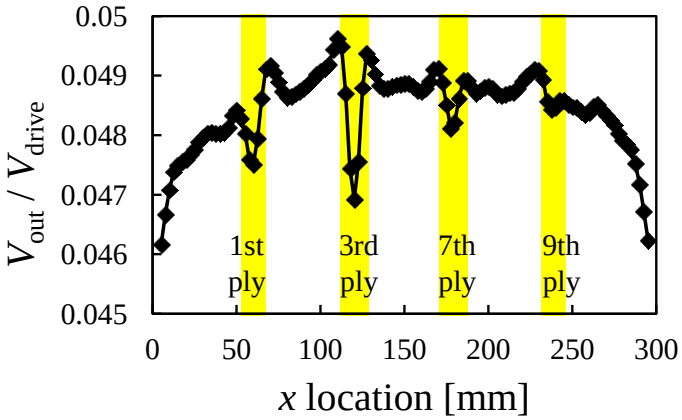

(c)

Fig. 3.14 Results obtained from the top-surface measurement. Long sides of the driver coil are directed in the 0° direction of specimen #2: (a) 1 MHz, (b) 3 MHz, (c) 5 MHz.

roughly estimated from the measurement data. Low values of output voltage around x = 0 and 300 mm are due to the edge effect. A comparison of the results in Figs. 3.14(a)–(c) reveals that the change in the pickup coil output at ninth ply waviness zone becomes smaller as the drive frequency increases. This is because of the well-known skin effect of eddy current. The penetration depth of eddy currents decreases as frequency increases. It thus becomes more difficult to inspect a deeper region at higher frequencies. However, since a higher frequency can offer a higher signal-to-noise ratio of the pickup coil voltage, there is a trade-off relationship between the signal-to-noise ratio and penetration depth.

Fig. 3.15 shows the results of the bottom-surface measurement in which the long sides of the driver coil were directed in the 0° direction. x = 60, 120, 180 and 240 mm are nominal locations of the vertex of waviness in the 20^{th}, 18^{th}, 14^{th} and 12^{th} layers, respectively. Figs. 3.15(a), (b) and (c) show the results for frequencies of 0.25, 0.5 and 1 MHz, respectively. Fig. 3.15(a) shows that the output of the pickup coil becomes a local maximum in the waviness zones of the 18^{th}, 14^{th} and 12^{th} layers, in contrast to the top-surface measurement. This is due to the difference in the direction of fiber displacement in waviness, as shown by the results for specimen #1. The direction of fiber displacement in waviness becomes the opposite when the specimen is turned over. Results in Figs. 3.15(a)–(c) show that recognizable signal changes can be produced by waviness in the 18^{th}, 14^{th} and 12^{th} layers for all frequencies used in the experiment. The change in the pickup coil output obtained at the location of the 18^{th} layer becomes slightly clearer at 0.25 MHz than at higher frequencies. This is again because a larger penetration depth of eddy current is achieved at lower frequency. However, the waviness in the 20^{th} layer cannot be detected in this experiment. At a drive frequency

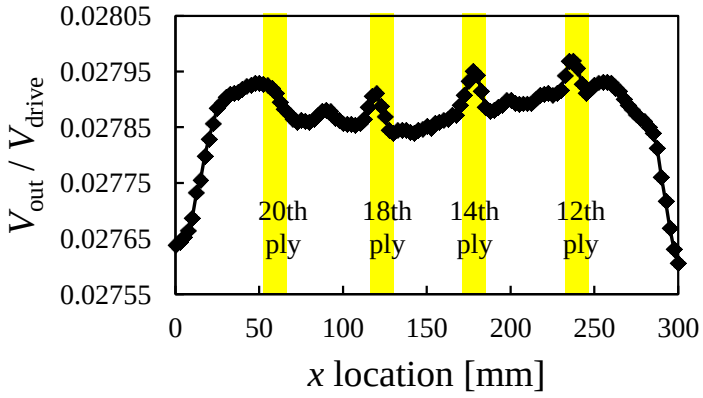

(a)

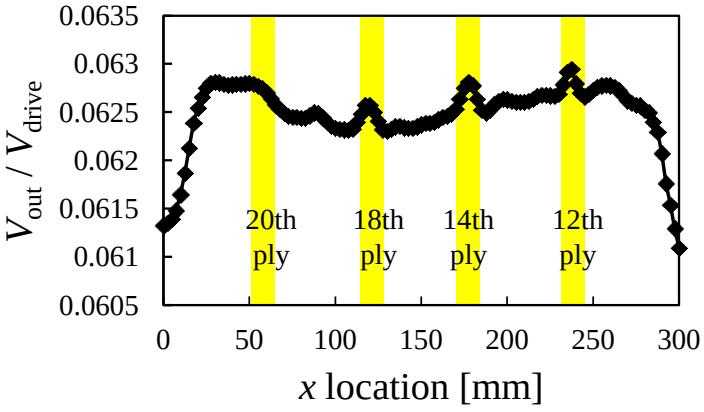

(b)

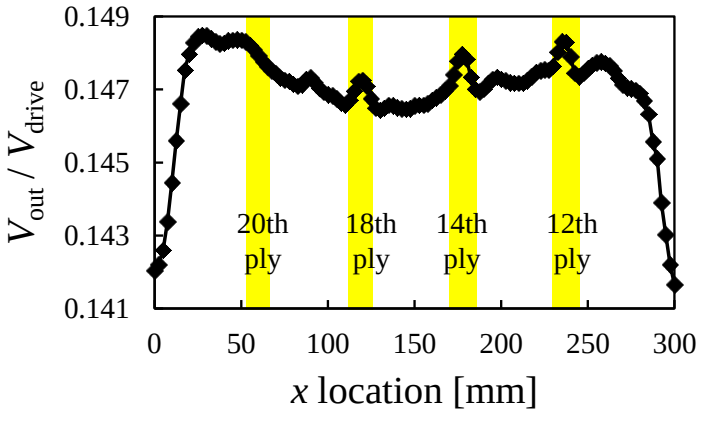

(c)

Fig. 3.15 Results obtained from the bottom-surface measurement, where long sides of the driver coil are directed in the 0° direction of specimen #2: (a) 0.25 MHz, (b) 0.5 MHz, (c) 1 MHz.

lower than 100 kHz, no waviness can be detected because of low signal-to-noise ratio.

Fig. 3.16 shows the results of the top-surface measurement in which the long sides of the driver coil were directed in the 90° direction. x = 60, 120, 180 and 240 mm are nominal locations of the vertex of waviness in the first, third, seventh and ninth layers, respectively. Figs. 3.16(a), (b) and (c) show the results for frequencies of 0.25, 0.5 and 1 MHz, respectively. Fig. 3.16(a) reveals that there is no observable change in the pickup coil output at the locations of the waviness. Almost the same results were obtained at higher frequencies as shown in Figs. 3.16(b) and (c). This is because eddy currents are concentrated only in 90° layers when the long sides of the driver coil are directed in the 90° direction, as described in FEM analysis. In this case, amplitudes of eddy current in 0° layers are small, and thus no waviness in 0° layers can be detected. Therefore, the proposed probe can select layers to be inspected and identify the fiber direction with in-plane waviness.

To investigate the physical background of the pickup coil output obtained in Figs. 3.13, 3.14, 3.15 and 3.16, FEM analyses were performed using the general-purpose FEM analysis software ANSYS.

First, the magnetic field distribution under the driver coil is calculated assuming that in-plane waviness is induced in the 0° layer in a cross-ply laminate and that the long sides of the rectangular driver coil are directed in the 0° fiber direction. Fig. 3.17 shows the analytical model for the calculation of the magnetic field under the driver coil. A rectangular driver coil is placed above a CFRP plate with a lift-off of 4 mm. The CFRP plate is a cross-ply laminate with a stacking sequence of $[0_2/90_2/0_2/90_2]_s$ and dimensions of 100 mm × 100 mm × 4 mm. The origin of the Cartesian coordinates (x, y, z) is set at the center of the surface of the CFRP plate, as shown in Fig. 3.17. The x and y directions

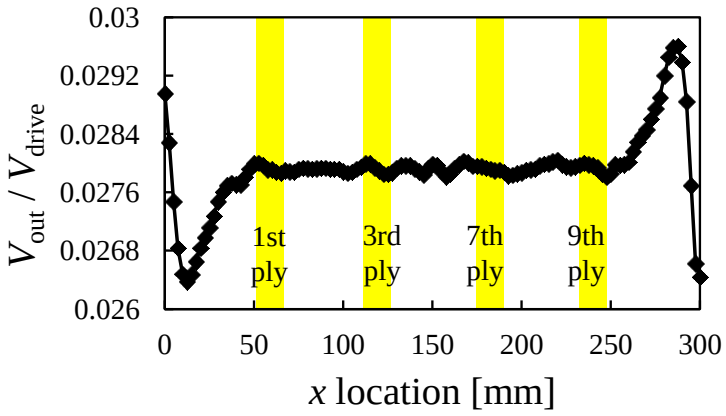

(a)

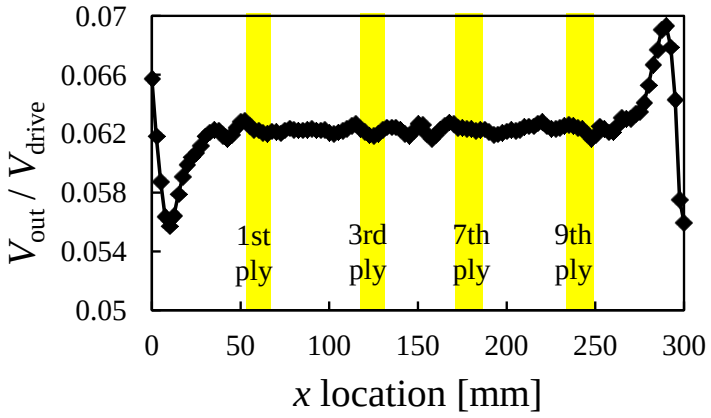

(b)

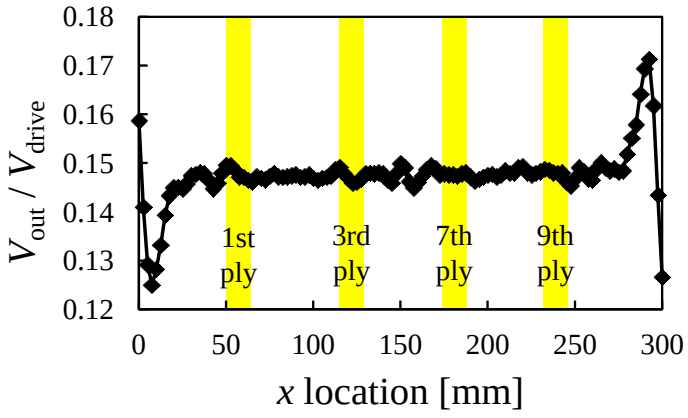

(c)

Fig. 3.16 Results obtained from top-surface measurement. Long sides of driver coil are directed in 90° direction of specimen #2: (a) 0.25 MHz, (b) 0.5 MHz, (c) 1 MHz.

represent the 0° and 90° fiber directions, respectively. The in-plane waviness zone is simulated in the area ranging $-5 < x < 5$ mm in the surface 0° layers by modifying the direction of electrical conductivity in elements. The waviness is represented as a half wavelength of the triangular wave, as shown in Fig. 3.17. Hence, directions of electrical conductivities are changed such that the fiber direction conductivity is directed along the triangular wave. The in-plane waviness is simulated over $-50 < y < 50$ mm, and has an amplitude of 2 mm and a length of 10 mm. The long sides of the rectangular driver coil are directed in the 0° fiber direction. The magnetic field in the 10 mm × 10 mm area 1 mm above the CFRP is calculated assuming that the drive frequency is 1 MHz. Only the z directional component of the magnetic field (H_z) is obtained because the output

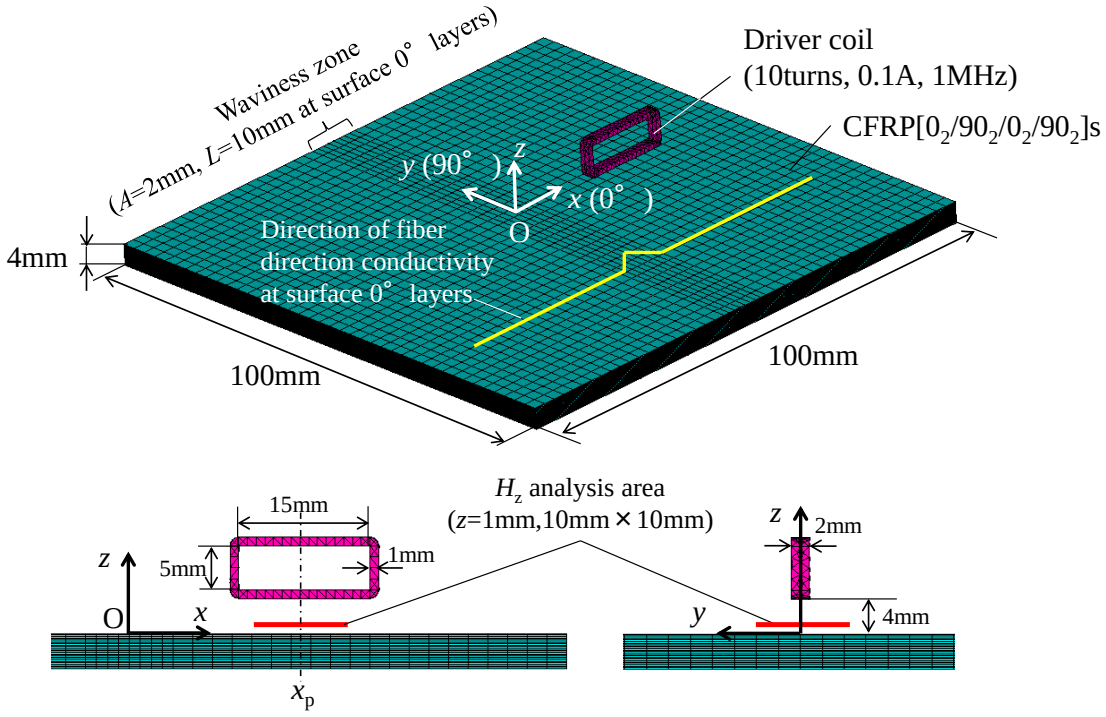

Fig. 3.17 Analytical model for the calculation of the magnetic field under the driver coil. In-plane waviness with amplitude of 2 mm and length of 10 mm is simulated at surface 0° layers. The driver coil is directed in the 0° fiber direction.

voltage of the pickup coil is generated by magnetic field normal to the loop. The x location of the center of the driver coil is denoted x_p. The magnetic field is calculated for x_p = −20, −7.5, 0, 7.5 and 20 mm. Fig. 3.18 shows FEM results of the magnetic field (H_z) for x_p = −20, −7.5, 0, 7.5 and 20 mm in the case that the fiber displacement in the waviness is the $+y$ direction in Fig. 3.17. Real and imaginary parts represent the in-phase and quadrature components with the drive current. At x_p = −20 and 20 mm, both Re(H_z) and Im(H_z) are antisymmetric with respect to y = 0. This result indicates that the magnetic fields penetrating the 10 mm × 10 mm area in $+z$ and $-z$ directions are equal to each other. Thus, the total magnetic flux penetrating a pickup coil placed immediately under the driver coil becomes zero, and no output voltage of the pickup coil is generated in the non-defective zone. At x_p = −7.5 and 7.5 mm, where the driver coil is close to the edge of the waviness zone, Re(H_z) is almost antisymmetric with respect to y = 0. No contribution of Re(H_z) to the generation of the pickup coil output

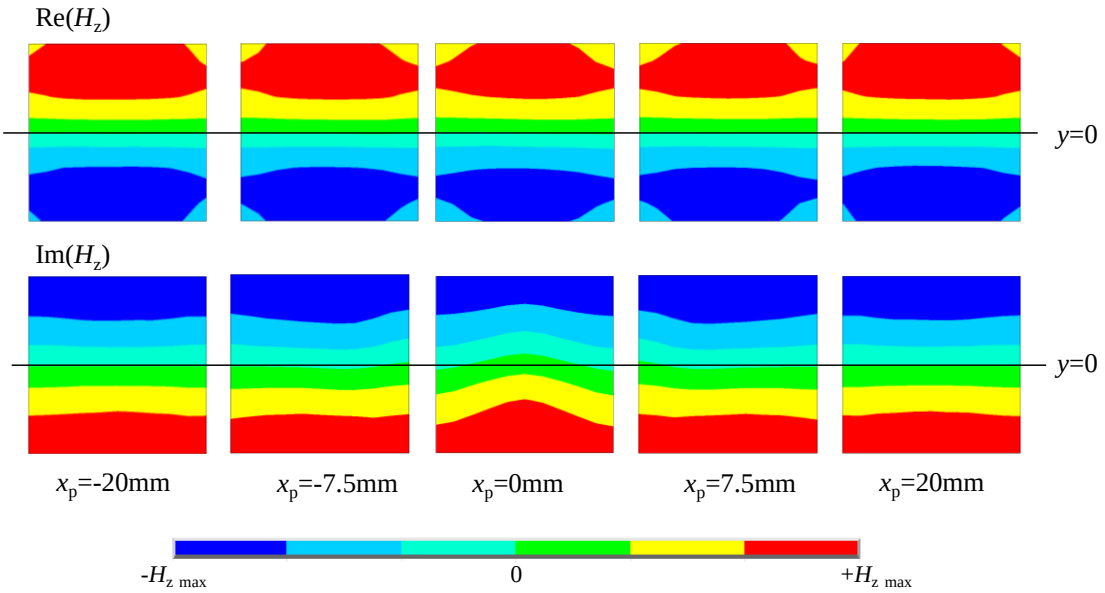

Fig. 3.18 Numerical results for the z directional component of the magnetic field. Long sides of the rectangular driver coil are directed in the 0° fiber direction, and fibers in simulated in-plane waviness are displaced in the + y direction in Fig. 3.17.

immediately under the driver coil is seen at x_p = −7.5 and 7.5 mm. However, the distribution of Im(H_z) is deformed and the area with Im(H_z) < 0 is slightly larger than that with Im(H_z) > 0. A change in pickup coil voltage can occur because of the deformation of the Im(H_z) distribution, which corresponds to the experimental results showing a signal change at the edges of the waviness zone. At x_p = 0, where the driver coil is immediately over the waviness zone, Re(H_z) still appears antisymmetric with respect to y = 0 like the other locations. The distribution of Im(H_z) is bent into the shape of in-plane waviness, which affects the pickup coil output. Fig. 3.19 shows the magnetic field distributions in the case that fiber displacement in the waviness is in the −y direction. Deformations of the Im(H_z) distribution at x_p = −7.5, 0 and 7.5 mm are opposite to those in Fig. 3.18. The results of FEM analyses shown in Figs. 3.18 and 3.19 can explain the physical background of experimental results shown in Figs. 3.13(a) and (b). In Fig. 3.18, Im(H_z) immediately under the center of the driver coil has negative

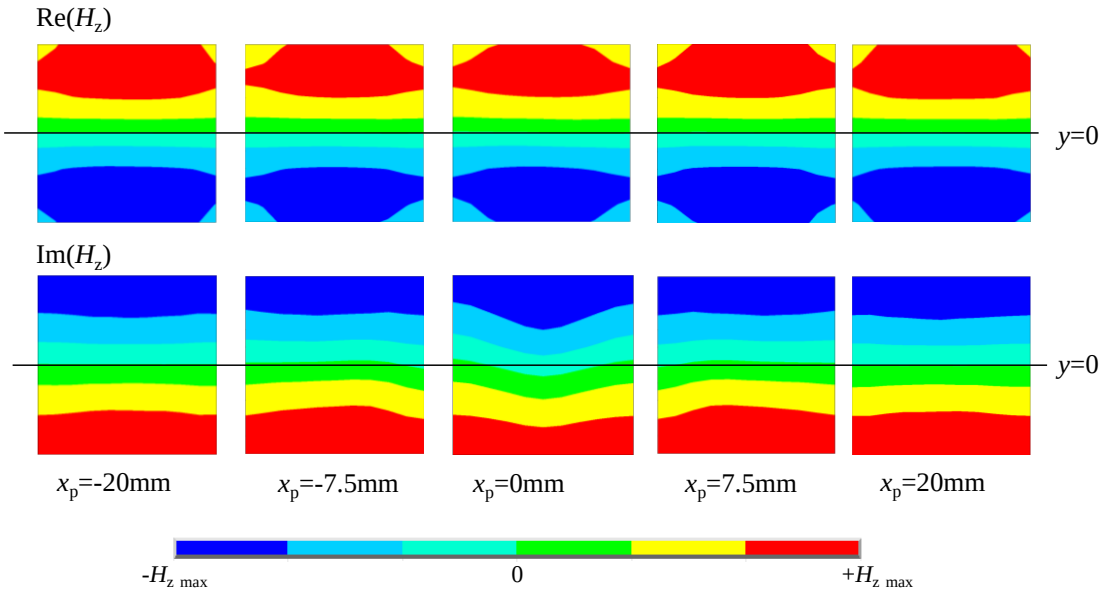

Fig. 3.19 Numerical results for the z directional component of the magnetic field. Long sides of the rectangular driver coil are directed in the 0° fiber direction, and fibers in simulated in-plane waviness are displaced in the −y direction in Fig. 3.17.

values at x_p = −7.5 and 7.5 mm and has a positive value at x_p = 0. By contrast, in Fig. 3.19, Im(H_z) immediately under the center of the driver coil has positive values at x_p = −7.5 and 7.5 mm and has a negative value at x_p = 0. The increase and decrease in the amplitude of the pickup coil output shown in Fig. 3.13 originate from positive and negative changes in Im(H_z). Moreover, the sequence of changes in the sign of Im(H_z) depends on the direction of fiber displacement in waviness, which caused the difference between Figs. 3.13(a) and (b). Therefore, the physical background of signal changes obtained in the experiments is verified by FEM analyses.

Second, the magnetic field distribution is calculated assuming that the long sides of the rectangular driver coil are directed in the 90° fiber direction of the cross-ply laminate. Fig. 3.20 shows the analytical model. The dimensions and stacking sequence

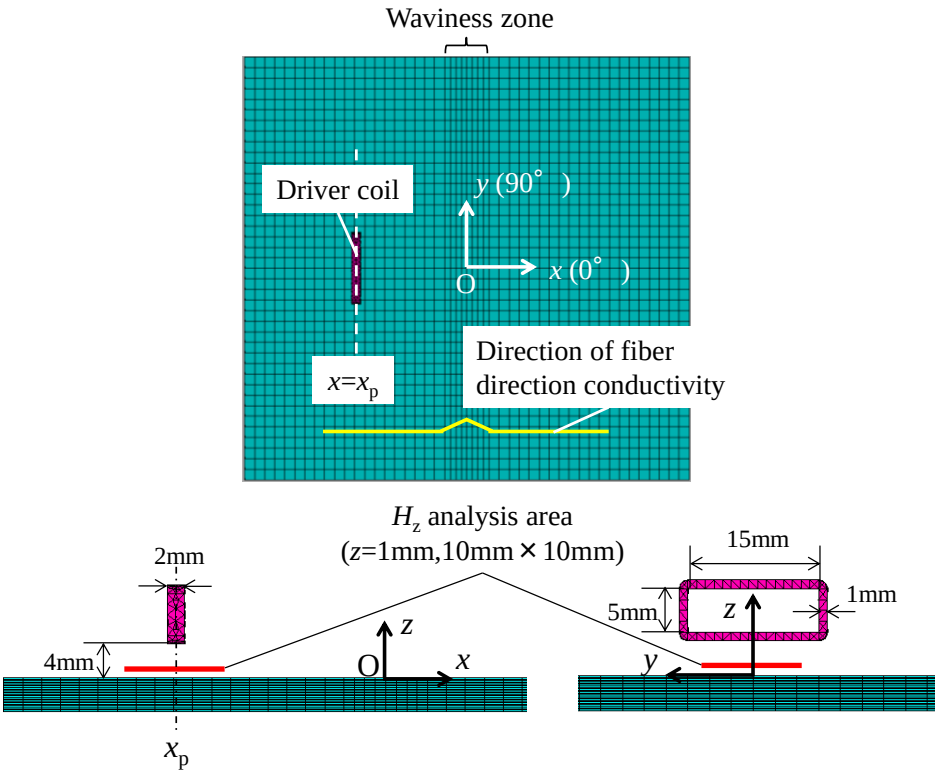

Fig. 3.20 Analytical model for the calculation of the magnetic field under the driver coil. The driver coil is directed in the 90° fiber direction.

of CFRP and the simulated in-plane waviness are the same as those in Fig. 3.17. H_z in the 10 mm × 10 mm area that is 1 mm above the CFRP surface is obtained for x_p = −10, −5, −2.5 and 0 mm. Fig. 3.21 shows FEM results of the H_z distribution. It is seen that both real and imaginary parts of the H_z distribution are almost antisymmetric with respect to $x = x_p$. These results indicate that when the long sides of the probe are directed in the 90° fiber direction, the output voltage of the pickup coil is almost zero even near waviness zones. This is because eddy currents are concentrated in 90° layers, and thus, waviness in the 0° layer does not distinctly affect the pickup coil output. The proposed probe can therefore detect in-plane waviness in the cross-ply laminate only when the direction of the driver coil corresponds to the fiber direction with waviness.

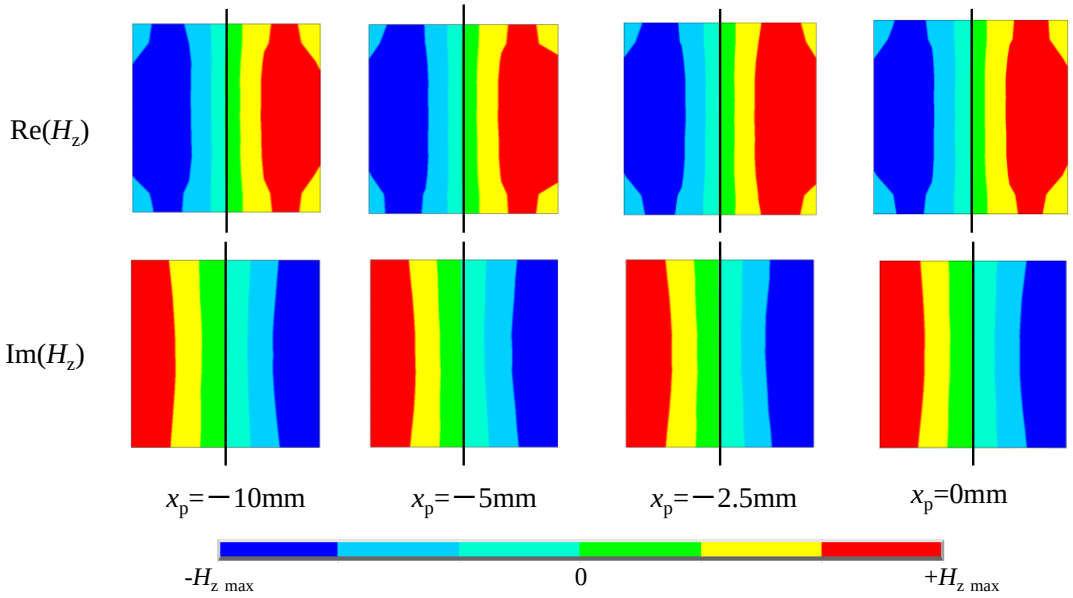

Fig. 3.21 Numerical results of the *z* directional component of the magnetic field. Long sides of the rectangular driver coil are directed in the 90° fiber direction.

3.3.4 Comparison with a conventional eddy current probe

To confirm that the proposed probe has higher sensitivity than conventional probe to

in-plane waviness, a half-transmission probe was used to inspect specimen #2. Fig. 3.22 shows the configurations of the half-transmission probe used in the experiments. The probe was composed of circular driver and pickup coils placed next to each other. The inner diameter, height and number of turns of the coils were 6 mm, 2 mm and 18, respectively. The probe was placed above the top surface of specimen #2 with a nominal lift-off of 0.5 mm. The probe scanned in the two ways shown in Figs. 3.23(a) and (b). In Fig. 3.23(a), the in-plane azimuth of the probe was set to 0°, and the probe scanned in the *x* direction. Meanwhile, in Fig. 3.23(b), the probe azimuth was 90°, and the probe scanned along the *x* axis. Drive frequencies used in the experiments were 1, 3 and 5

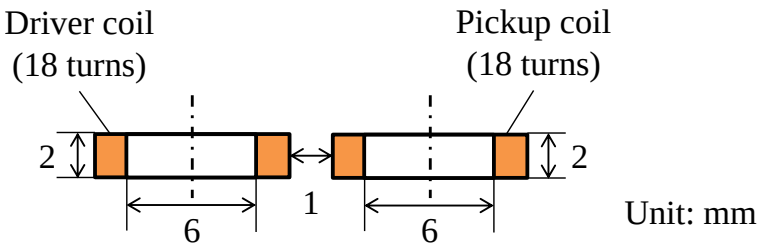

Fig. 3.22 Configurations of half-transmission probe. This probe is used to compare detectability of half-transmission probe and the proposed probe.

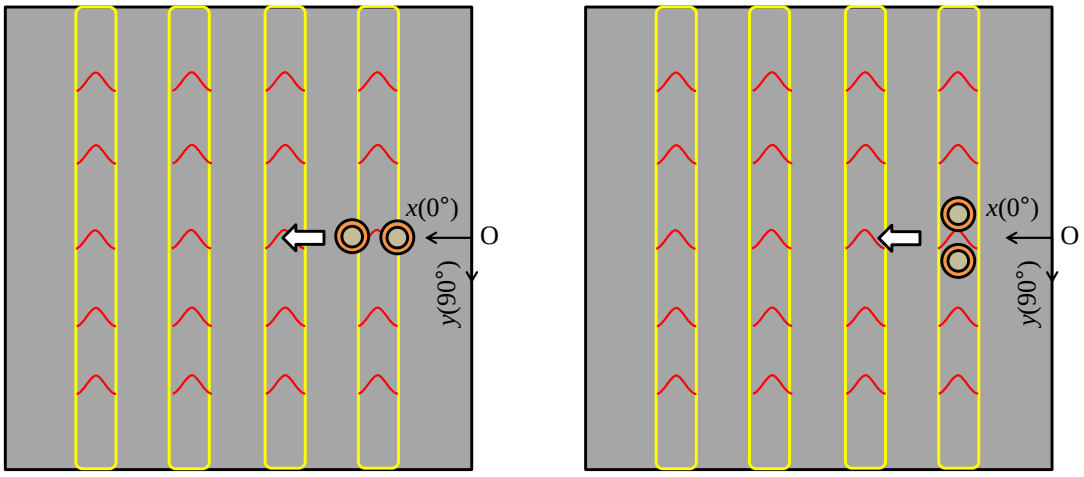

(a) (b)

Fig. 3.23 Experimental methods of using the half-transmission probe for the inspection of specimen #2: (a) probe azimuth of 0°, (b) probe azimuth of 90°.

MHz. The probe scanned at 2.5 mm intervals. Fig. 3.24 shows the results obtained when the probe azimuth was 0°. The horizontal axis denotes the *x* position of the midpoint between the driver and pickup coils. The vertical axis denotes the pickup coil voltage divided by the drive voltage. As seen in Figs. 3.24(a)–(c), no signal change can be observed at the locations of waviness. Although the proposed probe provides a clear signal change at waviness zones, as shown in Fig. 3.14, waviness in specimen #2 could not be detected using the half-transmission probe when the azimuth was 0°. Fig. 3.25 shows the result obtained when the azimuth of the half-transmission probe was 90°. As seen in Figs. 3.25(a)–(c), there was no distinct signal change even though the probe azimuth was changed to 90°. The proposed probe produced a clear signal change at waviness zones at drive frequencies of 1, 3 and 5 MHz, while the half-transmission probe did not. It was thus demonstrated that the proposed probe has better detectability of in-plane waviness than conventionally used half-transmission probe. One possible reason is the difference in the change ratio of the output signal at the waviness zone. The output signal of the half-transmission probe includes the effect of the excitation magnetic field from the driver coil. Since the magnetic field from eddy current is much weaker than the excitation field, the change in the eddy current path in CFRP does not produce a large change ratio of the half-transmission probe output. This possibly explains why the proposed probe has higher sensitivity to in-plane waviness.

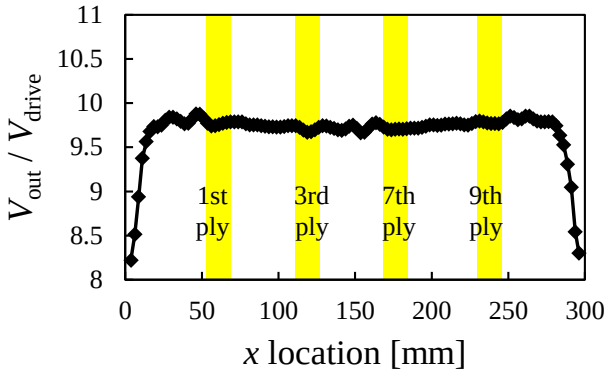

(a)

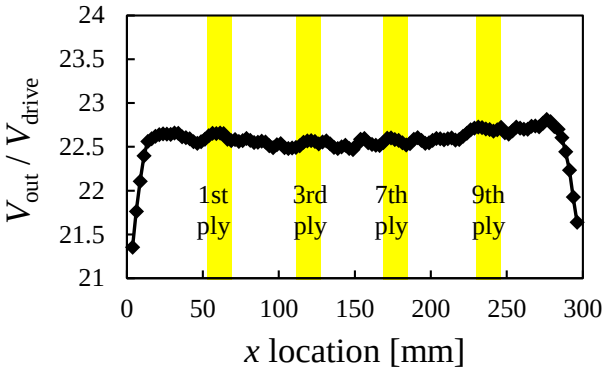

(b)

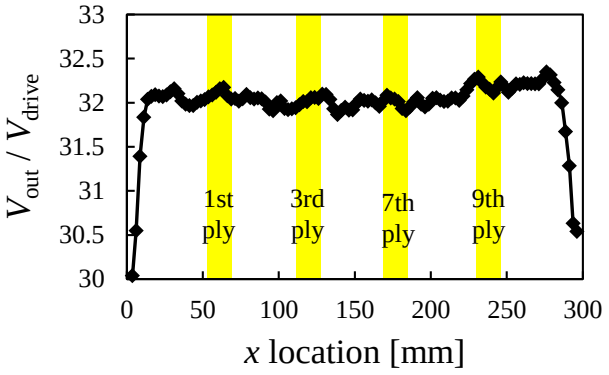

(c)

Fig. 3.24 Results of the top-surface measurement of specimen #2 obtained from the half-transmission probe, where the azimuth of the half-transmission probe is 0°: (a) 1 MHz, (b) 3 MHz, (c) 5 MHz.

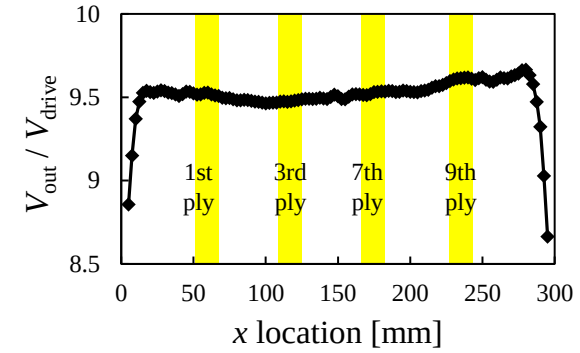

(a)

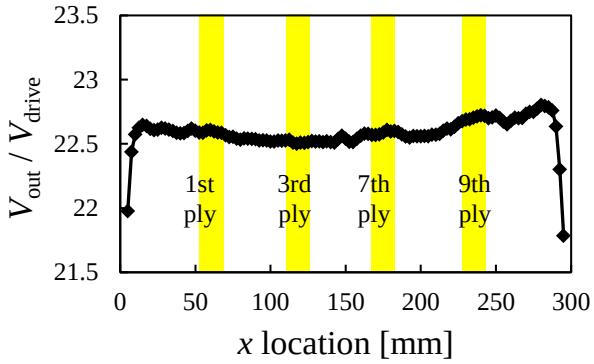

(b)

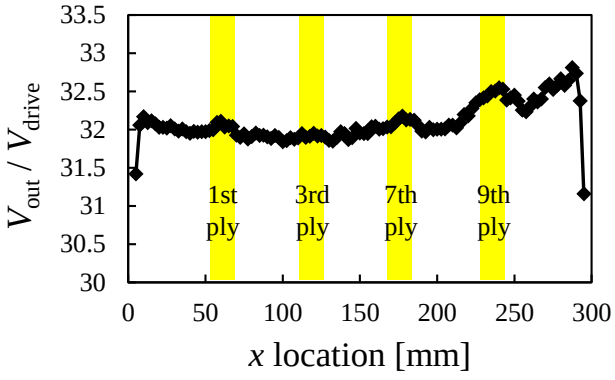

(c)

Fig. 3.25 Results of the top-surface measurement of specimen #2 obtained from the half-transmission probe, where the azimuth of the half-transmission probe is 90°: (a) 1 MHz, (b) 3 MHz, (c) 5 MHz.

3.4 Investigation of the effect of ±45° layers

The proposed probe can identify the fiber direction with waviness in a cross-ply laminate, as described in the previous section. The selectabilty of the inspected fiber direction can be qualitatively explained by analytical solutions to the line drive current-eddy current problem. However, analytical solutions cannot be obtained for laminates including ±45° layers because the presence of ±45° layers makes it difficult to solve Maxwell's equations. Hence, it remains unknown how to identify the fiber direction with waviness in the case of laminates including ±45° layers. We numerically investigated whether the proposed method can identify the wavy fiber direction in laminates including ±45° layers.

3.4.1 Eddy current distribution in a laminate with ±45° layers

The eddy current distribution in a laminate with ±45° layers was investigated in FEM analysis. The analytical model is similar to the model shown in Fig. 3.3. The dimensions of the CFRP plate and driver coil are the same as those in Fig. 3.3. The stacking sequence of CFRP under the driver coil is assumed to be $[0_2/45_2/-45_2/90_2]_s$. The values of electromagnetic properties are the same as those given in Table 3.1. The driver coil is directed in the 0° fiber direction. The drive frequency is assumed to be 1 MHz. Fig. 3.26 shows the eddy current vector distributions in $[0_2/45_2/-45_2/90_2]_s$. Distributions of the real part of eddy current density are displayed in Fig. 3.26. The figure shows that eddy currents flow along the fiber direction. Eddy currents are not concentrated in the fiber direction corresponding to the driver coil direction unlike the case for cross-ply laminate. Eddy currents in ±45° layers are not negligible. It is thus difficult to concentrate eddy currents in one fiber direction in the case of laminates including ±45° layers. Fig. 3.27

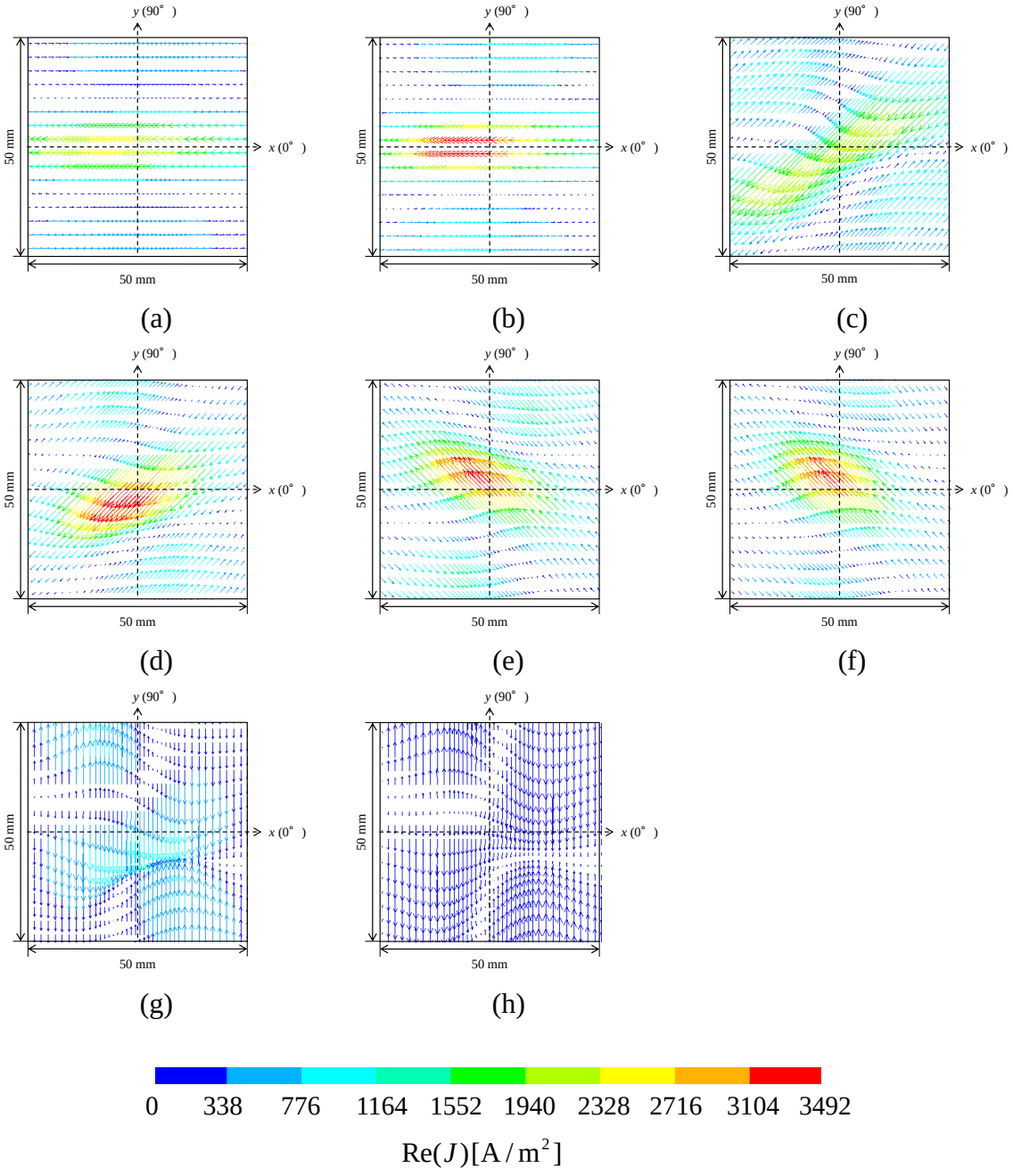

Fig. 3.26 Eddy current vector distribution in $[0_2/45_2/-45_2/90_2]_s$ calculated employing FEM, where the real part of the eddy current density vector in a 50 mm × 50 mm area under the driver coil is displayed: (a) first element layer from the surface (0° layer), (b) fourth element layer (0° layer), (c) fifth element layer (45° layer), (d) eighth element layer (45° layer), (e) ninth element layer (−45° layer), (f) 12th element layer (−45° layer), (g) 13th element layer (90° layer), (h) 16th element layer (90° layer).

shows the relationship between the maximum eddy current density and electrical conductivities in transverse and thickness directions of unidirectional ply. The maximum eddy current density strongly depends on conductivity in the thickness direction. This result is similar to the result obtained for cross-ply laminate shown in Fig. 3.7. Thus, a variation of electrical conductivity in the thickness direction affects the probe output during the inspection of a laminate with ±45° layers.

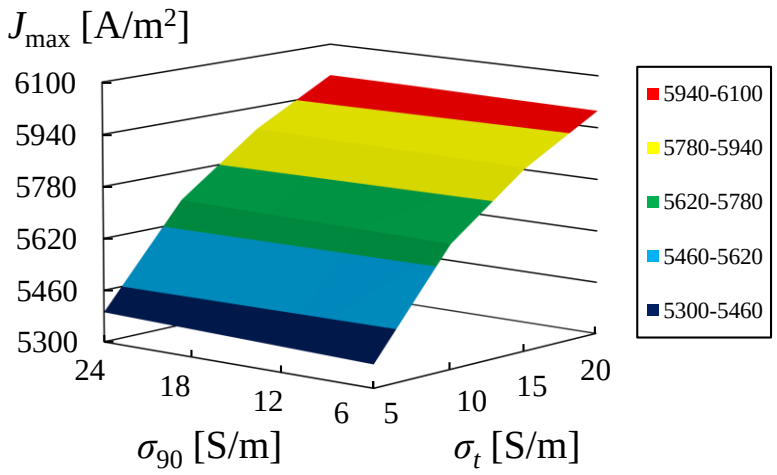

Fig. 3.27 Numerically calculated relationships between the maximum eddy current density in laminate with ±45° layers $[0_2/45_2/-45_2/90_2]_s$ and electrical conductivities in transverse and thickness directions of unidirectional ply.

3.4.2 Magnetic field distribution around waviness

The magnetic field around the waviness zone was numerically investigated. Although eddy currents cannot be concentrated in one fiber direction, identification of the wavy fiber direction is possible if the detectability of waviness changes with the probe azimuth. The analytical model used for the magnetic field calculation is similar to the model shown in Fig. 3.17. The dimensions of the CFRP plate and driver coil are the same as those in Fig. 3.17. The stacking sequence of the CFRP is assumed to be

$[0_2/45_2/-45_2/90_2]_s$. In-plane waviness is simulated at surface 0° layers, like the analytical model in Fig. 3.17. The in-plane waviness is induced over the CFRP width along the *y* direction, and its amplitude and length are 2 and 10 mm, respectively. The driver coil has 10 turns, and sinusoidal current with amplitude of 0.1 A and frequency of 1MHz is applied to the driver coil. The distribution of the *z* directional magnetic field (H_z) is investigated in the 10 mm × 10 mm area that is 1 mm above the CFRP plate (see Fig. 3.17). Calculations are made for in-plane driver coil azimuth angles of 0°, 45°, −45° and 90°. The *x* location of the driver coil (x_p) is varied among −20, −7.5, 0, 7.5 and 20 mm. Fig. 3.28 shows numerical results of the H_z distribution in the 10 mm × 10 mm area that is 1 mm above the CFRP plate at x_p = −20, −7.5, 0, 7.5 and 20 mm. Since the pickup coil is placed immediately under the driver coil, the magnetic field around the center of each image is important. In Fig. 3.28, the intersection of two lines represents the center of the 10 mm × 10 mm area. Distributions of the imaginary part of the magnetic field are antisymmetric when the driver coil is located at x_p = −20 and 20 mm (non-defective zones). These results show that the output voltage of a pickup coil placed at the center of the 10 mm × 10 mm area becomes zero at non-defective zones. As shown in Fig. 3.28(a), the imaginary part of H_z deforms into the shape of the simulated waviness when the driver coil is directed in the 0° fiber direction at x_p = 0. This result indicates that in-plane waviness affects the output signal when the pickup coil is placed at the center of the 10 mm × 10 mm area. Meanwhile, when the azimuth of the driver coil is 45°, −45° and 90°, deformation of the Im(H_z) distribution at x_p = 0 shown in Figs. 3.28(b)−(d) is much less than that obtained in the case of the 0° driver coil azimuth. It is thus predicted that the eddy current probe is the most sensitive to waviness when the driver coil is directed in the fiber direction with the waviness.

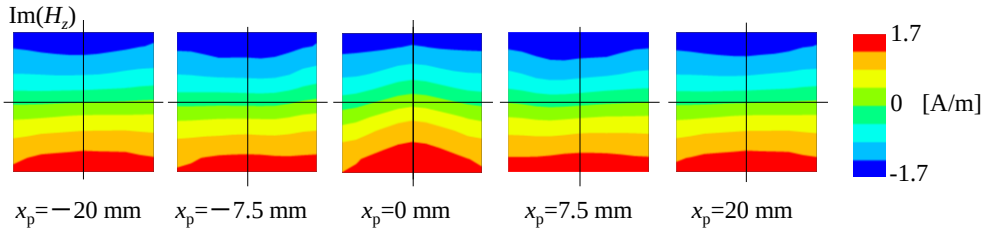

(a)

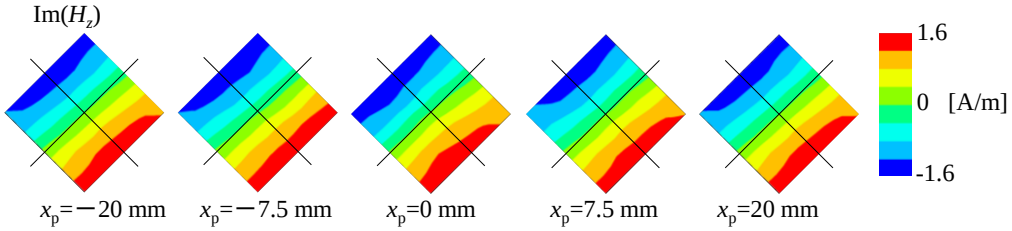

(b)

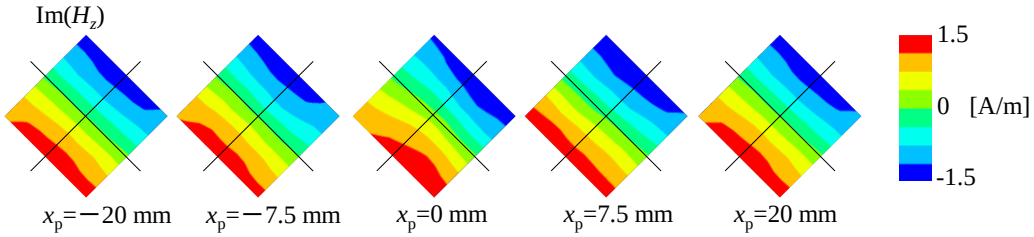

(c)

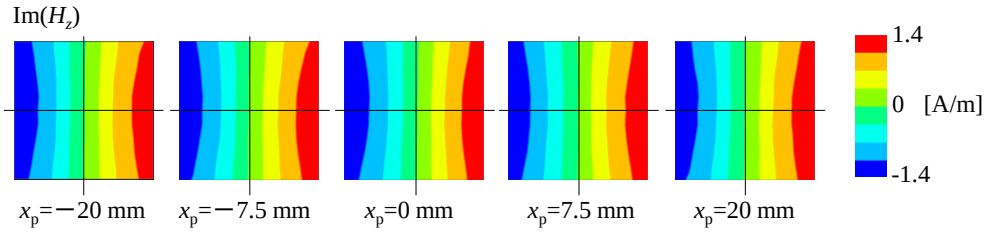

(d)

Fig. 3.28 Numerical results of the z directional component of the magnetic field obtained for $[0_2/45_2/-45_2/90_2]_s$: (a) driver coil azimuth of 0°, (b) driver coil azimuth of 45°, (c) driver coil azimuth of −45°, (d) driver coil azimuth of 90°.

3.4.3 Material

To investigate whether the proposed probe can detect in-plane waviness and identify the fiber direction with waviness, experiments were performed for a specimen with ±45° layers. Fig. 3.29 shows the CFRP laminate including ±45° layers used in the experiments (specimen #3). The length, width and thickness of the specimen were 300 mm, 270 mm and 4.8 mm, respectively. Specimen #3 was a 24-layer specimen with a stacking sequence of $[(0/45/0/-45/0/90)_2]_s$. Specimen #3 was fabricated using the same method as for specimen #2. In-plane waviness were artificially induced in the first, third and fifth 0° layers. Table 3.3 gives the sizes of in-plane waviness in specimen #3 measured by X-ray CT.

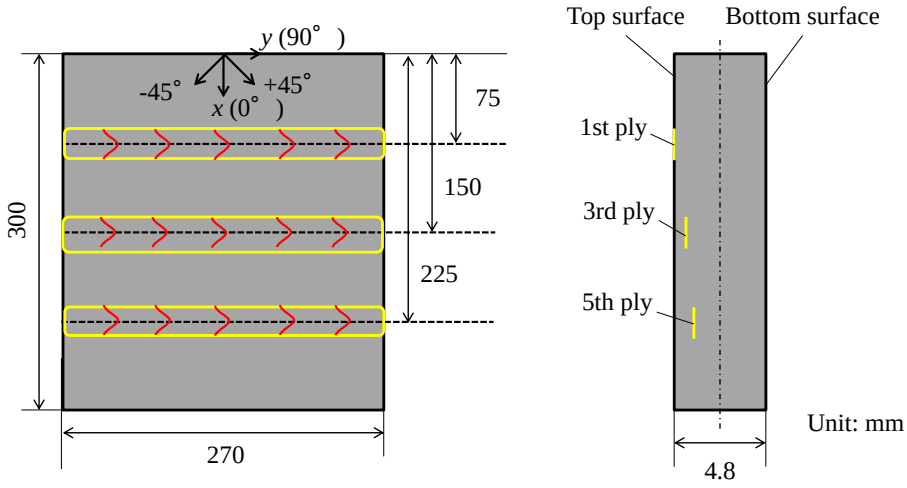

Fig. 3.29 CFRP laminate with in-plane waviness $[(0/45/0/-45/0/90)_2]_s$ (specimen #3).

Table 3.3 Sizes of in-plane waviness in specimen #3 measured from an X-ray CT image

Layer (from top surface)	Amplitude [mm]	Length [mm]	Angle [°]
first layer	1.23	12.3	13.8
third layer	0.99	13.4	10.0
fifth layer	1.56	13.4	16.2

3.4.4 Experimental setup

Fig. 3.30 shows the experimental setup. The probe was composed of a vertical rectangular driver coil and a pickup coil perpendicular to each other. The driver coil was a 20-turn rectangular coil with long and short sides of 20 and 7 mm, respectively. The pickup coil was a 6 mm × 5 mm rectangular coil with 15 turns. The diameters of the enameled copper wires used to turn the driver and pickup coils were 0.2 mm and 0.12 mm, respectively. The probe scanned along the *x* axis in Fig. 3.29 with a nominal lift-off of 0.5 mm. The experiments were performed for in-plane probe azimuth angles of 0°, 45°, −45° and 90°. An LCR meter (HIOKI E. E. CORPORATION, IM3536) supplied a 30 mA, 1 MHz sinusoidal current to the driver coil and measured the output voltage of the pickup coil. Impedance of the pickup coil was calculated as the pickup coil output divided by the drive current.

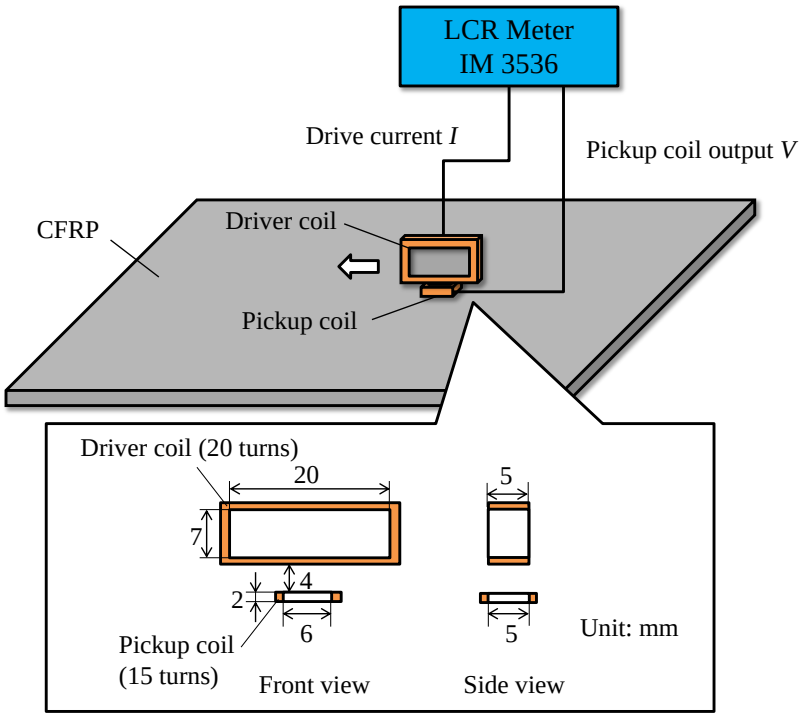

Fig. 3.30 Experimental setup for the inspection of specimen #3. The LCR meter supplies the drive current and measures the pickup coil voltage.

3.4.5 Results and discussion

Fig. 3.31 shows the results of ET of specimen #3. The horizontal axis denotes the *x* position of the probe, while the vertical axis denotes the impedance of the pickup coil. Fig. 3.31 (a) shows peaks of the pickup coil impedance at the locations of waviness. It is thus verified that the proposed probe can detect in-plane waviness in laminates including ±45° layers. This change in pickup coil impedance is result of the deformation of magnetic field distribution shown in Fig. 3.28(a). In Figs. 3.31 (b)–(d), there is no distinct peak of pickup coil impedance. The FEM results in Figs. 3.28 (b)–(d) show that the deformation of the magnetic field distribution caused by in-plane waviness in the 0° layer is smaller when the probe azimuth is 45°, –45° or 90°. This explains why the clear peaks of pickup coil impedance are observed only when the probe azimuth is 0°. According to the results shown in Fig. 3.31, the 0° fiber direction can be identified as the fiber direction with in-plane waviness.

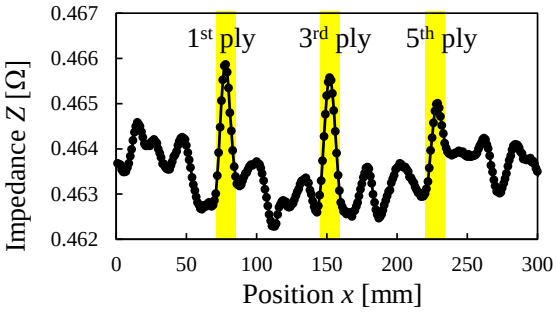

(a)

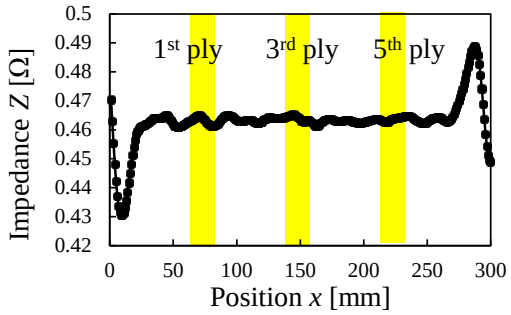

(b)

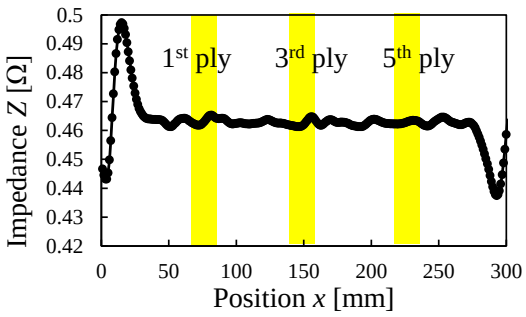

(c)

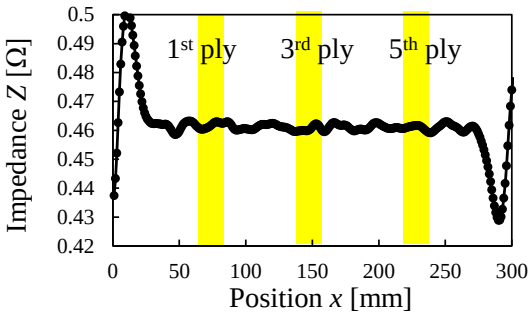

(d)

Fig. 3.31 Results of ET obtained for specimen #3: (a) probe azimuth of 0°, (b) probe azimuth of 45°, (c) probe azimuth of –45°, (d) probe azimuth of 90°.

3.5 Conclusions of Chapter 3

An eddy current probe specialized for the detection of in-plane waviness in CFRP laminates is proposed. The probe is sensitive to the in-plane deformation of the eddy current path, and can select fiber layers to be inspected through a change in the in-plane probe azimuth when the tested CFRP is a cross-ply laminate. The layer selectability was explained by two-dimensional analytical solutions for the vector potential derived in Chapter 2 and three-dimensional FEM analysis. Analytical solutions for the vector potential show that the eddy current distribution depends only on the conductivity in the drive current direction when the drive current is directed in the 0° or 90° fiber direction of cross-ply laminates. Moreover, the analytical solution shows that eddy currents are concentrated in layers with carbon fibers corresponding to the drive current direction. This was verified by three-dimensional FEM analyses. It was found that near the driver coil, eddy currents are directed only in the direction of the driver coil and concentrated in carbon fibers in that direction. Hence, the proposed method can select in which layers of the cross-ply laminate eddy currents are concentrated.

The proposed probe was used to detect artificially induced in-plane waviness in cross-ply CFRP laminates. It was found that the output signal of the pickup coil has a local maximum at the edges of the waviness zone and has a local minimum at the vertex of the waviness. In contrast, for the opposite direction of the fiber displacement in waviness, the pickup coil has a local minimum value at the vertex of the waviness, and a local maximum value at the vertex of the waviness. These results imply that the length of the waviness zone and direction of fiber displacement can be identified from the variation of the pickup coil output. Subsequently, measurements were performed for a 20-layer cross-ply CFRP specimen with in-plane waviness at different depths. The

probe produced a recognizable signal change at the location of waviness 18 layers from the surface at a drive frequency of 0.25–1 MHz.

The magnetic field distribution around the waviness zone in a cross-ply laminate was investigated in FEM analyses. It was found that the distribution of the imaginary part of the magnetic field normal to the CFRP surface is deformed around waviness, which affects the output voltage of the pickup coil. Furthermore, FEM analyses showed that the sequence of positive and negative changes in the pickup coil output obtained when scanning with the probe depends on the direction of fiber displacement in waviness. In addition, we investigated the magnetic field distribution when the direction of the driver coil is perpendicular to the fiber direction with waviness. Almost no change in the magnetic field was observed in this case.

We investigated whether the fiber direction with waviness can be identified in the case of testing laminates including ±45° layers. According to FEM analyses of $[0_2/45_2/-45_2/90_2]_s$ laminate, it is not possible to concentrate eddy currents in one fiber direction. However, FEM analyses revealed that deformation of the magnetic field caused by waviness is largest when the direction of the driver coil corresponds to the fiber direction with the waviness. Hence, the proposed probe is most sensitive to in-plane waviness when the probe azimuth corresponds to the fiber direction with the waviness. Identification of the fiber direction with waviness is possible even for the inspection of laminates including ±45° layers. Experimental results showed that the proposed probe produces a clear change in the pickup coil output at the locations of fiber waviness. Moreover, distinct peaks of the pickup coil output were observed at waviness zones only when the probe was directed in the fiber direction with waviness. Thus, the wavy fiber direction can be identified even if the tested laminate includes ±45° layers.

In conclusion, it was verified in experiments that the proposed probe can detect waviness only when the direction of the driver coil corresponds to that of the carbon fiber with waviness. In the experiments described in this chapter, a recognizable change in probe output was obtained from in-plane waviness up to 18 layers from the inspected surface of a 20-layer cross-ply laminate. The waviness in the 18^{th} layer from the surface had a misalignment angle of 24.9°. The minimum misalignment angle of detected waviness in the cross-ply laminate $[(0/90)_5]_s$ was 6.9°, and the waviness was located in the first layer of the laminate. The waviness with a minimum misalignment angle detected in the measurement for the laminate with a stacking sequence of $[(0/45/0/-45/0/90)_2]_s$ had an angle of 10.0° and was located in the third layer from the surface.

3.6 References

[3.1] H. Heuer, M. Schulze, M. Pooch, S. Gabler, A. Nocke, G. Bardl, Ch. Cherif, M. Klein, R. Kupke, R. Vetter, F. Lenz, M. Kliem, C. Bülow, J. Goyvaerts, T.Mayer, S. Petrenz, "Review on quality assurance along the CFRP value chain e Nondestructive testing of fabrics, preforms and CFRP by HF radio wave techniques", Composites: part B, Vol. 77, (2015), pp. 494-501.

[3.2] Carsten Schmidt, Cedric Schultz, Patricc Weber, Berend Denkena, "Evaluation of eddy current testing for quality assurance and process monitoring of automated fiber placement", Composites: Part B, Vol. 56, (2014), pp. 109-116.

[3.3] Akira Todoroki, "Skin Effect of Alternating Electric Current in Laminated CFRP", Advanced Composite Materials, Vol. 21, Nos. 5-6, (2012), pp. 477-489.

[3.4] W. S. Chang and J. S. Wang, "Influence of fiber waviness on the structural response of composite laminates", Journal of Thermoplastic Composite Materials, Vol. 7, (1994), pp. 243-260.

[3.5] J. C. Abry, S. Bochard, A. Chateauminois, M. Salvia, G. Giraud, "In situ detection of damage in CFRP laminates by electrical resistance measurements", Composites Science and Technology, Vol. 59, (1999), pp. 925-935.

[3.6] Jun Cheng, Hongli Ji, Jinhao Qiu, Toshiyuki Takagi, Tetsuya Uchimoto, Ning Hu, "Role of interlaminar interface on bulk conductivity and electrical anisotropy of CFRP laminates measured by eddy current method", NDT & E International, Vol. 68, (2014), pp.1-12.

[3.7] Hiroshi Hoshikawa and Kiyoshi Koyama, "Study on eddy current and electric potential gradient in electromagnetic induction", Journal of the Japanese Society for Non-destructive Inspection, Vol. 58, No. 7, (2009), pp. 274-280.

[3.8] Yoshiyasu Hirano, Takuya Yamane and Akira Todoroki, "Through-thickness electric conductivity of toughened carbon-fibre reinforced polymer laminates with resin-rich layers", Composites Science and Technology, Vol. 122, (2016), pp. 67-72.

Chapter 4

Eddy current imaging technique for visualization of in-plane fiber waviness

4.1 Background

In this chapter, an eddy current imaging technique for estimation of the size of in-plane waviness is proposed. Conventionally, the eddy current-based approach of visualizing defects has adopted inverse analyses [4.1]–[4.6]. Inverse analyses can be used to estimate sizes of defects if the tested material is isotropic conductive materials. Perturbation of the electromagnetic field produced by a defect can be obtained in the form of an analytical solution in the case of isotropic conductive materials [4.1]–[4.5]. FEM analyses are also available for solving forward problem, and a comparison with experimental data allows an estimation of the defect size [4.6]. On the other hand, an analytical solution for the perturbation of the electromagnetic field caused by a defect in CFRP has not been derived because of anisotropy and the multilayered structure. Hence, a change in electromagnetic field caused by in-plane waviness is not available in the form of an analytical solution. Moreover, it is difficult to realize good agreement between experimental data and FEM results because there is a variation of electrical conductivity within CFRP laminates, unlike the case for metal.

In Chapter 3, eddy current technique to detect in-plane waviness and identify the fiber direction with the waviness was developed. In this chapter, a method to estimate the size of in-plane waviness at the location of the detected waviness is proposed. Because eddy currents flow along carbon fibers in CFRP, the size of waviness can be estimated if the eddy current path can be visualized. We propose a method to identify the eddy current path by measuring the magnetic field. The effectiveness of the proposed method was investigated through FEM analyses and experiments. The proposed method was applied to multidirectional CFRP with artificially induced in-plane waviness.

4.2 Method

4.2.1 Magnetic field measurement strategy for visualizing eddy current path

We propose a method to estimate the eddy current path from the magnetic field in this study. Fig. 4.1 is a schematic representation of the proposed eddy current imaging method for estimating the shape and size of in-plane waviness. Two types of coil are used: a driver coil and pickup coil. The driver coil generates a magnetic field and induces eddy current in the tested CFRP. The pickup coil measures the resulting magnetic field generated by the drive current and eddy current.

In this method, a vertical rectangular driver coil is fixed above a region with waviness and is directed in the fiber direction with the waviness. For example, if the waviness is located in the 0° fiber direction of the CFRP, the rectangular driver coil is placed above the CFRP such that it is directed in the 0° fiber direction as shown in Fig. 4.1. It is assumed that x and y locations of the in-plane waviness and fiber orientation with waviness are known in advance. This is because the location of waviness and the fiber direction with the waviness can be identified using the eddy current probe developed in Chapter 3. The in-plane azimuth of the vertical rectangular driver coil is important for

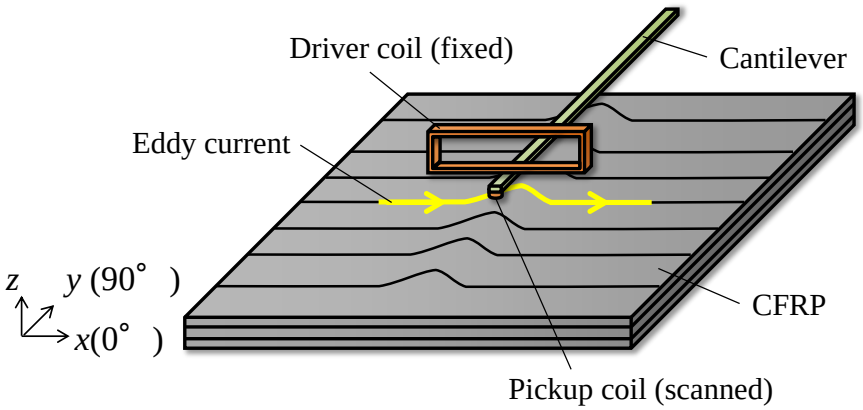

Fig. 4.1 Schematic representation of the proposed eddy current imaging method for estimation of the shape and size of waviness.

determining in which fiber direction eddy currents are induced. Chapter 3 showed that when the rectangular driver coil is directed in the 0° fiber direction of a cross-ply laminate, eddy currents are concentrated only in 0° layers under the driver coil. Hence, layers to be inspected can be selected by changing the in-plane probe azimuth. This excitation method is useful also for visualization of the wavy eddy current path from the magnetic field. The magnetic field generated by eddy current in the fiber direction perpendicular to the driver coil direction can be eliminated if the tested CFRP is a cross-ply laminate.

The eddy current path is estimated from the magnetic field distribution measured by scanning the sample surface with the pickup coil. Visualization of electric currents based on magnetic field measurement is employed in a wide variety of research fields [4.7]–[4.10]. It is commonly reported that the measurement of the magnetic field component perpendicular to the plane in which electric currents flow is an effective way to visualize the electric current paths. For example, when the electric currents are distributed in the *x*-*y* plane, the *z* directional component of the magnetic field (H_z) is measured. Because the *z* directional magnetic field becomes zero above a line current element according to the Biot–Savart law, the $H_z = 0$ line offers a good estimation of the current paths. Most studies visualizing electric current focus on current generated by the electric potential gradient using electrodes on the sample. Meanwhile, the path of current induced by electromagnetic induction has not been obtained from the H_z distribution to the best of the author's knowledge. This is because the magnetic field from the driver coil is included in the measured magnetic field. The magnetic field from the drive current prevents the $H_z = 0$ line from corresponding to the eddy current path. In this study, a new complex plane analysis method is developed to remove the effect of

the magnetic field generated by the driver coil. The magnetic field generated by the drive current is in-phase with the drive current. On the other hand, eddy current induced by the drive current is generally not in-phase with the drive current. Hence, the magnetic field component that is out-of-phase with the drive current does not include the magnetic field from the drive current. The quadrature magnetic field is generated only from the eddy current. This physical background can be seen in analytical solutions for the electromagnetic field derived in Chapter 2. Fig. 4.2 shows the analytical model of two opposing line currents placed above unidirectional CFRP. It is assumed that the fiber direction of the unidirectional CFRP is the *x* direction in Fig. 4.2. The line drive current is infinitely long in the *x* direction. Hence, the line current in Fig. 4.2 represents the sides of the vertical rectangular coil parallel to the CFRP surface when the lengths are sufficiently long. The vector potential in the region between the CFRP and bottom of the line drive currents ($0 < z < l_1$) is expressed as Eq. (4.1).

$$\boldsymbol{A}(y,z) = \begin{pmatrix} A_d(y,z) + A_e(y,z) \\ 0 \\ 0 \end{pmatrix} \tag{4.1}$$

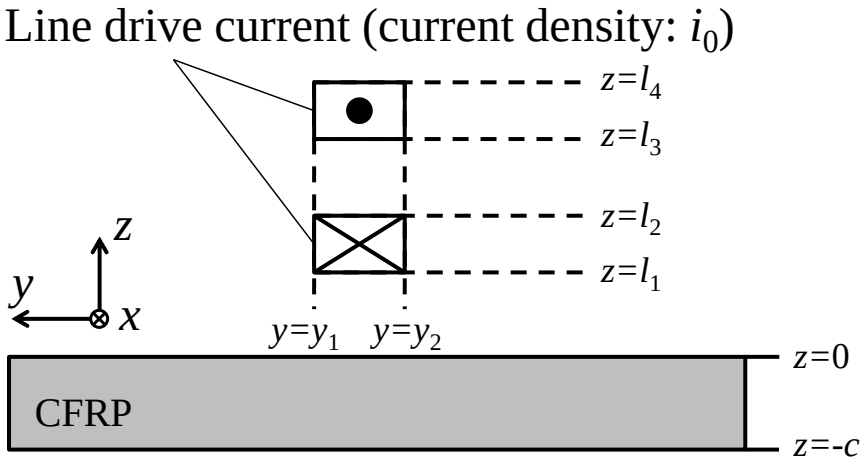

Fig. 4.2 Analytical model of line drive currents placed above CFRP directed in opposite directions to each other.

A_d and A_e are expressed as the following equations.

$$A_d(y,z) = \frac{\mu_0 i_0}{2\pi}\int_0^\infty \frac{1}{\alpha^3} e^{\alpha z}\left\{(e^{-\alpha l_2} - e^{-\alpha l_1}) - (e^{-\alpha l_4} - e^{-\alpha l_3})\right\} \times \left\{\sin\alpha(y-y_2) - \sin\alpha(y-y_1)\right\} d\alpha \tag{4.2}$$

$$A_e(y,z) = \frac{\mu_0 i_0}{2\pi}\int_0^\infty \frac{1}{\alpha^3} \frac{\left(\alpha^2 - {\alpha_3}^2\right)\left(1 - e^{-2\alpha_3 c}\right)e^{-\alpha z}}{\left(\alpha_3+\alpha\right)^2 - \left(\alpha_3-\alpha\right)^2 e^{-2\alpha_3 c}} \left\{(e^{-\alpha l_2} - e^{-\alpha l_1}) - (e^{-\alpha l_4} - e^{-\alpha l_3})\right\} \times \left\{\sin\alpha(y-y_2) - \sin\alpha(y-y_1)\right\} d\alpha \tag{4.3}$$

where

$$\alpha_3 = \left(\alpha^2 + j\omega\mu_0\sigma_0\right)^{1/2} \tag{4.4}$$

Here, i_0 is the drive current density, μ_0 is magnetic permeability in a vacuum, ω is the angular drive frequency, σ_0 is electrical conductivity in the fiber direction of unidirectional CFRP and j is the imaginary unit. A_d is independent of electrical conductivity of CFRP according to Eq. (4.2). Only A_e depends on electrical conductivity of CFRP, as shown in Eq. (4.3). Furthermore, Eq. (4.3) shows that A_e becomes zero when the electrical conductivity of the tested material is zero. It follows that A_d is a vector potential generated by drive current, while A_e is that generated by eddy current. Eq. (4.2) shows that A_d has only a real part, which indicates that A_d is in-phase with the drive current. Meanwhile, A_e is a complex number and is generally not in-phase with the drive current. Because the magnetic field is a rotation of the vector potential, the magnetic field is also divided into fields generated by the driver coil and eddy current. Hence, the z directional magnetic field in the region between the CFRP and bottom of the line drive currents can be written as Eq. (4.5).

$$H_z = H_d + H_e \tag{4.5}$$

where

$$H_{\mathrm{d}} = \mathrm{Re}(H_{\mathrm{d}}) \tag{4.6}$$

$$H_{\mathrm{e}} = \mathrm{Re}(H_{\mathrm{e}}) + j\,\mathrm{Im}(H_{\mathrm{e}}) \tag{4.7}$$

Thus, when the drive current is assumed to be a phase reference (i.e., the real part in the complex plane), the imaginary part of H_z (Im(H_z)) represents the magnetic field from the eddy current. Therefore, the eddy current path can be estimated from a line on which Im(H_z) becomes zero and the size of waviness can be estimated.

4.2.2 FEM analyses of magnetic field distribution in waviness zone

To confirm that the Im(H_z) = 0 line allows a good estimation of the waviness size, FEM analyses are performed using the general-purpose FEM analysis software ANSYS. Fig. 4.3 shows an analytical model of the proposed eddy current imaging method. A vertical rectangular driver coil is placed above a CFRP plate with simulated in-plane waviness. The rectangular driver coil has length of 15 mm, width of 5 mm and height of 2 mm. The lift-off of the driver coil is set to 4 mm. It is assumed that the driver coil has

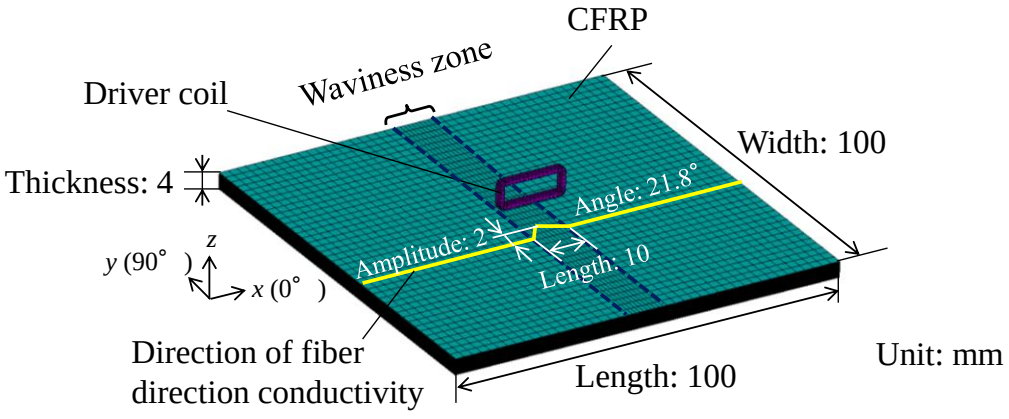

CFRP Stacking sequence: $[0_2/90_2/0_2/90_2]$s or $[0_2/45_2/\text{-}45_2/90_2]$s

Fig. 4.3 Analytical model of eddy current imaging. Triangular waviness is simulated somewhere in 0° layers along the width of CFRP plate.

10 turns, and a sinusoidal current with amplitude of 0.1 A is applied to the driver coil. The length, width and thickness of the CFRP plate are 100, 100 and 4 mm, respectively. The shape of the in-plane waviness is assumed to be a half-wavelength of a triangular wave as shown in Fig. 4.3. The in-plane waviness is simulated by modifying the direction of electrical conductivity of the elements in the waviness zone. Directions of the electrical conductivity are modified such that fiber-direction conductivity is directed along the triangular wave. The waviness is induced along the width of the CFRP. In all calculations, the amplitude and length of the waviness are 2 and 10 mm, respectively. The angle of the waviness is calculated as 21.8° from the inverse tangent. The distribution of H_z at the surface of the CFRP is calculated. The calculations are made for CFRPs with stacking sequences of $[0_2/90_2/0_2/90_2]_s$ and $[0_2/45_2/-45_2/90_2]_s$. Material properties used for calculations are listed in Table 4.1 [4.11].

First, the distribution of H_z at the surface of a 16-layer cross-ply laminate $[0_2/90_2/0_2/90_2]_s$ is investigated while varying the drive frequency and the depth of in-plane waviness. Drive frequencies used in the calculations are 0.25, 1 and 4 MHz. There are three cases of the depth of in-plane waviness: in-plane waviness in the first and second layers, the fifth and sixth layers, and the 11^{th} and 12^{th} layers. Because in-plane waviness is located in the 0° layers in all three cases, the driver coil was directed in the 0° fiber direction as depicted in Fig. 4.3. Fig. 4.4 shows the distribution

Table 4.1 Material properties of CFRP used for FEM analyses

Material property	Value
Conductivity in fiber direction [S/m]	34120
Conductivity in transverse direction [S/m]	24
Conductivity in thickness direction [S/m]	20
Magnetic permeability [H/m]	1.26×10^{-6}

of Im(H_z) at the surface of the CFRP when the in-plane waviness is located in first and second layers. Fig. 4.4 presents a 30 mm × 30 mm area under the driver coil. As the dotted lines in Fig. 4.4 show, the Im(H_z) = 0 line is deformed at the location of waviness and corresponds to the shape of the simulated waviness. Lengths of the deformation of the Im(H_z) = 0 line are 9.67–9.77 mm for the three frequencies used in the calculations. There is thus good agreement with the length of the simulated waviness (10 mm). The amplitude of the Im(H_z) = 0 line in Fig. 4.4(c) is the closest to that of the simulated waviness (2 mm). The error is approximately 10 %. However, the amplitude of waviness estimated from the Im(H_z) = 0 line has larger error as the drive frequency decreases. This is because the magnetic field from eddy current in 0° layers without waviness is included in the magnetic field. For visualization of the eddy current path, it is desirable that eddy current flows only in a layer with in-plane waviness. However, in reality, eddy currents are distributed in several layers in the laminate and attenuate in the

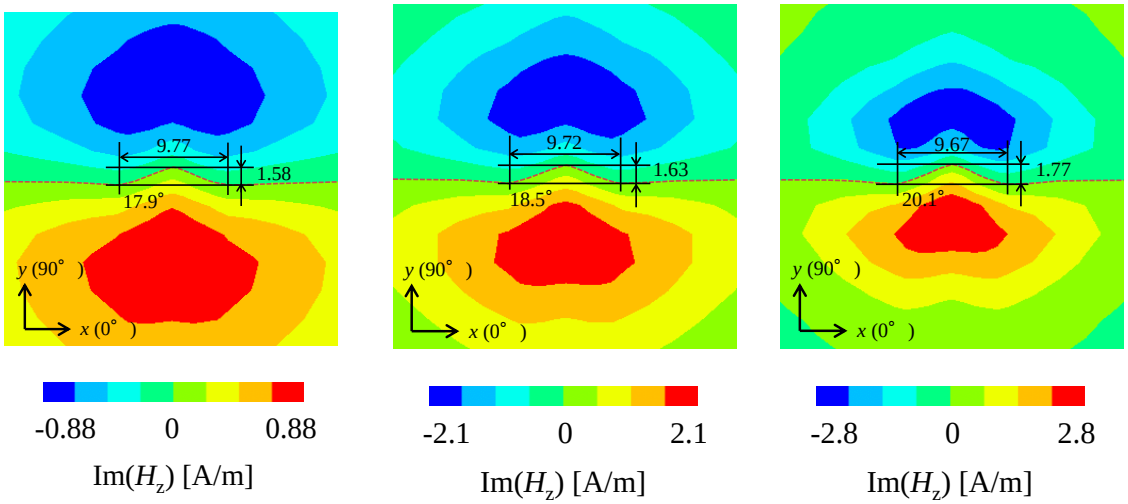

(a) (b) (c)

Fig. 4.4 Im(H_z) distributions at the CFRP surface when in-plane waviness is located in the first and second layers of the cross-ply laminate with the stacking sequence of $[0_2/90_2/0_2/90_2]_s$ (30 mm × 30 mm area under the driver coil): (a) 0.25 MHz, (b) 1 MHz, (c) 4 MHz (unit: millimeters).

thickness direction because of the skin effect. Hence, the magnetic field from eddy currents in non-defective layers can be included in the Im(H_z) distribution, which results in underestimation of the amplitude of the waviness. According to the skin effect, eddy currents can be more concentrated near surface layers at higher frequency. When the in-plane waviness is located at the surface layer of the CFRP, the use of a higher drive frequency can offer better accuracy in the estimation of the waviness size. This is because non-defective layers below the top wavy layers have less effect on the magnetic field. This is the reason why the amplitude of the Im(H_z) = 0 line obtained at a higher drive frequency is in better agreement with the amplitude of the simulated waviness. Fig. 4.5 shows the Im(H_z) distribution in the case that in-plane waviness is located in the fifth and sixth layers. The wavy shape of the Im(H_z) = 0 line can be observed even though waviness is located inside the CFRP. However, the estimated waviness amplitudes have larger errors relative to the results presented in Fig. 4.4. Estimated

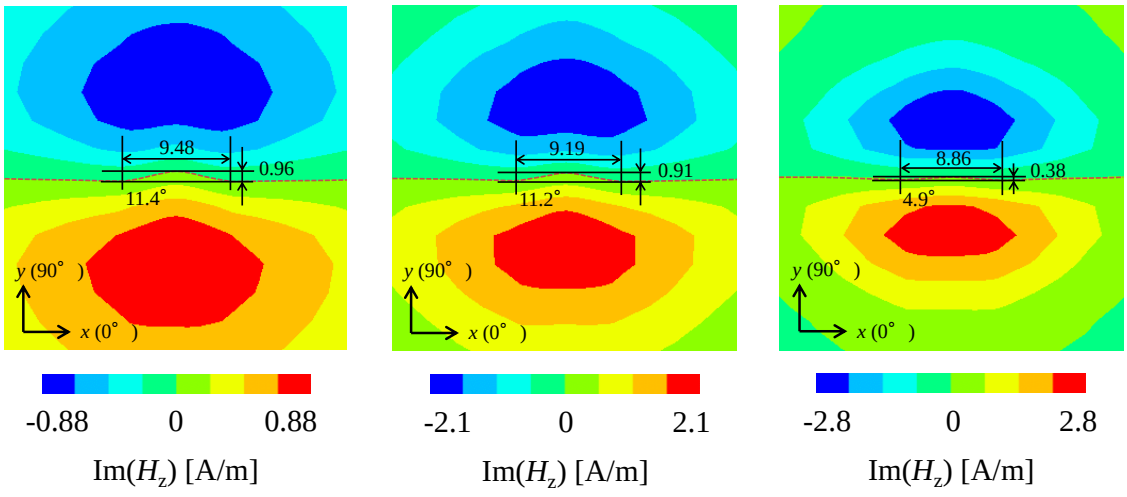

(a) (b) (c)

Fig. 4.5 Im(H_z) distributions at the CFRP surface when in-plane waviness is located in the fifth and sixth layers of the cross-ply laminate with the stacking sequence of $[0_2/90_2/0_2/90_2]_s$ (30 mm × 30 mm area under the driver coil): (a) 0.25 MHz, (b) 1 MHz, (c) 4 MHz (unit: millimeters).

amplitudes of the waviness are underestimated and are less than half the simulated size. This is because of the effect of the magnetic field from eddy currents in top 0° layers. Because eddy currents have larger amplitude near surface layers, the magnetic field from eddy current in the surface 0° layers is dominant in the Im(H_z) distribution. The resulting magnetic field obtained in the Im(H_z) image is the sum of the magnetic fields from all layers, which leads to a reduced amplitude of the Im(H_z) = 0 line. There is thus underestimation of the amplitude of waviness in deeper regions. This physical background explains why the estimated waviness size has larger error at higher frequency. At higher frequency, eddy currents are concentrated more in the surface 0° layers, and the amplitude of the eddy currents in deeper region becomes smaller. This reduces the contribution of eddy currents in the wavy layer to the Im(H_z) distribution, and thus, the Im(H_z) = 0 line has an amplitude that is smaller than the actual size of waviness. To obtain the Im(H_z) = 0 line that has an amplitude closer to the size of

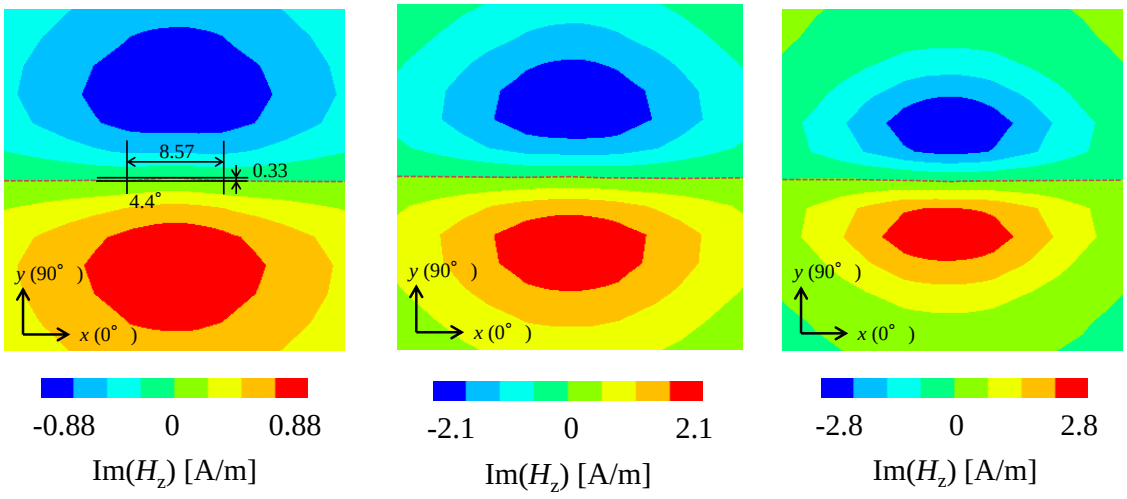

Fig. 4.6 Im(H_z) distributions at the CFRP surface when in-plane waviness is located in the 11th and 12th layers of the cross-ply laminate with the stacking sequence of $[0_2/90_2/0_2/90_2]_s$ (30 mm × 30 mm area under the driver coil): (a) 0.25 MHz, (b) 1 MHz, (c) 4 MHz (unit: millimeters).

subsurface waviness, the use of a lower frequency is desirable. However, Fig. 4.5 shows that the value of Im(H_z) decreases as the drive frequency decreases, which leads to a lower signal-to-noise ratio in actual measurements. It follows that there is a trade-off relationship between the accuracy of the subsurface waviness size estimation and sensitivity. Fig. 4.6 shows the Im(H_z) distribution when in-plane waviness is located in the 11th and 12th layers. The wavy shape of the Im(H_z) = 0 line is slightly visible at 0.25 MHz; it has amplitude of only 0.33 mm. At drive frequencies of 1 and 4 MHz, Im(H_z) = 0 lines are almost straight and the estimation of the waviness size is no longer possible. Therefore, the proposed method can accurately estimate the size of surface waviness, while estimation of the size of deep lying waviness is difficult.

Second, the distribution of Im(H_z) is calculated for a laminate with a stacking sequence of $[0_2/45_2/-45_2/90_2]_s$. In the case of a cross-ply laminate, eddy currents are concentrated only in the fiber direction that corresponds to the driver coil direction. For example, when the driver coil is directed in the 0° fiber direction of a cross-ply laminate, almost no eddy currents are induced in 90° layers under the driver coil and eddy currents are concentrated only in 0° layers. This can be explained by analytical solutions for eddy currents induced by a line current derived in Chapter 2. However, because analytical solutions to the eddy current problem cannot be obtained for CFRP including ±45° layers, the applicability of the proposed method is unknown. We investigate whether the proposed method is effective also for estimating the size of waviness in CFRP including ±45° layers. It is assumed that in-plane waviness is located in the first and second 0° layers, and the driver coil is directed in the 0° direction. Other conditions of the calculations are the same as those used for cross-ply laminate. Fig. 4.7 shows the Im(H_z) distribution in a 30 mm × 30 mm area at the surface of the $[0_2/45_2/-45_2/90_2]_s$

laminate. The shapes and sizes of the Im(H_z) = 0 line in Fig. 4.7 closely match the waviness simulated in the calculations. Hence, waviness can be successfully visualized even in the case of a laminate with ±45° layers. One notable difference between Fig. 4.4 and Fig. 4.7 is that the Im(H_z) = 0 line in Fig. 4.7 is slightly inclined. This is because of the magnetic field generated by eddy current in +45° layers below the top 0° layers. A non-negligible amount of eddy current flows in ±45° layers, resulting in the Im(H_z) = 0 line being inclined relative to the *x* axis. Because the +45° layer is closer to the surface of the CFRP than −45° layer, larger eddy currents flow in the +45° layer because of the skin effect. Thus, the effect of the magnetic field from the +45° layer on Im(H_z) is stronger than that from −45° layer. This explains why the Im(H_z) = 0 line in Fig. 4.7 is inclined relative to the *x* axis in the direction of the +45° fiber. Subsequently, the effect of the in-plane azimuth of the driver coil is investigated. Fig. 4.8 shows numerical

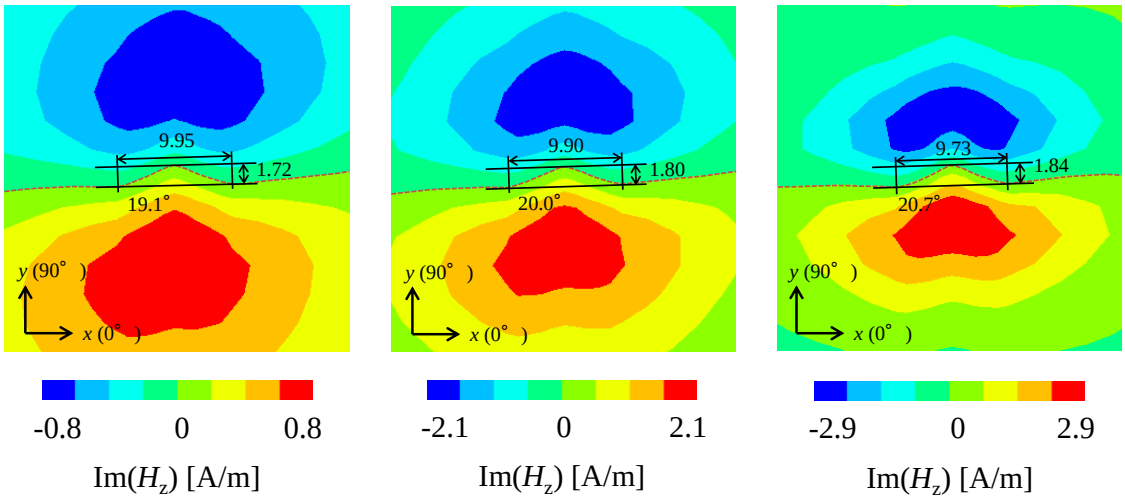

(a) (b) (c)

Fig. 4.7 Im(H_z) distributions at the CFRP surface when in-plane waviness is located in the first and second layers of the laminate including ±45° layers and having the stacking sequence of $[0_2/45_2/-45_2/90_2]_s$ (30 mm × 30 mm area under the driver coil), where the in-plane azimuth of driver coil is 0° direction: (a) 0.25 MHz, (b) 1 MHz, (c) 4 MHz (unit: millimeters).

results of the Im(H_z) distribution in a 30 mm × 30 mm area at the surface of the $[0_2/45_2/-45_2/90_2]_s$ laminate when the azimuth angle of the driver coil varies among 45°, −45° and 90°. The drive frequency used to obtain Fig. 4.8 is 1 MHz. According to Figs. 4.8(a)–(c), in-plane waviness in the first and second 0° layers does not produce clear deformation of the Im(H_z) = 0 line compared with the results in Fig. 4.7 (b). It is almost impossible to grasp the shape and size of in-plane waviness in the first and second 0° layers. It is thus necessary to match the driver coil azimuth with the wavy fiber direction to estimate the waviness shape and size more accurately.

Third, the effect of lift-off of the magnetic field measurement is investigated. The analytical model and excitation conditions are the same as those used to calculate the Im(H_z) distribution in Fig.4.4 (b). It is assumed that the driver coil is placed above the cross-ply CFRP laminate $[0_2/90_2/0_2/90_2]_s$ with a 4 mm lift-off of. In-plane waviness was simulated in the first and second 0° layers like the analytical condition of Fig.4.4(b).

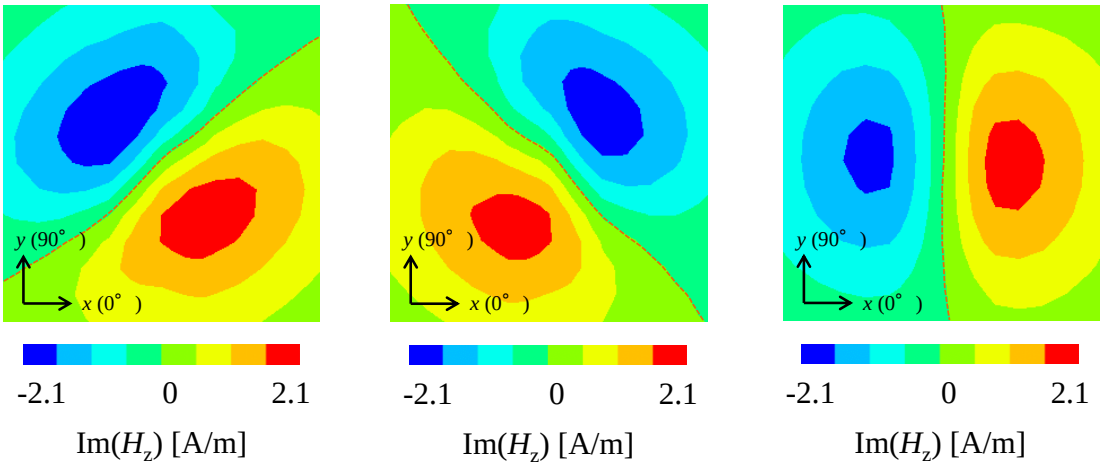

Fig. 4.8 Im(H_z) distributions at the CFRP surface when in-plane waviness is located in the first and second layers of the laminate including ±45° layers $[0_2/45_2/-45_2/90_2]_s$ (30 mm × 30 mm area under the driver coil). The drive frequency is 1 MHz. The in-plane azimuth of the driver coil is in (a) the 45° direction, (b) the −45° direction and (c) the 90° direction.

The driver coil is directed in the 0° fiber direction, and the drive frequency is 1 MHz. Although Fig. 4.4(b) shows the Im(H_z) distribution at the CFRP surface, the Im(H_z) distribution in the area above the CFRP is investigated. Fig. 4.9 shows the Im(H_z) distribution in the area above the CFRP surface. Fig. 4.9(a) is the Im(H_z) distribution in a 30 mm × 30 mm area that is 1 mm above the CFRP surface. The deformation of the Im(H_z) = 0 line has an amplitude of 1.10 mm, which is much smaller than that in Fig. 4.4(b). Fig. 4.9(b) is the Im(H_z) distribution in an area that is 2 mm above the CFRP surface. The amplitude of the Im(H_z) = 0 line in Fig. 4.9(b) is 0.85 mm. It is found that the amplitude of the Im(H_z) = 0 line decreases as the distance between the CFRP surface and the plane in which the magnetic field distribution is measured increases. Thus, the pickup coil used to measure the magnetic field distribution should be in contact with the CFRP surface for accurate estimation of waviness size.

The calculations described above verify that in-plane fiber waviness can be visualized

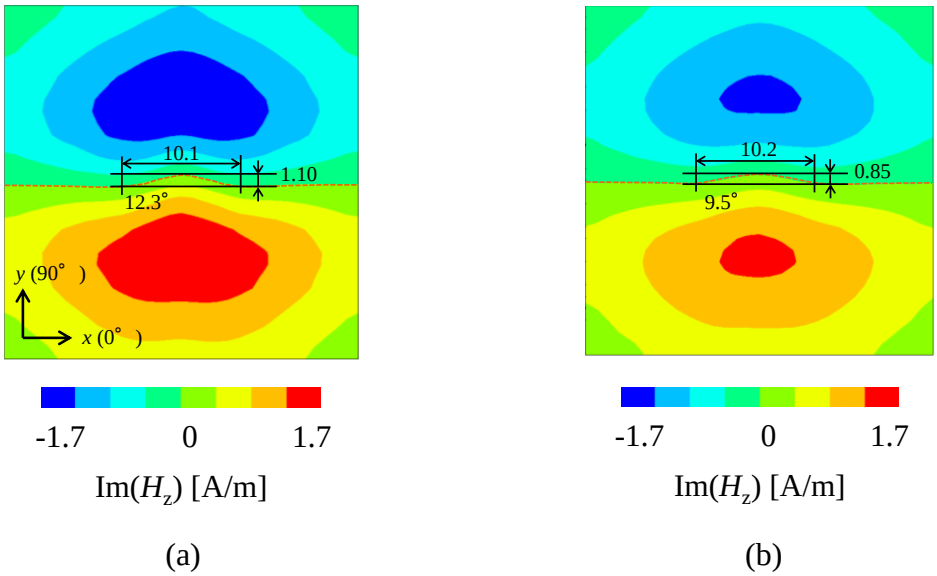

Fig. 4.9 Im(H_z) distributions in an area above the CFRP surface when in-plane waviness is located in the first and second layers of the cross-ply laminate having the stacking sequence of $[0_2/90_2/0_2/90_2]_s$ (30 mm × 30 mm area under the driver coil): (a) area 1 mm above the CFRP surface, (b) area 2 mm above the CFRP surface (unit: millimeters).

using the proposed method. The shape and size of surface waviness can be estimated with high precision using this method. It was found that in-plane waviness in laminates including ±45° layers can also be visualized by matching the driver coil azimuth with the fiber direction with the waviness. FEM results for cross-ply laminate indicate that the amplitude of waviness is underestimated when the waviness is located in a deeper region of the tested material.

4.3 Experimental

4.3.1 Materials

Fig. 4.10 shows CFRP specimens used in experiments of the proposed eddy current imaging.

Fig. 4.10 (a) shows a three-layer cross-ply laminate with a stacking sequence of [0/90/0] (specimen #1). The length and width of the specimen were 250 and 200 mm, respectively. The specimen was fabricated by stacking prepregs (Mitsubishi Rayon Co., Ltd., PYROFIL TR380G250S) and curing them in an electric furnace. In-plane waviness was artificially induced in the first layer over the width along the center line of the specimen. The waviness was formed by deforming carbon fibers in the prepreg prior to molding. Epoxy resin at the center line of the first layer prepreg was removed by wiping it with a paper towel soaked with acetone until carbon fibers could deform. A compressive load was then applied to the resin removed area and in-plane waviness formed along the specimen center line. The prepreg with artificially induced in-plane waviness was stacked and cured following the standard cycle recommended by the manufacturer. As shown in Fig. 4.10(a), the specimen had in-plane waviness with an amplitude of 1.25 mm and a length of 19.9 mm. The angle of the fiber misalignment

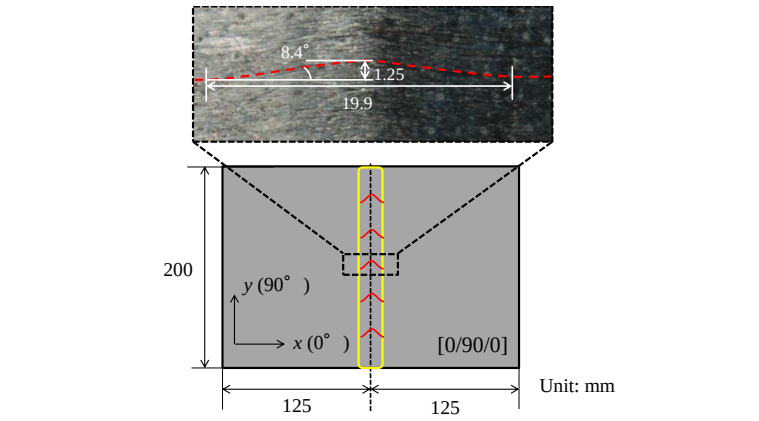

(a)

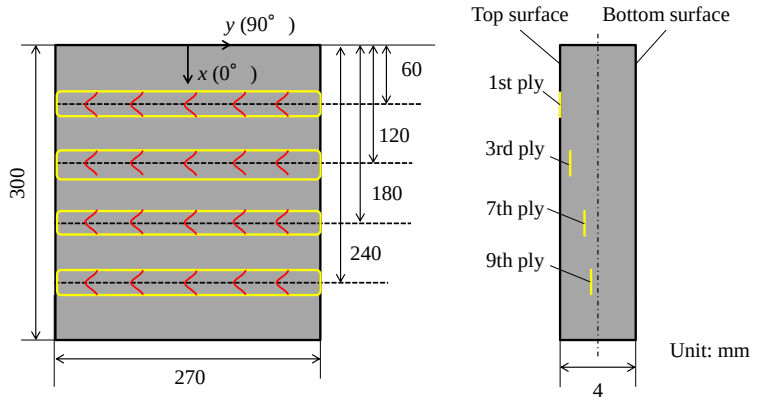

(b)

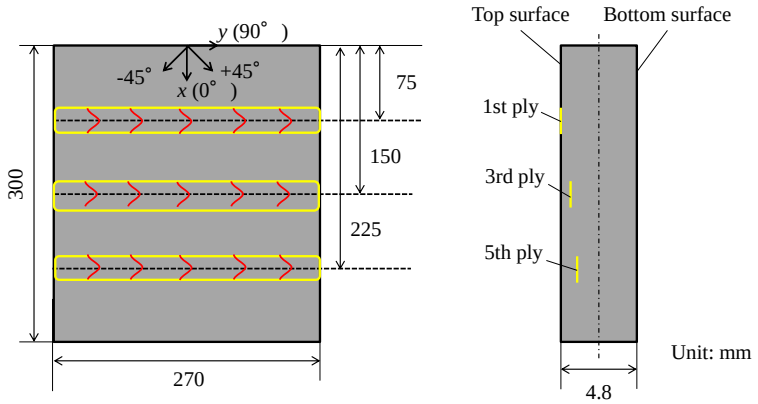

(c)

Fig. 4.10 CFRP specimens with artificially induced in-plane waviness: (a) specimen #1, a three-layer cross-ply CFRP ([0/90/0]) with surface in-plane waviness, (b) specimen #2, a 20-layer cross-ply CFRP ($[(0/90)_5]_s$) with in-plane waviness in the first, third, seventh and ninth layers from the top surface, (c) specimen #3, a 24-layer CFRP including ±45° layers ($[(0/45/0/-45/0/90)_2]_s$) with in-plane waviness induced in the first, third and fifth 0° layers from the top surface.

was 8.4°. Fig. 4.10(b) shows a 20-layer cross-ply specimen with a stacking sequence of $[(0/90)_5]_s$ (specimen #2). The length, width and thickness of the specimen were 300, 270 and 4 mm, respectively. The specimen was fabricated by stacking thermoplastic unidirectional prepregs (Toho Tenax Co., Ltd., Q111E 2000). Multiple in-plane waviness were artificially induced in 0° layers that were the first, third, seventh and ninth layers from the top surface as shown in Fig. 4.10(b). In-plane waviness were induced by deforming fibers in prepreg before molding. A heat gun was used to heat and soften thermoplastic resin in the area where the waviness was induced. Subsequently, carbon fibers were moved in the transverse direction of the prepreg and in-plane waviness could form. The sizes of the in-plane waviness were measured by X-ray CT. The sizes of the waviness estimated from an X-ray CT image are listed in Table 4.2. The size of the first layer waviness was measured from an optical image of the specimen surface.

Fig. 4.10 (c) shows a 24-layer specimen with a stacking sequence of $[(0/45/0/-45/0/90)_2]_s$ (specimen #3). The size of the specimen was 300 mm × 270 mm ×

Table 4.2 Sizes of in-plane waviness in CFRP specimens measured in an X-ray CT test or from an optical image

Specimen	Layer	Amplitude [mm]	Length [mm]	Angle [deg.]
#1	1	1.25	19.9	8.4
#2	1	0.81	14.0	6.9
	3	2.75	16.0	24.9
	7	1.48	10.6	21.8
	9	1.66	10.8	20.6
#3	1	1.23	12.3	13.8
	3	0.99	13.4	10.0
	5	1.56	13.4	16.2

4.8 mm. Specimen #3 was fabricated from the same prepreg as specimen #2. The method used to induce artificial in-plane waviness was the same as that used for specimen #2. In-plane waviness was induced at three depths. Fig. 4.10 (c) shows that in-plane waviness were located in the first, third and fifth 0° layers from the top surface. The sizes of the in-plane waviness measured by X-ray CT are given in Table 4.2.

4.3.2 Experimental setup

Experiments of the estimation of the waviness size were performed for the three specimens in Fig. 4.10. Fig. 4.11 shows the experimental setup of the eddy current imaging method. A vertical rectangular driver coil was fixed above the tested CFRP specimen with a lift-off of 10 mm. The length, width and height of the driver coil were 30, 10 and 2 mm, respectively. The driver coil was longer than waviness length so that the eddy current flows over the waviness zone. The driver coil was turned with enameled copper wire with a diameter of 0.16 mm, and the number of turns was 10. The driver coil was directed in the 0° fiber direction because in-plane waviness were located in 0° layers for all three specimens in Fig. 4.10. A pickup coil was used to measure the distribution of the *z* directional magnetic field at the CFRP surface under the driver coil.

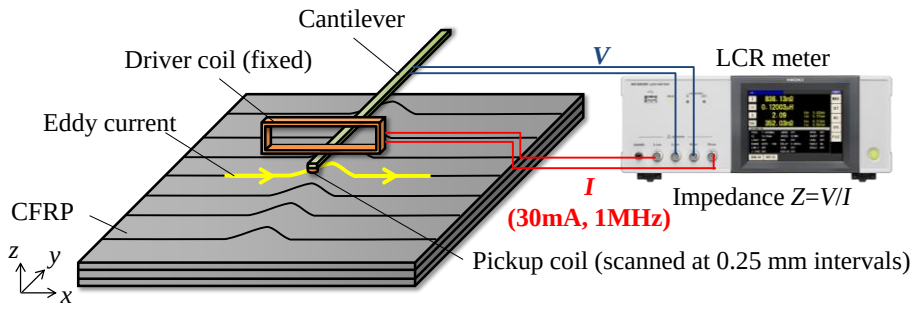

Fig. 4.11 Experimental setup for eddy current imaging. The vertical rectangular driver coil is excited above the waviness zone. The pickup coil scans the CFRP sample under the driver coil to obtain the magnetic field distribution at the surface of the CFRP.

The pickup coil was a 60-turn circular coil with an inner diameter of 0.5 mm. It was turned by enameled copper wire with a diameter of 40 μm. The pickup coil was attached to the tip of a cantilever made from 0.5 mm thick glass fiber reinforced plastic (GFRP). Because the GFRP cantilever is flexible, the pickup coil could scan such that it was in contact with the CFRP surface. A 30 mA, 1 MHz sinusoidal current was applied to the driver coil by an LCR meter (HIOKI E. E. CORPORATION, IM3536). The output voltage of the pickup coil was measured by the LCR meter, and the pickup coil impedance was calculated as the output voltage divided by the drive current. The pickup coil scanned a 30 mm × 30 mm area under the driver coil at 0.25 mm intervals.

The purpose of this experiment was to obtain the Im(H_z) distribution shown in Figs. 4.4–4.7 and to estimate the shape and size of in-plane waviness from the Im(H_z) = 0 line. However, a circular pickup coil does not measure a magnetic field at a point but measures a magnetic field averaged over the circular area. Now we introduce a spatial frequency analysis technique to convert the measured pickup coil impedance $Z(x, y)$ to the magnetic field at the measurement point $H(x, y)$. The impedance of the pickup coil is written as Eq. (4.8) [4.12]–[4.13].

$$Z(x,y) = -\frac{j\omega N}{I}\int_{-\infty}^{\infty}\int_{-\infty}^{\infty} C(x-x', y-y')B_Z(x', y')dx'dy' \tag{4.8}$$

Here, ω is the angular drive frequency, N is number of turns of the pickup coil, I is the drive current and j is the imaginary unit. B_z is the z directional component of the magnetic flux density and C is a step function that depends on the shape of the pickup coil. For a pickup coil with a radius a, C is expressed as Eq. (4.9).

$$C(x,y) = \begin{cases} 1 & (\sqrt{x^2+y^2} < a) \\ 0 & (\sqrt{x^2+y^2} > a) \end{cases} \tag{4.9}$$

By taking the real part of Eq. (4.8), we obtain Eq. (4.10).

$$\frac{\mathrm{Re}(Z)I}{\omega N} = \int_{-\infty}^{\infty}\int_{-\infty}^{\infty} C(x-x', y-y')\,\mathrm{Im}(B_Z(x', y'))dx'dy' \tag{4.10}$$

The right side of Eq. (4.10) is a convolution of C and Im(B_z). Applying the convolution theorem, the two-dimensional Fourier transform of Eq. (4.10) can be expressed as Eq. (4.11).

$$\frac{I}{\omega N} z_{\mathrm{r}}(k_x, k_y) = c(k_x, k_y) b_{\mathrm{i}}(k_x, k_y) \tag{4.11}$$

Here, z_{r}, c and b_{i} are the two-dimensional Fourier transform of Re(Z), C and Im(B_z), respectively. k_x and k_y are spatial frequencies in x and y directions. Eq. (4.11) shows that c is a spatial frequency filter function applied to the Fourier transform of magnetic flux density b_{i}. c can be analytically derived and expressed as Eq. (4.12).

$$c(k_x, k_y) = \frac{J_1(2\pi a\sqrt{k_x^2 + k_y^2})a}{\sqrt{k_x^2 + k_y^2}} \tag{4.12}$$

J_1 is a first-order Bessel function of the first kind. When the pickup coil radius a is 0.25 mm, c is the spatial frequency domain filter shown in Fig. 4.12. Both sides of Eq. (4.11) are divided by c and the inverse Fourier transform is applied to obtain Im(B_z). A problem may arise because there are spatial frequencies that make the value of c zero. A

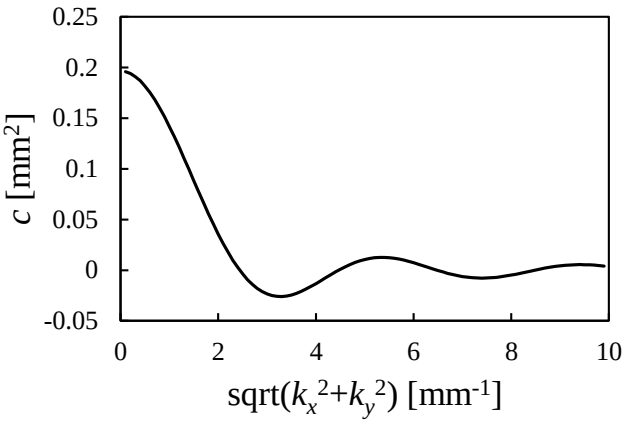

Fig. 4.12 Spatial frequency filter applied to the magnetic field distribution when the radius of the pickup coil a is 0.25 mm.

zero value of c means that some spatial frequencies cannot be reconstructed from measurement data. Because the first zero of $J_1(x)$ is at x = 3.83, this problem can be avoided if the spatial frequencies contributing to the formation of the magnetic field distribution are much lower than the spatial frequency that makes the input value of J_1 in Eq. (4.12) equal to 3.83 [4.12]. The Im(B_z) distribution can be reconstructed using the algorithms described above. Im(H_z) can be calculated by dividing Im(B_z) by magnetic permeability in a vacuum μ_0 (=1.26×10^{-6} H/m).

4.4 Results and discussion

4.4.1 Cross-ply laminate [0/90/0]

Fig. 4.13 shows the result of eddy current imaging for the waviness zone of the three-layer cross-ply specimen with the stacking sequence [0/90/0] (specimen #1). The Im(H_z) distribution calculated using the above mentioned algorithms is displayed in Fig.

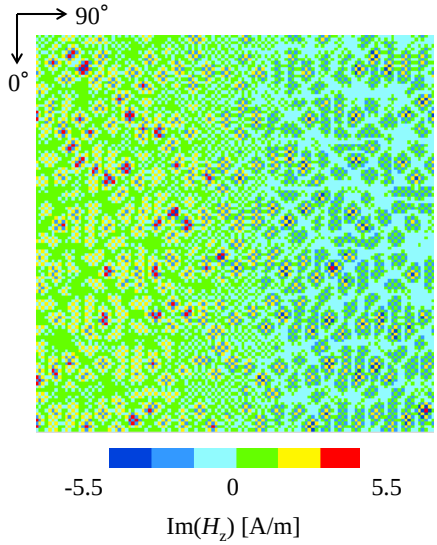

Fig. 4.13 Distribution of the imaginary part of H_z obtained for the three-layer cross-ply specimen (specimen #1). No window function is applied in the spatial frequency domain prior to the inverse Fourier transform. The displayed area is a 30 mm × 30 mm region in the surface waviness zone.

4.13. It is seen that there is large high spatial frequency noise in the obtained image, and that the Im(H_z) = 0 line cannot be recognized. This is because of the noise included in the measured pickup coil impedance, which is not considered in Eq. (4.11). Electromagnetic interference noise in the measured impedance is dominant at high spatial frequencies [4.12]. Because function c in Fig. 4.12 has a smaller value at higher spatial frequencies, dividing the Fourier transform of the measured impedance by c amplifies the high spatial frequency noise in the Im(H_z) distribution. To reduce the high spatial frequency noise in the Im(H_z) image, a Tukey window was applied to the Fourier transform of the measured impedance in the spatial frequency domain. The Tukey window is a window function expressed as Eq. (4.13).

$$w(k_x,k_y)=\begin{cases} 1, \left(\sqrt{k_x{}^2+k_y{}^2}\le k_{\max}\right) \\ \frac{1}{2}-\frac{1}{2}\cos\left(\frac{\pi(\sqrt{k_x{}^2+k_y{}^2}-(k_{\max}+t))}{t}\right), \left(k_{\max}<\sqrt{k_x{}^2+k_y{}^2}<t+k_{\max}\right) \\ 0, \left(\sqrt{k_x{}^2+k_y{}^2}\ge t+k_{\max}\right) \end{cases} \tag{4.13}$$

$k_{\max}$ and t were empirically determined as $k_{\max}$ = 0.75 mm^{-1} and t = 0.25 mm^{-1}. Fig. 4.14 shows the Tukey window function used for the experimental results. Fig. 4.15 shows the Im(H_z) distribution obtained after the implementation of the Tukey window.

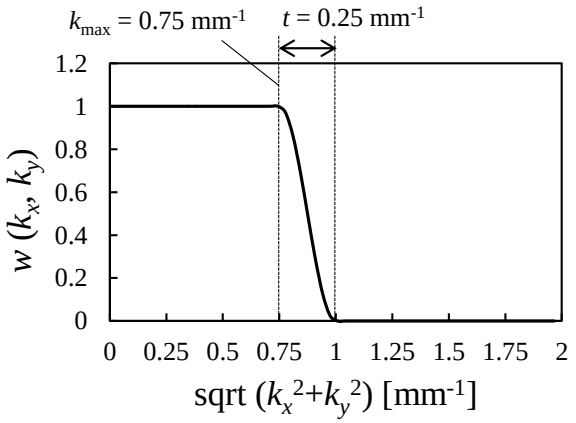

Fig. 4.14 Tukey window used in the spatial frequency domain to reduce high spatial frequency noise in the Im(H_z) image.

The Im(H_z) distribution data in Fig. 4.15(a) was interpolated, and the Im(H_z) = 0 line was highlighted as Fig. 4.15(b) shows. It is seen that high spatial frequency noise is eliminated compared with the case for Fig. 4.13. The Im(H_z) = 0 line in Fig. 4.15 corresponds to the shape of the in-plane waviness in specimen #1. The amplitude and angle of the wavy shape of the Im(H_z) = 0 line are 1.08 mm and 7.5°, which agrees well with the dimensions of fiber waviness in Fig. 4.10(a) (1.25 mm and 8.4°). The reason why waviness amplitude and angle are slightly underestimated in Im(H_z) distribution is that eddy current is induced not only in the first 0° layer, but also in the third 0° layer. A comparison of the length of waviness is omitted because it is difficult to recognize the boundary between the wavy region and non-defective zone. The proposed eddy current imaging method can accurately estimate the size of surface in-plane waviness.

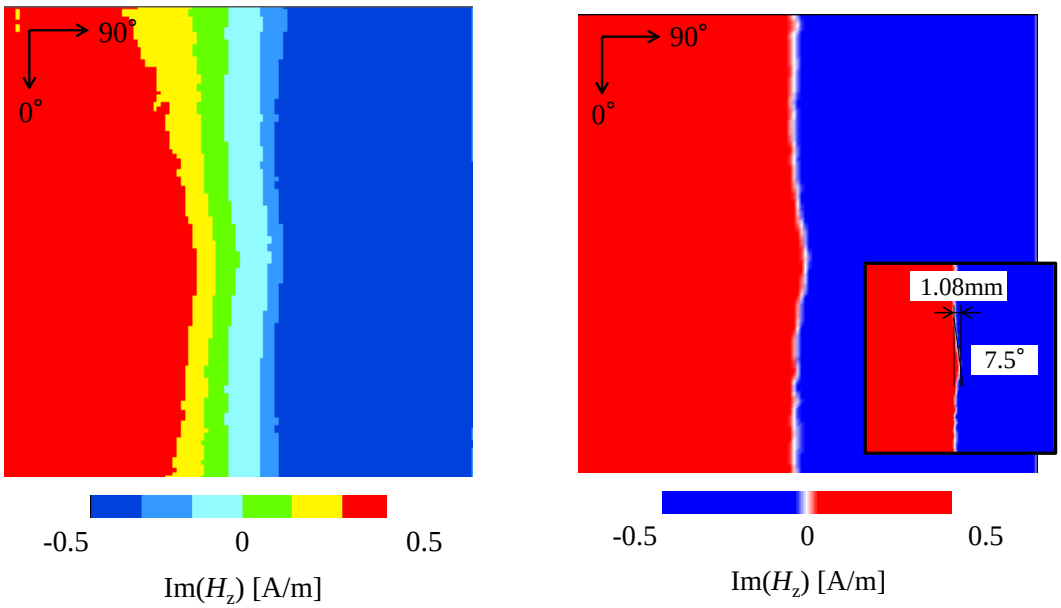

Fig. 4.15 Im(H_z) distribution obtained for a three-layer cross-ply specimen (specimen #1). A Tukey window was used before the inverse Fourier transform. The displayed area is a 30 mm × 30 mm region in the surface waviness zone. (a) Im(H_z) distribution data. (b) The interpolated image with a highlighted Im(H_z) = 0 line. The lower right window shows auxiliary lines used for the estimation of the waviness size.

4.4.2 Cross-ply laminate $[(0/90)_5]_s$

Fig. 4.16 shows the results of eddy current imaging experiments performed for the 20-layer cross-ply laminate with the stacking sequence $[(0/90)_5]_s$ (specimen #2). Figs. 4.16(a)–(e) show the Im(H_z) distributions obtained at the locations of the non-defective zone, first layer waviness, third layer waviness, seventh layer waviness and ninth layer waviness. As shown in Fig. 4.16(a), the Im(H_z) = 0 line obtained in non-defective zone is straight. Because the driver coil was directed in the 0° direction in this experiment, eddy currents are concentrated only in 0° layers immediately under the driver coil. All fibers in 0° layers are straight in 0° direction in the non-defective zone, and eddy current paths are also straight along the carbon fibers. Thus, the *z* directional magnetic field immediately under the driver coil becomes zero, which produces a straight Im(H_z) = 0 line. Fig. 4.16(b) presents the results of the Im(H_z) distribution measurement made at the location of first layer waviness. A wavy shape of the Im(H_z) = 0 line with an amplitude of 0.73 mm and an angle of 5.9° is obtained. These dimensions are close to the actual amplitude and angle of the fiber waviness given in Table 4.2 (0.81 mm and 6.9°). Although the amplitude and angle of the Im(H_z) = 0 line agree well with the actual dimensions of the waviness, the Im(H_z) = 0 line underestimates the waviness amplitude in the same way as for specimen #1. This trend can be seen in the results of FEM analyses shown in Fig. 4.4. The underestimation of the waviness amplitude is caused by the magnetic field generated by eddy currents in non-wavy 0° layers inside the CFRP. Fig. 4.16(c) is the Im(H_z) distribution at the location of third layer waviness. The shape of the waviness can be clearly identified in this image. However, the estimated waviness amplitude is 1.47 mm. This is approximately 53% of the actual amplitude given in Table 4.2 (2.75 mm). As shown in the FEM results of Fig. 4.5,

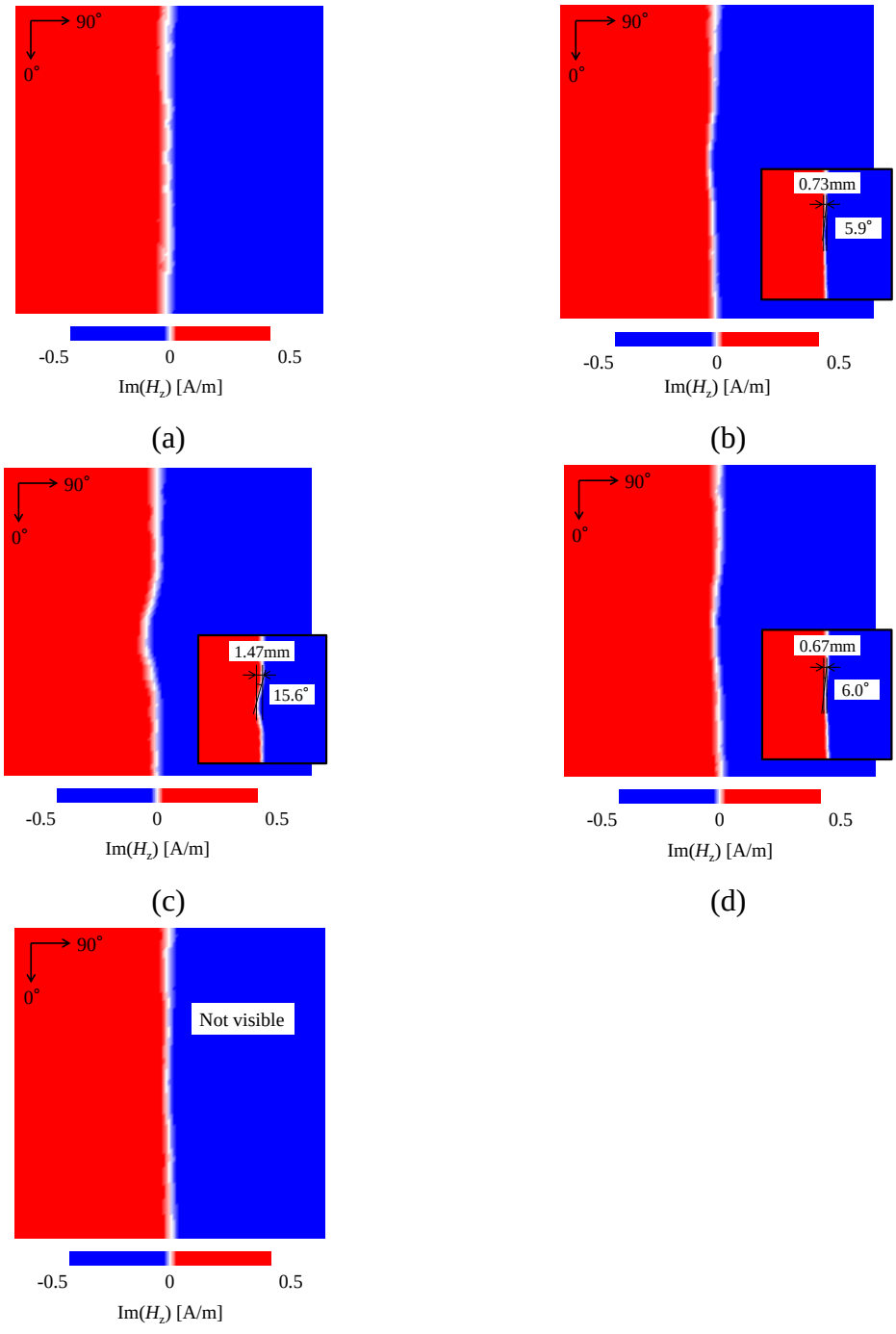

Fig. 4.16 Im(H_z) distributions obtained from the 20-layer cross-ply CFRP specimen (specimen #2): (a) non-defective zone, (b) first layer waviness, (c) third layer waviness, (d) seventh layer waviness and (e) ninth layer waviness. The displayed area is a 30 mm × 30 mm region under the driver coil. Lower-right windows in (b), (c) and (d) show auxiliary lines used for waviness size estimation.

estimation of the amplitude of subsurface waviness has large error and the amplitude is always underestimated. Because of the reduced waviness amplitude in the Im(H_z) image, the estimated angle of the waviness is also smaller than that of the actual waviness. Although accurate estimation of subsurface waviness is difficult, the presence of in-plane waviness can be identified using the proposed method. This is of particular importance in an inspection scenario. For instance, the eddy current probe developed in Chapter 3 can produce a change in the output signal at in-plane waviness zone; however, a signal change can be caused also by a variation of electrical properties originating from material inhomogeneity and lift-off variation. Hence, it is required to know whether the output signal change is caused by waviness in practical application. If the wavy shape of the Im(H_z) = 0 line is observed in the eddy current imaging, it means that the eddy current path is deformed and in-plane waviness exists. This is because eddy current flows along carbon fibers due to large electrical resistivity in transverse and thickness directions of unidirectional ply. In this way, the presence of waviness can be clearly recognized by eddy current imaging. Fig. 4.16(d) presents the result for seventh layer waviness. Because the contribution of 0° layers near the laminate surface to the Im(H_z) distribution is greater, the Im(H_z) = 0 line extremely underestimates the amplitude of the actual waviness. In the case of ninth layer waviness shown in Fig. 4.16(e), the wavy shape of the Im(H_z) = 0 line is no longer recognizable. The results in Fig. 4.16 indicate that the waviness amplitude is always underestimated, and error in estimation of the waviness amplitude increases with the depth of the waviness. Thus, estimation of the waviness size from the Im(H_z) = 0 line gives unsafe side evaluation. Even though it is difficult to accurately estimate the subsurface waviness size, the wavy shape of the Im(H_z) = 0 line is a good indication of the presence of in-plane waviness.

4.4.3 Laminate with ±45° layers $[(0/45/0/-45/0/90)_2]_s$

Fig. 4.17 shows the results of eddy current imaging for the laminate including ±45° layers (specimen #3). Figs. 4.17(a)–(d) show the results obtained at the locations of the non-defective zone, first layer waviness, third layer waviness and fifth layer waviness. Because all waviness were located in the 0° layers, the driver coil was directed in 0° direction. As shown in Fig. 4.17(a), the Im(H_z) = 0 line is straight in the non-defective zone. However, unlike the case for the cross-ply laminate, the line is slightly inclined relative to the 0° direction. This inclination of the Im(H_z) = 0 line is caused by the magnetic field from eddy currents in the +45° direction fibers in the second layer. Even if the driver coil is directed in the 0° direction, eddy currents are not concentrated only in 0° layers in the case of the laminate with ±45° layers. There are eddy currents flowing in ±45° layers, which causes inclination of the Im(H_z) = 0 line as shown in Fig. 4.7. Because the +45° layer is closer than −45° layer to the top layer, the Im(H_z) = 0 line in Fig. 4.17 is inclined relative to the 0° direction in the +45° direction. Fig. 4.17(b) shows the Im(H_z) distribution obtained at the location of first layer waviness. Waviness of the Im(H_z) = 0 line can be observed. If it is assumed that the amplitude of the Im(H_z) = 0 line is a deviation of the Im(H_z) = 0 line from the inclined straight line, the amplitude is estimated to be 1.12 mm. This amplitude is in good agreement with the actual waviness amplitude given in Table 4.2 (1.23 mm). The angle of the Im(H_z) = 0 line is estimated to be 12.4°, and this agrees well with the misalignment angle of the actual waviness (13.8°). The inclination of the Im(H_z) = 0 line can be seen also in the FEM results of Fig. 4.7. Figs. 4.17(c) and (d) show the eddy current imaging results for third and fifth layer waviness, respectively. It is found that the visualization of subsurface waviness in the laminate with ±45° layers is possible. The amplitude of the

waviness estimated from the Im(H_z) = 0 line is smaller than the actual amplitude in the same way as for the cross-ply laminate.

Results obtained from experiments on the three specimens are summarized in Table 4.3. The table compares the waviness sizes estimated by eddy current imaging and those measured from X-ray CT or an optical image. It was found that the proposed eddy

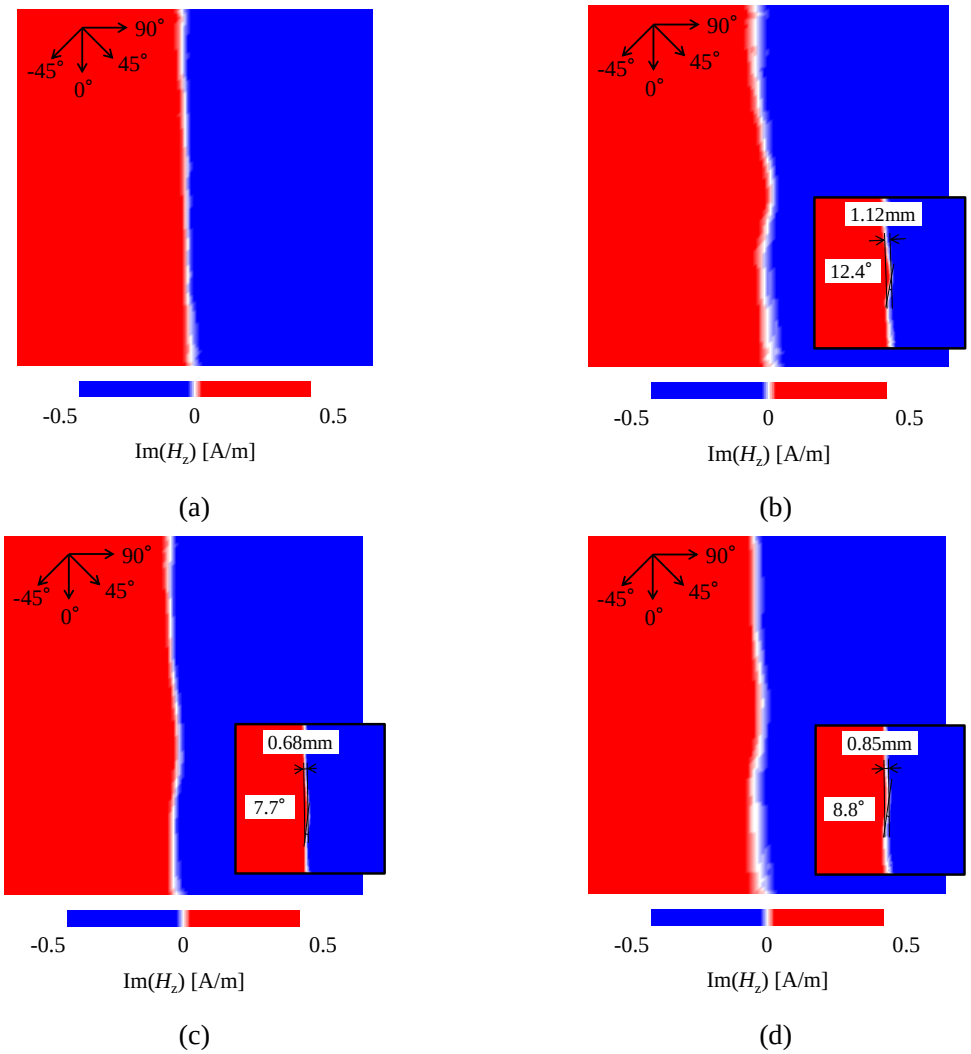

Fig. 4.17 Im(H_z) distributions obtained from a 24-layer CFRP including ±45° layers (specimen #3): (a) non-defective zone, (b) first layer waviness, (c) third layer waviness, (d) fifth layer waviness. The displayed area is a 30 mm × 30 mm region under the driver coil. Lower-right windows in (b), (c) and (d) show auxiliary lines used for waviness size estimation.

current imaging technique has high accuracy in the estimation of the surface waviness size. The size of subsurface waviness is underestimated and the error increases as the waviness is located in a deeper region.

Table 4.3 Comparison of sizes of waviness estimated from eddy current imaging and those measured from X-ray CT or an optical image

Specimen	Layer	Amplitude (eddy current imaging) [mm]	Angle (eddy current imaging) [deg.]	Amplitude (X-ray CT or optical image) [mm]	Angle (X-ray CT or optical image) [deg.]
#1	1	1.08	7.5	1.25	8.4
#2	1	0.73	5.9	0.81	6.9
	3	1.47	15.6	2.75	24.9
	7	0.67	6.0	1.48	21.8
	9	Not visible		1.66	20.6
#3	1	1.12	12.4	1.23	13.8
	3	0.68	7.7	0.99	10.0
	5	0.85	8.8	1.56	16.2

4.5 Conclusions of Chapter 4

A new eddy current imaging method for estimating the shape and size of in-plane fiber waviness in CFRP was proposed. Since eddy current flows along carbon fibers, in-plane waviness can be visualized by visualizing the eddy current path. Conventionally, it is possible to identify the path of electric current by measuring the *z* directional magnetic field perpendicular to the *x*-*y* plane in which the electric current flows. However, the magnetic field in eddy current testing includes magnetic fields from both the drive current and eddy current, which makes it difficult to visualize eddy current from the magnetic field. To eliminate the effect of the magnetic field from the driver coil, we proposed a new method that measures the magnetic field out-of-phase with the drive current. By measuring the quadrature component of the magnetic field, the magnetic field from the eddy current alone can be obtained. The validity of the proposed method was investigated in FEM analyses. It was found that when the in-plane waviness is located at the top surface of the CFRP laminate, the $\mathrm{Im}(H_z) = 0$ line is in good agreement with the shape and size of waviness. The numerically calculated $\mathrm{Im}(H_z) = 0$ line produced by subsurface waviness has a smaller amplitude than simulated waviness, which indicates that the $\mathrm{Im}(H_z) = 0$ line underestimates the amplitude of waviness. This is because of the magnetic field from eddy currents in non-wavy layers close to the top surface. The results of FEM analysis revealed that the use of a higher drive frequency is better in estimating the size of surface waviness, while a lower frequency is better for subsurface waviness.

Experiments on the proposed eddy current imaging were performed for cross-ply laminates and a laminate including ±45° layers. A pickup coil was used as a magnetic sensor to obtain the two-dimensional distribution of the magnetic field. Spatial

frequency analysis was introduced to reconstruct the Im(H_z) distribution from measured pickup coil impedance. It was found that the Im(H_z) = 0 line obtained from surface waviness corresponds well to the shape and size of actual waviness. Surface waviness with an amplitude of around 1 mm was successfully visualized. The amplitude and angle of surface waviness could be estimated with error of approximately −10% and −1°, respectively. However, the amplitude of subsurface waviness estimated from the Im(H_z) = 0 line was smaller than that of actual waviness as predicted in FEM analyses. The estimated amplitude of waviness in third layer of a $[(0/90)_5]_s$ laminate was 53% of the actual amplitude. Error in the angle of the third layer waviness was −9.3°. Experimental results show that the amplitude of in-plane waviness is underestimated when employing the proposed method. Thus, the evaluation of waviness size is always on the unsafe side. In conclusion, the shape and size of surface waviness can be estimated with high accuracy using the proposed eddy current imaging method, while the size of subsurface waviness is underestimated. In any case, the presence of waviness can be identified using the proposed method.

4.6 References

[4.1] J. R. Bowler, “Eddy current calculations using half-space Green’s functions”, Journal of Applied Physics, Vol. 61, No. 3, (1987), pp. 833-839.

[4.2] J. R. Bowler and S. A. Jenkins, “Eddy-current probe impedance due to a volumetric flaw”, Journal of Applied Physics, Vol. 70, No. 3, (1991), pp. 1107-1114.

[4.3] Stephan J. Norton and John R. Bowler, “Theory of eddy current inversion”, Journal of Applied Physics, Vol. 73, No. 2, (1993), pp. 501-512.

[4.4] J. R. Bowler, “Eddy-current interaction with an ideal crack. I. The forward problem”, Journal of Applied Physics, Vol. 75, No. 12, (1994), pp. 8128-8137.

[4.5] Jozsef Pavo and Kenzo Miya, “Reconstruction of Crack Shape by Optimization Using Eddy Current Field Measurement”, IEEE Transaction on Magnetics, Vol. 30, No. 5, (1994), pp. 3407-3410.

[4.6] Haoyu Huang, Nozomu Sakurai, Toshiyuki Takagi, Tetsuya Uchimoto, “Design of an eddy-current array probe for crack sizing in steam generator tubes”, NDT & E International, Vol. 36, (2003), pp. 515-522.

[4.7] F. Baudenbacher, N. T. Peters, P. Baudenbacher, J. P. Wikswo, “High resolution imaging of biomagnetic fields generated by action currents in cardiac tissue using a LTS-SQUID microscope”, Physica C, Vol. 368, (2002), pp. 24-31.

[4.8] F. Infante, P. Perdu, D. Lewis, “Magnetic microscopy for 3D devices: Defect localization with high resolution and long working distance on complex system in package”, Microelectronics Reliability, Vol. 49, (2009), pp. 1169-1174.

[4.9] K. Abiru, Y. Honda, M. Inoue, T. Kiss, Y. Iijima, K. Kakimoto, T. Saitoh, K. Nakao, Y. Shiohara, “Visualization of non-uniform current flow in coated conductors by scanning Hall-probe magnetic microscopy”, Physica C, Vol. 469, (2009), pp. 1450-1453.

[4.10] Y. Shibata, S. Nomura, H. Kashiwaya, S. Kashiwaya, R. Ishiguro and H. Takayanagi, “Imaging of current density distributions with a Nb weak-link scanning nano-SQUID microscope”, Scientific Reports, Vol. 5, No. 15097, (2015).

[4.11] J.C. Abry, S. Bochard, A. Chateauminois, M. Salvia, G. Giraud, “In situ detection of damage in CFRP laminates by electrical resistance measurements”, Composites Science and Technology, Vol. 59, (1999), pp. 925-935.

[4.12] Bradley J. Roth, Nestor G. Sepulveda and John P. Wikswo Jr., “Using a magnetometer to image a two-dimensional current distribution”, Journal of Applied Physics, Vol. 65, No.1, (1989), pp.361-372.

[4.13] Bradley J. Roth and John P. Wikswo Jr., “Apodized pickup coils for improved

spatial resolution of SQUID magnetometers", Review of Scientific Instruments, Vol. 61, No. 9, (1990), pp. 2439-2448.

Chapter 5

Conclusions and future works

This thesis presented an eddy current technique for detection and size estimation of fiber waviness in CFRP. Eddy current distributions in CFRPs were investigated by obtaining analytical solutions and conducting FEM analyses. Findings obtained from the calculations were used to propose a new eddy current method specialized for waviness detection. An eddy current imaging technique was also newly developed to estimate the shape and size of waviness.

In Chapter 2, analytical solutions for eddy current induced by an infinitely long line drive current were derived. Maxwell's equations were solved taking the orthotropic electrical conductivity of unidirectional CFRP into consideration. The differential equations can be solved when the line drive current is directed in the fiber direction or transverse direction of the CFRP. The derived solutions indicate that the eddy current distribution depends only on electrical conductivity in the drive current direction. Moreover, eddy current is directed only in the direction of the line drive current. The solution method can be used to derive the eddy current distribution in cross-ply laminates that are composed of 0° and 90° fiber layers. When the line drive current is directed in the 0° or 90° direction, eddy currents are concentrated only in the fiber direction corresponding to the line drive current direction. Subsequently, the penetration depth of eddy current calculated from the analytical solution was compared with that calculated from the conventionally used general expression of skin depth. The general expression is an approximation that postulates that the penetration depth depends only on the drive frequency and electromagnetic properties of the tested material. However, the analytical solutions clearly show that the penetration depth depends also on the width and lift-off of the drive current. It was found that the general expression

overestimates the penetration depth, and the error becomes larger as the width and lift-off of the line drive current decrease.

In Chapter 3, an eddy current probe specially designed for the detection of in-plane waviness was proposed. The probe is composed of a vertical rectangular driver coil and a rectangular pickup coil that are perpendicular to each other. The advantages of the proposed probe are its high sensitivity to in-plane waviness and the selectability of the inspected fiber direction. When the driver coil is directed in one of the fiber directions of the cross-ply laminate, eddy currents can be concentrated in the fiber direction with the driver coil direction. Hence, the inspected fiber direction can be chosen by changing the in-plane probe azimuth. Identification of the wavy fiber direction is of particular importance because waviness causes degradation of mechanical property in the fiber direction with the waviness. The selectability can be explained by the analytical solutions for the eddy current derived in Chapter 2. Additionally, three-dimensional FEM analyses verified that eddy currents can be concentrated in one fiber direction under the driver coil. The validity of the probe was experimentally investigated using cross-ply CFRP specimens with artificially induced in-plane waviness. Experimental results showed that the proposed probe produces distinct changes in pickup coil output at the locations of waviness. The minimum misalignment angle of the detected waviness was 6.9°. A recognizable output signal change was obtained for waviness up to 18 layers from the inspected surface. These results were obtained for a drive frequency up to 1 MHz, which is much lower than the frequency used in the conventional eddy current testing of CFRP. Hence, the proposed probe can detect in-plane waviness in deeper regions. The sensitivity of the proposed probe was compared with that of a

conventionally used half-transmission probe. The comparative study also showed that the proposed probe is more sensitive at the same drive frequency. Experiments in which the probe was directed in the direction perpendicular to the wavy fiber direction did not show a signal change at waviness zones. This result indicates that the fiber orientation with waviness can be identified by changing the probe azimuth. The effectiveness of the probe for a CFRP laminate including ±45° layers was also investigated. FEM analyses showed that it is difficult to distribute eddy currents in one fiber direction in the case of the laminate with ±45° layers. However, the numerical results imply that the proposed probe is most sensitive to waviness when the probe is directed in the fiber direction with the waviness. Experimental studies showed that the proposed probe produces a clear change in the output signal at waviness zones when the probe is directed in the wavy fiber direction. Meanwhile, a distinct signal change cannot be detected when the probe azimuth matches other fiber directions. Therefore, the fiber direction with waviness can be identified even if the tested CFRP includes ±45° layers.

In Chapter 4, an eddy current method to visualize in-plane waviness was developed. Because eddy currents flow along carbon fibers, fiber waviness can be visualized if the eddy current path is visualized. The eddy current path is visualized using information of the magnetic field distribution. In the visualization of the eddy current path, the excitation field generated by the driver coil prevents the measurement of the magnetic field generated by the eddy current. To solve this problem, a complex plane analysis method was newly proposed to eliminate the effect of the excitation field. Spatial frequency analysis was introduced to convert the pickup coil impedance distribution to the magnetic field distribution. To investigate the validity of the proposed method, FEM

analyses and experiments were performed for cross-ply laminates and a laminate including ±45° layers. FEM analyses and experiments showed that the proposed method accurately estimates the size of surface waviness in multidirectional laminates. Errors in the estimation of the amplitude and misalignment angle of the surface waviness were approximately −10% and −1°, respectively. Sizes of subsurface waviness were always underestimated, and the estimation error becomes larger as the depth of subsurface waviness increases. Although the size estimation of waviness in a deeper region becomes more difficult, the wavy shape of the visualized eddy current path is an indication of presence of waviness. Even if change in the output signal is obtained from the probe proposed in Chapter 3, it does not necessarily indicate that waviness is present. This is because a signal change can be a result of a variation of conductivity in the CFRP or a variation of lift-off during scanning. Hence, the visualization technique proposed in Chapter 4 is needed to confirm whether the signal change is caused by waviness.

An inspection scenario that adopts the eddy current method described in this thesis is shown in Fig. 5.1. Fig. 5.1 is an example of an inspection scenario in the case of testing a cross-ply CFRP laminate. First, the probe proposed in Chapter 3 scans the CFRP in two ways: 0° scanning and 90° scanning. The probe is directed in the 0° fiber direction during 0° scanning, and the probe is directed in 90° fiber direction during 90° scanning. When in-plane waviness is located in the 0° fiber direction, there is a variation in probe output during 0° scanning. From the results obtained in 0° and 90° scanning, waviness can be detected and the fiber orientation with that waviness can be identified. The drive frequency required to achieve the appropriate skin depth can be roughly determined

from analytical solutions for the eddy current derived in Chapter 2. Second, eddy current imaging in Chapter 4 is performed at the location where the change in probe output is obtained. The vertical rectangular driver coil is directed in the fiber direction with the probe output variation, and is fixed above the CFRP under test. The pickup coil scans the CFRP surface to obtain the magnetic field distribution. The size of deformation of the line on which the *z* directional magnetic field from the eddy current becomes zero is measured to estimate the waviness size. In this procedure, the presence of waviness can be confirmed and the size of waviness can be estimated.

Although eddy current techniques described in this thesis can detect and visualize in-plane waviness, problems remain for industrial application.

Even if there is a recognizable signal change of the eddy current probe during scanning, we cannot conclude that the location is a waviness zone. A slight signal change can be easily caused by a variation of the electrical property in the CFRP even at the non-defective zone. Hence, it is necessary to define a clear border between an acceptable signal change and unacceptable signal change. Generally, a threshold of the output signal change is set to define the border. The threshold can be determined by the output signal change caused by an unacceptable size of defect. Investigation of the signal change produced by a predefined size of waviness in a reference specimen can allow users to determine the threshold. If the threshold is determined from a signal change caused by waviness in the bottom layer of the reference specimen, safe side evaluation may become possible.

In the waviness visualization technique described in this paper, the size of subsurface waviness is underestimated, which always offers unsafe side evaluation. To solve this

problem, future works should focus on an eddy current testing method that is able to identify the defect depth. If the depth of in-plane waviness can be identified, the visualized waviness size can be corrected using the FEM results and the waviness size can be more accurately estimated. Despite the drive frequency dependence of the penetration depth, it remains difficult to accurately identify the defect depth. No study has reported a method to accurately identify the defect depth in CFRP. Therefore, a technique to identify the defect depth is required to accurately estimate the size of subsurface waviness size.

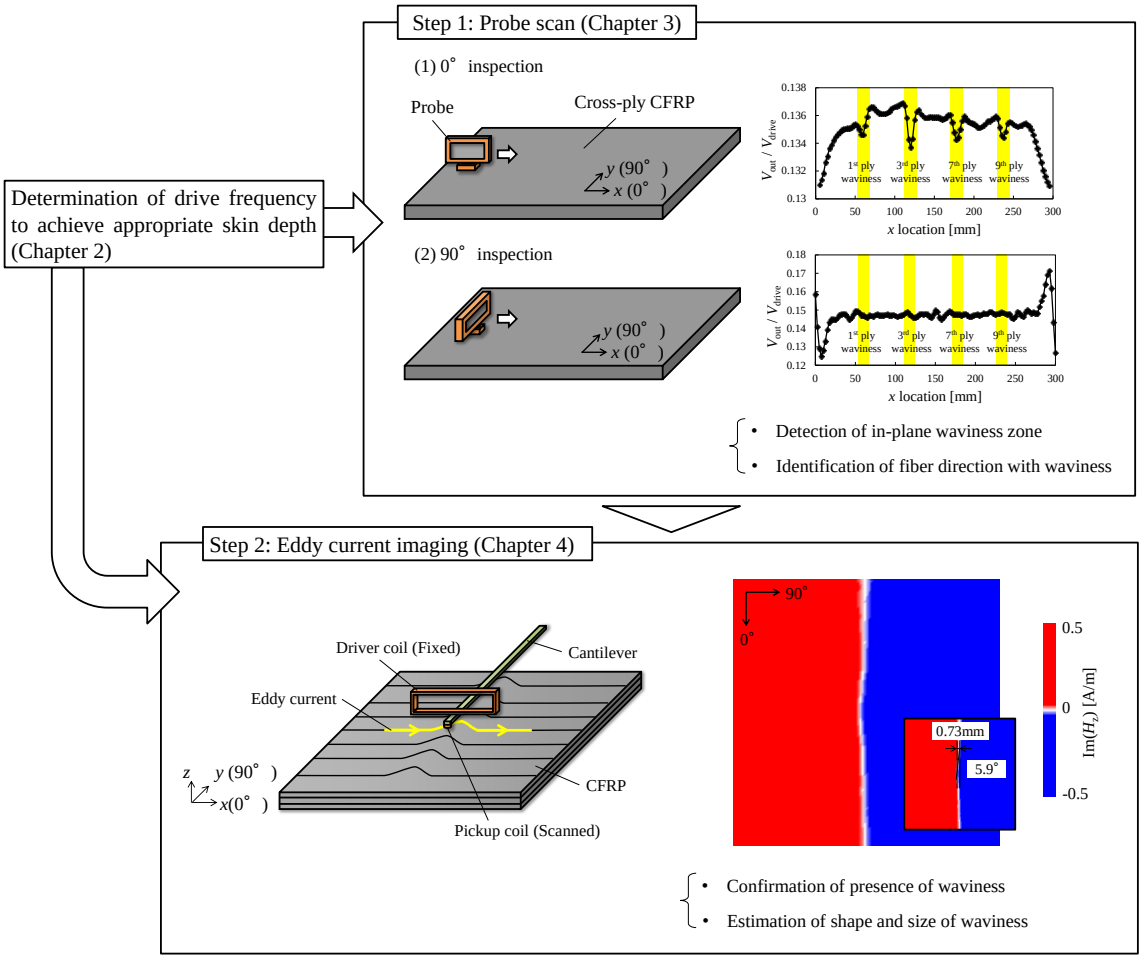

Fig. 5.1 Scenario of eddy current testing for in-plane fiber waviness in CFRP described in this thesis.

List of publications

(1) Koichi MIZUKAMI, Yoshihiro MIZUTANI, Kenshi KIMURA, Akiyoshi SATO, Akira TODOROKI, Yoshiro SUZUKI and Yoshiaki NAKAMURA “Visualization and size estimation of fiber waviness in multidirectional CFRP laminates using eddy current imaging”, Composites: Part A, Vol. 90, (2016), pp. 261-270. (Chapter 4)

(2) Koichi MIZUKAMI, Yoshihiro MIZUTANI, Akira TODOROKI and Yoshiro SUZUKI, “Analytical solutions to eddy current in carbon fiber-reinforced composites induced by line current”, Advanced Composite Materials, Vol. 25, Issue 4, (2016), pp. 385-401. (Chapter 2)

(2’) 水上孝一, 水谷義弘, 轟章, 鈴木良郎, 「線状電流により炭素繊維強化複合材料に誘導される渦電流の解析解」, 日本複合材料学会誌, Vol. 42, No. 3, (2016). ((2)の邦文誌投稿) (Chapter 2)

(3) Koichi MIZUKAMI, Yoshihiro MIZUTANI, Kenshi KIMURA, Akiyoshi SATO, Akira TODOROKI and Yoshiro SUZUKI, “Detection of in-plane fiber waviness in cross-ply CFRP laminates using layer selectable eddy current method”, Composites: Part A, Vol. 82, (2016), pp. 108-118. (Chapter 3)

(4) Koichi MIZUKAMI, Yoshihiro MIZUTANI, Akira TODOROKI and Yoshiro SUZUKI, “Detection of in-plane and out-of-plane fiber waviness in unidirectional carbon fiber reinforced composites using eddy current testing”, Composites: Part B, Vol. 86, (2016), pp. 84-94. (Chapter 1)

(5) 水上孝一, 中村圭亨, 水谷義弘, 轟章, 鈴木良郎, 「透過モードによる誘導加熱アシスト近共振型渦電流試験を用いた CFRP のはく離検出」, 実験力学, Vol. 15, No. 3, (2015), pp. 200-204.

(6) Koichi MIZUKAMI, Yoshihiro MIZUTANI, Akira TODOROKI and Yoshiro SUZUKI, “Detection of delamination in thermoplastic CFRP welded zones using induction heating assisted eddy current testing”, NDT & E International, Vol. 74, (2015), pp. 106-111.

(7) Koichi MIZUKAMI, Yoshihiro MIZUTANI, Akira TODOROKI and Yoshiro SUZUKI, “Design of eddy current-based dielectric constant meter for defect detection in glass fiber reinforced plastics”, NDT & E International, Vol. 74, (2015), pp. 24-32.

(8) 水上孝一, 水谷義弘, 轟章, 鈴木良郎, 「渦電流試験による温度検知を用いた熱可塑性CFRP溶着不良の検出」, 日本機械学会論文集, Vol. 80, No. 812, (2014), p. SMM0084.

International conferences

(1) Koichi MIZUKAMI, Yoshihiro MIZUTANI, Akira TODOROKI, Yoshiro SUZUKI, Akiyoshi SATO and Kenshi KIMURA, "Development of a probe of eddy current testing for detection of in-plane waviness in CFRP cross-ply laminates", Proceedings of the 7th International Conference on NDT in Aerospace, (2015). (Chapter 3)
(2) Koichi MIZUKAMI, Yoshihiro MIZUTANI, Akira TODOROKI and Yoshiro SUZUKI, "Detection of delamination in thermoplastic CFRP weld parts using eddy current testing and induction heating", Proceedings of the 11th European Conference on Non-Destructive Testing, (2014).
(3) Koichi MIZUKAMI, Yoshihiro MIZUTANI, Akira TODOROKI, and Yoshiro SUZUKI, "In-situ inspection of thermoplastic CFRP welded zones using eddy current thermo-sensing", Proceedings of the 2nd International Symposium on Laser Processing for CFRP and Composite Materials, (2013).

Awards

(1) 平成 24 年 12 月　National Instruments Graphical System Design Contest 2012 学生部門最優秀賞
(2) 平成 25 年　3 月　日本機械学会　畠山賞
(3) 平成 25 年　8 月　日本実験力学会年次大会　優秀講演賞
(4) 平成 25 年 11 月　日本非破壊検査協会秋季講演大会　新進賞
(5) 平成 26 年　9 月　日本複合材料学会第39回複合材料シンポジウム　林学生賞
(6) 平成 26 年 10 月　National Instruments Graphical System Design Contest 2014 学生部門最優秀賞
(7) 平成 27 年　1 月　東京工業大学機械物理工学専攻中間発表　グッドプレゼン賞1位
(8) 平成 27 年　3 月　日本複合材料学会第6回複合材料会議(JCCM-6)優秀講演賞
(9) 平成 28 年　5 月　日本機械学会関東支部第22期総会　若手優秀講演賞